Spectroscopy and evaporative cooling of rubidium atoms in radiofrequency dressed traps

Raghavan Kollengode Easwaran

UNIVERSITE PARIS XIII
INSTITUT GALILEE

LABORATOIRE DE PHYSIQUE DES LASERS

Thèse présentée par

Raghavan Kollengode Easwaran

pour obtenir le grade de

Docteur en science de l'Université Paris13

Sujet de la thèse :

Spectroscopy and evaporative cooling of rubidium atoms in radiofrequency dressed traps

Soutenue le 16 avril 2009 devant le jury composé de :

Mme	Isabelle Bouchoule	Rapporteur
M.	Pierre Lemonde	Rapporteur
M.	C. S. Unnikrishnan	Examinateur
M.	Thomas Coudreau	Examinateur
M.	Vincent Lorent	Directeur de Thèse
Mme	Hélène Perrin	Co-Directeur de Thèse

Contents

Acknowledgments

It brings me great pleasure to thank many people who have made this thesis possible. This thesis would not have been possible without the kind support and encouragement of my Ph.D supervisors Vincent Lorent and Hélène Perrin. I am grateful to both for their caring supervision, their enthusiastic involvement in this project and their supportive suggestions and comments. I am also grateful towards other members of our group L.Longchambon, Paul-Eric Pottie and T.liennard for helping me in the experiment and to our collaborator Barry Garraway for fruitful discussions. It was a great learning and enriching experience for me at L.P.L during last three years of my Ph.D.

I will thank the members of elctronics work shop and mechanical work shop for their efficient support in building required components for our experiment. I thank the whole administrative staffs for helping and guiding me to fulfill my administrative requirements being a foriegn candidate.

I dedicate this work to my family, especially my mother Kaveri for giving me all the support I needed along with my brother Subramanian and sister Jayasree. I thank my two best friends Sapna Benali and Anshita Ganjoo who gave me moral support all the way and made my stay extremely comfortable at Maison de l'Inde. I thank all my friends in fourth floor Maison de l'Inde especially to Pranav, Raji and Jensen.

Chapter 1

Introduction

Bose-Einstein condensation (BEC) is a quantum statistics phenomenon which occurs in a 3D system of bosons (particles with an integer spin) when the characteristic thermal de Broglie wavelength of particles exceeds the mean interparticle separation. Under this condition it is favorable for particles to occupy a single ground state, and below a critical temperature the population of this state becomes macroscopic. This phenomenon has been predicted as a result of the work of Bose [1] and Einstein [2,3] in the mid twenties. Since that time, a number of phenomena have been considered as manifestations of BEC: superfluidity in liquid helium [4], condensation of hypothetical Higgs particles, BEC of pions [5] and so on. Bose-Einstein condensation in dilute gases has been observed in 1995 in pioneering experiments with clouds of magnetically trapped alkali atoms at JILA [6], MIT [7] and RICE [8].

Since then the field of ultracold quantum gases has developed from the point of proof of principle to a mature field, and hundreds of BEC experiments with different atoms, atom numbers, temperatures, interatomic interactions and trapping geometries have been performed. In recent years, the investigation of quantum gases in low dimensional trapping geometries has significantly attracted the attention of the physics research community [9]. This growing interest is motivated, partially, by the current possibilities that the extremely rapid progress in integrated atom optics [10, 11] has opened for the manipulation of Bose-Einstein condensed atoms. This development allows the study of crucial problems associated with the strong modifications that the fundamental properties of these quantum systems experience due to the reduced dimensionality. For instance, a one dimensional (1D) Bose gas in the Tonks-Girardeau regime mimics a system of noninteracting spinless fermions [12–14]. In 2D, the superfluidity emerges due to the vortex binding-unbinding Berezinskii-Kosterlitz-Thouless phase transition [15–17] recently observed [18].

For the study of the BEC low-dimensional physics, trapping configurations of different nature and topology have been proposed and used. For example, the 3D to 1D crossover was explored by Görlitz *et al.* [19] in an elongated Ioffe-Pritchard type dc magnetic trap, the phase defects of a BEC were investigated in a quasi-2D trap based on a 1D optical lattice [20] and, in atom chip experiments, dc current-carrying wires

are usually employed to confine atoms in highly anisotropic traps [11].

Since a few years, adiabatic potentials, resulting from a combination of dc and radio-frequency (rf) magnetic fields, have become a very attractive and promising tool. This anisotropic quasi two dimensional trap was proposed by O. Zobay and B. M. Garraway [21] in 2001 and was experimentally realized in our lab by Y. Colombe *et al.* [22] in 2003. A possibility of performing evaporative cooling [23] in such traps and loading them into a ring geometry [24] was also theoretically studied in our group.

The motivation of my Ph.D thesis was to reach quantum degeneracy in lower dimensions and to implement a ring trap [24] for the study of persistent currents [25] and superfluid propagation phenomenons [26]. As a first step for that I could experimentally demonstrate an evaporative cooling mechanism in rf dressed trap during my Ph.D. The future goal of this experiment will be to reach degeneracy in this trap and to implement a ring trap.

This manuscript will be organized as follows: In Chapter 2, I give a general overview on the Bose-Einstein condensate experimental set up and then I will describe in more detail the parts where I was personally involved during my thesis. For a more detailed description of this experimental set up, I refer the reader to the previous dissertations of Y. Colombe and O. Morizot [27, 28].

In Chapter 3, I briefly explain the technique of loading the atoms into a rf dressed trap starting from a static magnetic trap. This topic was also already discussed in the previous dissertations of Y. Colombe and O. Morizot [27, 28].

In his dissertation, O. Morizot discusses the issue of technical noise coming from the rf components which was preventing him to go further in the direction of evaporative cooling and reaching quantum degeneracy. In my thesis, we studied this topic intensively, with different rf sources, which allowed us to fulfill the requirements on the rf source quality. In Chapter 4, I discuss these requirements on the rf source used to trap neutral atoms in rf-dressed potentials. We could very well reduce the technical noise, by choosing proper rf components and fulfilling the rf requirements. The long lifetimes and low heating rates reported in this chapter made ideal conditions to do an evaporative cooling directly in the rf-based trap.

Chapter 5 is devoted to evaporative cooling performed in the rf-dressed trap. To understand well the evaporation mechanism, we first made some spectroscopic measurements in this trap. This is a natural way of determination of the dressing Rabi frequency, and also gives a measurement of the temperature in the trap. We found that one of the transition involving a two photon process was efficient to outcouple the hotter atoms as compared to other transitions. We used this particular transition for evaporation and could reduce the temperature and increase the phase space density, which is the signature of evaporative cooling. The highest phase space density was obtained as a compromise between a high initial number of atoms and an initial temperature as low as possible. As a matter of fact, the transfer of the atoms between the magnetic trap and the dressed trap is not adiabatic due to the low oscillation frequency in the x direction. Despite the evidence for evaporative cooling, the degeneracy could not be reached in this trap.

To increase the horizontal oscillation frequency, we decided to dress the quadrupo-

lar trap since horizontal oscillation frequencies are higher in this case. A method to dress this trap is explained in 6. The role of the rf polarization is highlighted as it becomes important in this configuration. Here we experimentally demonstrate the loading scheme and show a way to improve the initial conditions. In future, the next step will be to perform an evaporative cooling in the dressed Quadrupole down to quantum degeneracy. This system will be very interesting to make a ring trap and to see persistent currents by rotating the ring trap [24].

Chapter 2

Experimental set up

In this chapter, I briefly describe the apparatus which is used to produce a ^{87}Rb Bose-Einstein condensate for our studies of ultracold atoms confined in rf-induced two dimensional trapping potentials. This chapter is organized as follows: first I will give a general overview on the Bose-Einstein condensate experimental set up and then I will describe in more detail the parts where I was personally involved during my thesis, namely, the procedure to arrange precisely the three coils of the trap and the spatial filtering of the probe laser beam. For a more detailed description of the experimental set up, I refer the reader to the previous dissertations of Y. Colombe and O. Morizot [27,28].

2.1 General Overview

Bose-Einstein condensation occurs when a macroscopic population of bosons occupy the same quantum state at non-zero temperature. To reach quantum degeneracy we need to cool the atoms to a very low temperature of order 100 nK. A Magneto-Optical Trap (MOT) [29] is used for initial cooling and trapping to capture a large number of atoms with a temperature range of $10 - 1000\,\mu$K. In a MOT, a combination of laser beams and quadrupolar magnetic field simultaneously traps and cools the atoms. Then, the pre-cooled atoms are transferred into a conservative magnetic trap, in our case a Ioffe-Pritchard QUIC trap [30], for radio frequency evaporative cooling [31, 32] until quantum degeneracy. These different stages in the experiment require different vapor pressures. The ^{87}Rb MOT loading requires a higher rubidium vapor pressure (10^{-8} torr) to capture a large number of atoms, while evaporative cooling towards final BEC creation in the QUIC trap requires ultra high vacuum of less than 10^{-11} torr to maintain a long magnetic trap lifetime. The conflict between the two different pressure ranges is solved with a double chamber separated by a tube of low vacuum conductance. In our set-up the two chambers, namely the Upper MOT chamber (at 10^{-8} torr) and the Lower MOT chamber (at 10^{-11} torr) are vertically separated by 75 cm. The two chambers are connected via a small tube of length 120 mm with an internal diameter of only 6 mm which maintains a pressure difference between the two chambers. The

experimental set-up is shown in Figure 2.1.

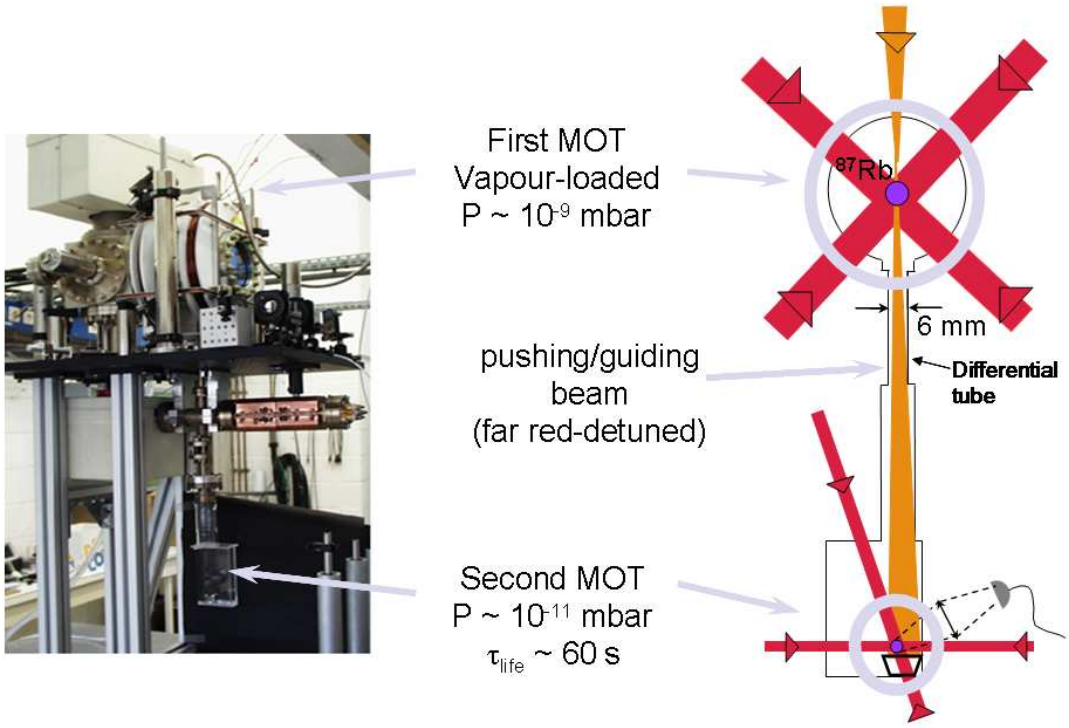

Figure 2.1: Scheme and picture of the vacuum chamber

.

2.1.1 Upper MOT

In the Upper MOT chamber the ^{87}Rb atoms are collected from a vapor in a standard magneto-optical trap (MOT) by three retro-reflected beams ($1/e^2$-diameter of 25 mm each with a total power of 45 mW). This MOT acts as a reservoir for the second MOT in the lower cell.

2.1.2 Transfer of atoms into Lower MOT

The atoms are continuously transferred into the second cell by an original method combining pushing and guiding the atoms [33]. The pushing beam has a power of 21 mW and is detuned by 1.5 GHz on the red side of the MOT $^5S_{1/2}, F = 2 \longleftrightarrow ^5 P_{3/2}, F = 3$ transition. It is focused 8 cm above the upper MOT to a waist of 220 µm such that its radius is 250 µm at the upper MOT and 940 µm at the lower MOT. In the upper MOT region this beam induces a sufficiently large light shift (30 MHz) so that atoms inside the beam no longer feel the MOT beams; the atoms are extracted from the upper MOT with a radiation pressure about 25 times smaller than that of a typical MOT. The advantage of this method is that the velocity of the atoms remains in the capture range of the lower MOT (about $15\,\mathrm{m}\cdot\mathrm{s}^{-1}$). Furthermore, the pushing beam acts as a dipole trap which guides the atoms vertically inside the small diameter tube. The depth of this guide is about 1.4 mK at the upper MOT for the $F = 2$ state. Due to the divergence of the guiding beam the radiation pressure as well as the dipole force at the position of the lower trap are negligible. The fact that the atoms are guided while pushed towards the lower cell renders the loading process very robust against small changes in the parameters of the two MOTs. For detailed description of this pushing and guiding beam I refer to appendix A of the previous dissertation by O. Morizot [28] and to the article [33].

2.1.3 Achieving BEC in the Lower chamber

The Lower MOT is set up with six independent laser beams with a $1/e^2$-diameter of 10 mm each for a total power of 45 mW. After 30 s of loading into the lower MOT, the atoms are cooled by molasses cooling, compressed and pumped into the $F = 2, m_F = 2$ state. They are then transferred into a Ioffe-Pritchard, cigar-shaped magnetic trap (Figure 2.2). We achieve Bose-Einstein condensation after 30 s of rf evaporative cooling in this trap. The number of atoms is deduced from the optical density and the cloud size measured by absorption imaging by sending a probe laser beam through the ultracold atoms. The imaging system is explained in the section 2.5 of this chapter.

2.2 Magnetic QUIC trap

The coils producing the magnetic field in the Lower MOT are arranged in a quadrupole-Ioffe configuration (QUIC) [30] (Figure 2.2). It consists of two identical quadrupole coils and one Ioffe coil. A current I_q through the quadrupole coils produces a spherical quadrupole trap in the center of the two coils. The trap is converted into the QUIC trap by turning on the current I_i through the Ioffe coil. While increasing the current I_i the magnetic zero of the quadrupole is shifted towards the Ioffe coil and a second zero appears in the magnetic field, resulting in a second quadrupole trap in the vicinity of the Ioffe coil. When the current I_i approaches I_q the two spherical quadrupole traps merge and a trap with non-zero magnetic minimum is formed. At the minimum of the trapping potential the field of the Ioffe coil and the field of the quadrupole coils almost cancel each other.

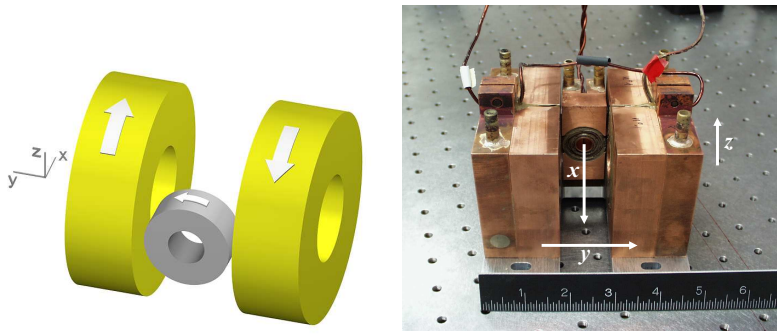

Figure 2.2: Schematic representation of the QUIC trap (left). It is constituted of three coils; two quadrupolar coils (big, face to face) and one so called Ioffe coil (small). This coil is responsible for the presence of a non-zero local minimum of the magnetic field located where the gradients created by the 3 coils along the Ioffe coil axis exactly cancel. The currents in the quadrupole and in the Ioffe coil flow according to the direction of the arrows. We label x-axis the axis of the Ioffe coil, y-axis the quadrupole axis and z-axis the vertical direction pointing upwards. Photograph of the QUIC coils (right). (The photograph shown here was taken in the previous configuration of our QUIC coils arrangement. The dimensions shown in the picture are changed, In our current configuration the quadrupolar coils are slightly more apart from each other compared to the picture.)

The QUIC trap presents a non-zero magnetic minimum $B_{\min}$; this is compulsory to avoid Majorana flips. The magnetic field produced by the QUIC coils at position $\mathbf{r}(x, y, z)$ is expressed by

$$\mathbf{B_{dc}}(\mathbf{r}) = (B_{\min} + \frac{b''}{2}(x^2 - \frac{[y^2 + z^2]}{2}))\,\mathbf{e}_x + (b'y - \frac{b''}{2}xy)\,\mathbf{e}_y + (-b'z - \frac{b''}{2}xz)\,\mathbf{e}_z. \quad (2.1)$$

The origin is taken at the center of the QUIC trap. x is the axis of the Ioffe coil, z the vertical axis and y the second horizontal axis. The corresponding oscillation frequencies are given by

$$\omega_x = \sqrt{\frac{\mu b''}{M}} \quad (2.2)$$

and, if $b'^2 \gg b'' B_{\min}$,

$$\omega_{y,z} = \sqrt{\frac{\mu b'^2}{M B_{\min}}}. \quad (2.3)$$

where μ is the magnetic moment and M is the mass of the atoms.

2.3 Procedure for optimal coils arrangement

In this section a description is given on the alignment of the magnetic QUIC coils with respect to the ultra high vacuum chamber. This geometric arrangement is critical for

having the same current in all three coils, which limits the effect of current fluctuations. The aim of the following procedure is to have a QUIC with $B_{\min}$ of about 2 G at 10 mm from the Ioffe coil end. This 10 mm distance is chosen to avoid any contact between the ultra cold atoms and the inner wall of the cell. The cell wall thickness has a width of 5 mm, see Figure 2.3. To obtain these figures we have followed a step by step procedure.

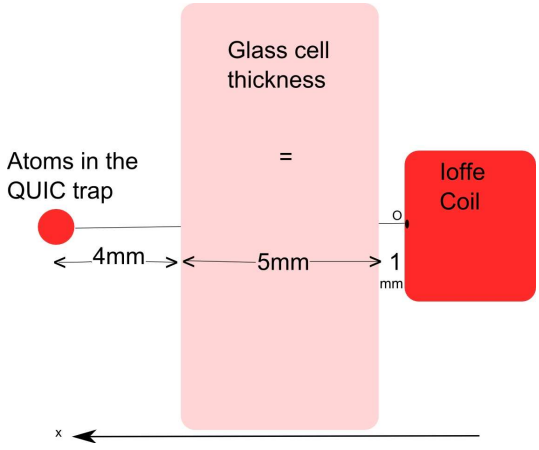

Figure 2.3: The 10 mm distance between the QUIC centre and the Ioffe coil is chosen to avoid any contact between the ultracold atoms and the cell wall. For the measurements, the origin of the x-axis is taken at the point O on the Ioffe coil.

Step 1: Compensation box for the measurements

All the measurements are done inside a magnetic field compensation box which nullifies the Earth and stray magnetic fields. This compensation coils were made and tested before starting the optimization.

Step 2: Matching the axis of magnetic coils

It is important to ensure that the center of the quadrupole field is placed on the axis of the Ioffe coil (the x-axis). In the following measurements the origin of the x-axis is taken at the Ioffe coil. The axis of the magnetic coils is the locus of all the points in the xz plane where B_z goes to zero. A magnetic longitudinal probe is mounted vertically on a translation stage and it is translated along z to find the position $z_0(x)$ where B_z goes to zero for a particular value of x. This experiment is repeated for different values of x and the graph $z_0(x)$ is plotted on Figure 2.4 (left) for different field configurations.

1. Ioffe coil on, quadrupole coils off
2. Ioffe coil off, quadrupole coils on
3. Both Ioffe and quadrupole coils on

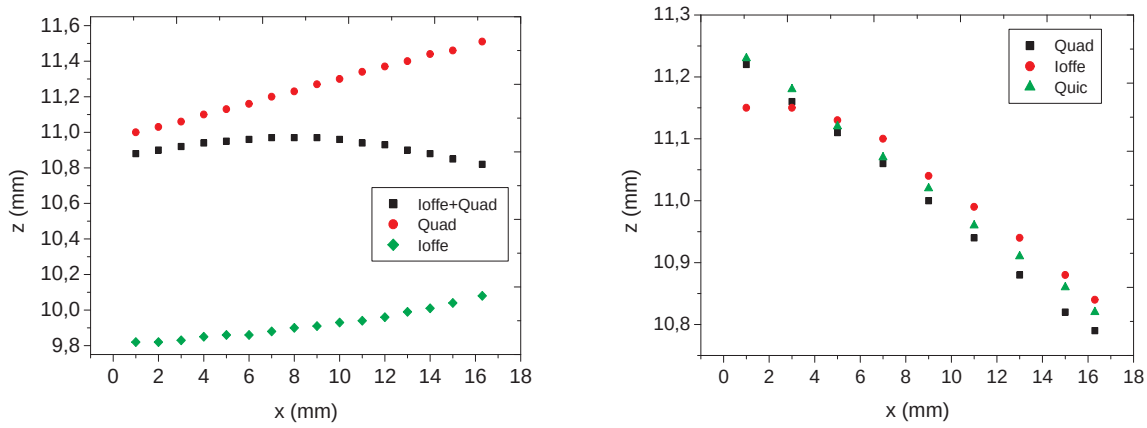

Figure 2.4: Left: Mismatch between the Ioffe and quadrupolar coil axis. Right: Mismatch corrected by raising the Ioffe coil by 1 mm. This measurement was done at a current of 9 A through the coils.

It is clear from the graph that in this first try, the axis of Ioffe and Quad do not match and are apart by a distance of 1.2 mm. This was corrected by modifying the mechanical mount to raise the Ioffe coil by 1 mm. The resulting field is shown on Figure 2.4 (right). The axis of the Ioffe and Quad coils are now matched. The tilt in this axis of about 1.7° with respect to the translation axis of the probe may be due to a small mismatch between the axis of measurement of the magnetic field and the translation axis of the magnetic probe.

Step 3: Finding the vertical position of the Ioffe coil axis using a horizontal probe

For the measurement of the magnetic field along the x-axis it is very important to place the magnetic probe on the axis of the Ioffe coil. To find the position of the axis of the Ioffe coil with the horizontal probe oriented along x, we pass current through the Ioffe coil only and perform a magnetic field measurement of B_x as a function of z. We find a maximum which corresponds to the axis of the Ioffe coil, see Figure 2.5, due to the term $B_{\min} - \frac{b'' z^2}{4}$ in Eq.(2.1). Once the axis is identified, we keep z constant and measure B_x as a function of x. We have noticed however that this magnetic center does not correspond to the geometric center of the Ioffe coil. This may be due to improper coil windings.

Step 4: Matching the gradients of Ioffe and Quad at the required distance

Once the axis is identified, we keep $z = 0$ constant and measure the magnetic field produced by the Ioffe coil $B_{Ix}(x, 0)$ along the x-axis as a function of x. For the QUIC trap centre to be at 10 mm from the Ioffe coil we need that the magnetic gradient of the Ioffe coil $b'_i(x)$ and the quadrupole coils b'_q (note that b'_q does not depend on x) cancel at this point, $b'_q = -b'_i(x_0)$. We fit the recorded data by a third order polynomial function $B_{Ix} = A_0 + A_1\, x + A_2\, x^2 + A_3\, x^3$. The gradient is the derivative of this polynomial

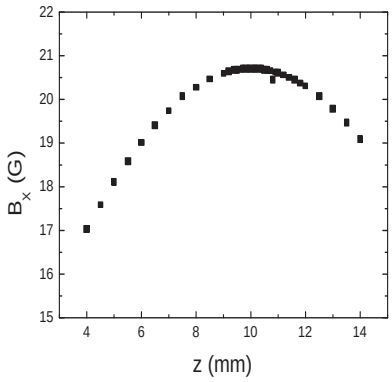

Figure 2.5: B_x v/s z is plotted to find the vertical position of the Ioffe coil axis. The measurement was done at a current of 9 A through the Ioffe coil.

function $b'_i(x) = A_1 + 2A_2\,x + 3A_3\,x^2$ and is equal to -2.88 G/mm at $x_0 = 10$ mm for 9 A. Now the next step is to adjust the distance between the Quad coils in such a way that we recover the opposite gradient for the quadrupole trap, $b'_q = -b'_i(x_0)$ with the same current. After this step, we have a total magnetic field B_{Tx} extremum at the desired distance from the Ioffe coil. This total magnetic field is given by $B_{Tx} = B_{Qx} + B_{Ix}$ the sum of the magnetic fields due to quadrupole and Ioffe coils. We now have to adjust the magnetic field value at this position.

Step 5: Achieving the desired $B_{\min}$

This is done by translating the Ioffe coil along the x-axis by monitoring the magnetic field with the gaussmeter. This maintains the distance between the QUIC center and the Ioffe coil, imposed by the value of the gradient matching b'_q. After choosing an optimum position for the Ioffe coil giving a minimum around 2 G, we plotted B_x v/s x and found $B_{\min}$ to be 1.87 G, see Figure 2.6. We also recorded B_z v/s z at the final position and measured the gradient $b' = 241$ G/cm, see Figure 2.7.

From the fittings, we know $B_{\min}$, b' and b''. Equations (2.2) and (2.3) give us the expected oscillation frequencies $\nu_x = 20.1$ Hz and $\nu_z = 225$ Hz.

2.4 Measurement of the oscillation frequencies

The longitudinal and transverse oscillation frequencies of QUIC trap can be measured respectively by dipolar and parametric excitation of the ultracold atoms. To do this experiment we use an excitation coil of 7 cm diameter and 20 loops made of a copper wire of diameter 0.56 mm. This coil is mounted at a distance of 7.5 cm from the ultracold atoms along the Ioffe coil axis. To measure ν_x a sinusoidal signal of amplitude $A_{mod} = 10\,\mathrm{V_{pp}}$ and frequency ν_{mod} close to the theoretical value of $\nu_x = 20$ Hz is applied through the coil during $t_{exc} = 3$ s using a Stanford DDS synthesizer. The experiment is repeated for various values of ν_{mod} close to $\nu_x = 20$ Hz per increment of 50 mHz. Each

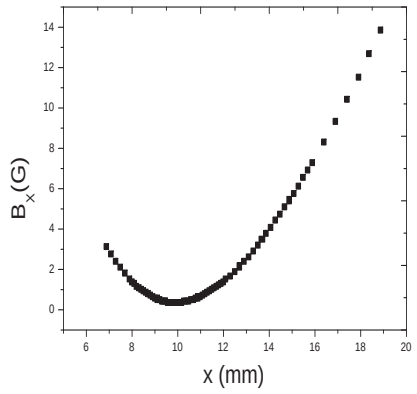

Figure 2.6: B_x v/s x is plotted and this shows the magnetic minimum $B_{\min} = 1.87\,\mathrm{G}$ at a required distance of 10 mm from the Ioffe coil. The measurement was done at a current of 9 A through the three coils.

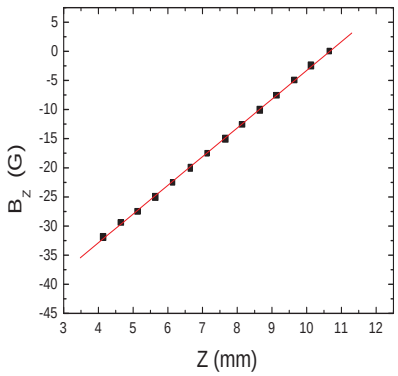

Figure 2.7: B_z v/s z is plotted to obtained the gradient in the vertical direction at the final position.

time the displacement δx of the cloud after 15 ms of time of flight is recorded. We fit the x values with a dispersion curve, from which $\nu_x = 20.175\,\mathrm{Hz}$ is deduced.

To measure ν_z, a sinusoidal signal of amplitude $A_{mod} = 4\,\mathrm{V_{pp}}$ and frequency ν_{mod} is applied during $t_{exc} = 1s$, since $\nu_z \gg \nu_x$ the experimental sequence is repeated by an increment of step 2 Hz around the theoretical value of $\nu_{mod} = 2\nu_z$. The effect of the modulation is observed on the expansion of the atomic cloud near to the resonance after 15 ms of time of flight. We observe a narrow Gaussian response centered at $\nu_{mod} = 402.48\,\mathrm{Hz}$ with a standard deviation $\sigma_{\nu_{mod}} = 4.29\,\mathrm{Hz}$, from which we deduce the value of $\nu_z = \frac{\nu_{mod}}{2} = 201\,\mathrm{Hz}$ (Figure 2.8). There is a discrepancy in the measured values and the predicted value of ν_z. A discrepancy can arise in the measured value, if we are in the non-harmonic regime of the QUIC trap. This can happen if the thermal width of the atomic cloud given by v_z/ω_z exceeds the characteristic size $B_{\min}/b'$ around

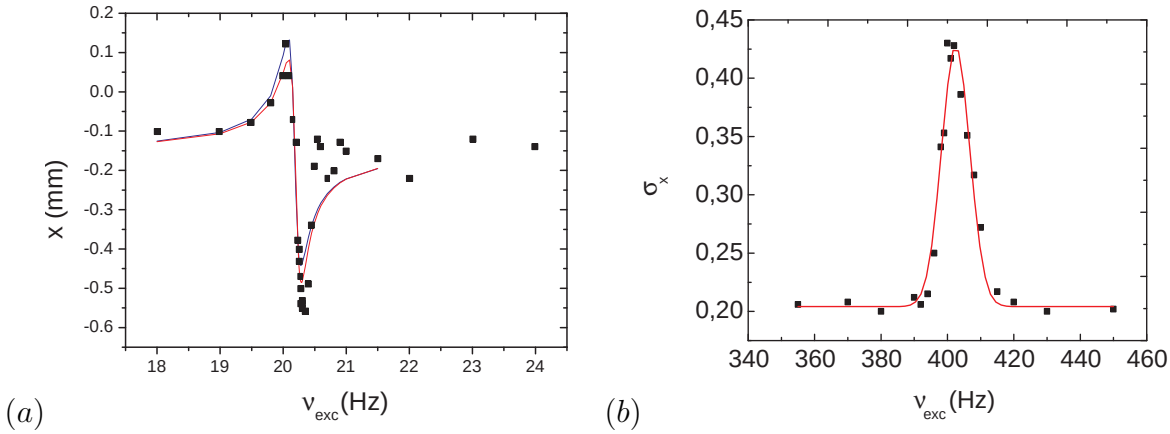

Figure 2.8: Oscillation frequencies measured with the dipolar and parametric excitations of the atoms. (a) Dipolar excitation: The movement of the atoms along the x axis is excited at a frequency ν_{mod}. The displacement of the center of mass of the cloud δx after a 20 ms time of flight plotted for different values of ν_{mod}. We fit the curve with a dispersion curve, from which we deduce the value of $\nu_x = 20.175$ Hz. (b) Parametric excitation: The transverse breathing mode of the trapped atoms is excited at a frequency ν_{mod}. We plot the vertical radius at $1/e^2$ of the cloud σ_z after 20 ms of ballistic expansion for different values of ν_{mod}. We fit the curve with a Gaussian centered at $\nu_{mod} = 402.48$ Hz with a standard deviation $\sigma_{\nu_{mod}} = 4.29$ Hz, from which we deduce the value of $\nu_z = \nu_{\frac{mod}{2}} = 201.24$ Hz.

the minimum at $z = 0$ where the trap is harmonic. We found that in our measurements we were well inside the harmonic regime as the thermal width is less by a factor of 4.3 with respect to the characteristic size[1]. Thus a reason for this discrepancy is not well understood.

2.5 Imaging system for the BEC experiment

In order to obtain high quality images of the atoms, we need a clean uniform probe beam without any fringes. In the previous imaging system used in the experiment, the cleaning of the probe beam was done using a pinhole of 20 µm diameter. But this technique was not efficient enough to give us a clean probe beam, see Figure 2.9 (*a*). We then implemented an optical fiber to couple the probe beam with an efficiency of 75 % and used this beam for imaging. The use of an optical fiber allows to preserve the beam quality up to the vacuum chamber, see Figure 2.9 (*b*).

[1]In our case near to the resonance peak, thermal width $v_z/\omega_z = 17$ µm, where v_z is the thermal velocity deduced from the time of flight measurement and $B_{\min}/b' = 78$ µm.

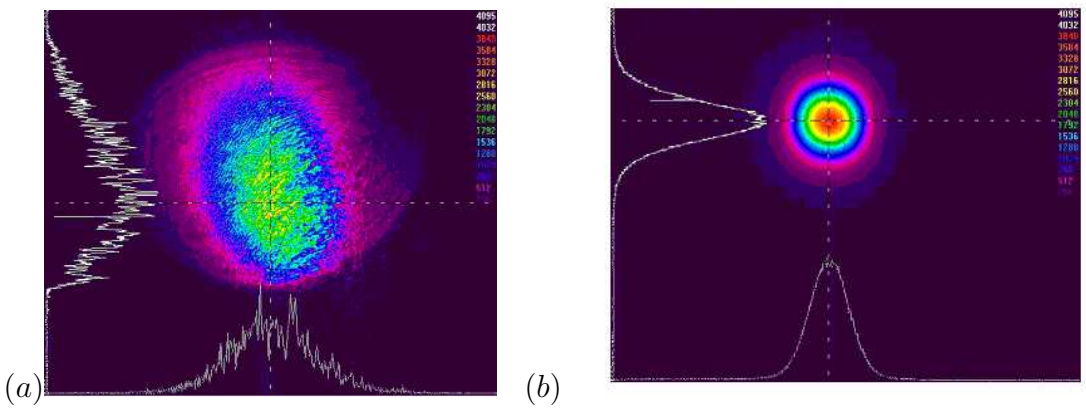

Figure 2.9: (a) Probe beam after the pinhole. (b) Probe beam at the fiber output.

2.5.1 Optical fiber coupling

To achieve an efficient coupling, the beam waist at the input of the coupler should be optimum. We use an OZ optics optical fiber for coupling. From the specifications given in the OZ optics manual the optimum beam waist is in the range $300 - 500\mu$m for an efficient coupling. To have an astigmatic free and optimum size beam we used a cylindrical lens ($f = 200$ mm) and a telescope with two lenses of focal lengths $f' = 150$ mm and $f'' = 75$ mm. The optical set up is sketched on Figure 2.10. Using this shaped beam, we obtain a coupling efficiency of 75 % into the optical fiber, defined as the ratio of the output intensity over the input intensity. The beam waist was analyzed directly using a beam profiler. The distance between f_1 and f_2 is adjusted in such a way that the beam waist at the input of the fiber is 300 mm.

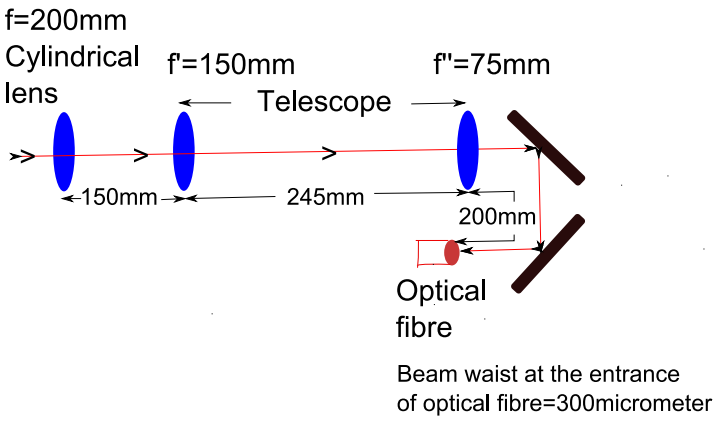

Figure 2.10: Schematic diagram of the optical fiber coupling set up.

2.5.2 Imaging system

The beam at the output of the optical fiber was analyzed using a beam profiler. We obtain a much better beam profile than with the former pinhole set up, as can be seen on Figure 2.9 (*b*). For preserving the beam quality at the output of the fiber, the use of an aspheric lens is essential. After using an aspheric lens ($f_1 = 2.2\,\text{mm}$) we get a fringe free probe beam. After this lens we use an additional telescope with two lenses of focal lengths $f_2 = -30\,\text{mm}$ and $f_3 = 150\,\text{mm}$ to have a 10 mm diameter collimated beam, see Figure 2.11. This collimated beam is sent in the y-direction through the

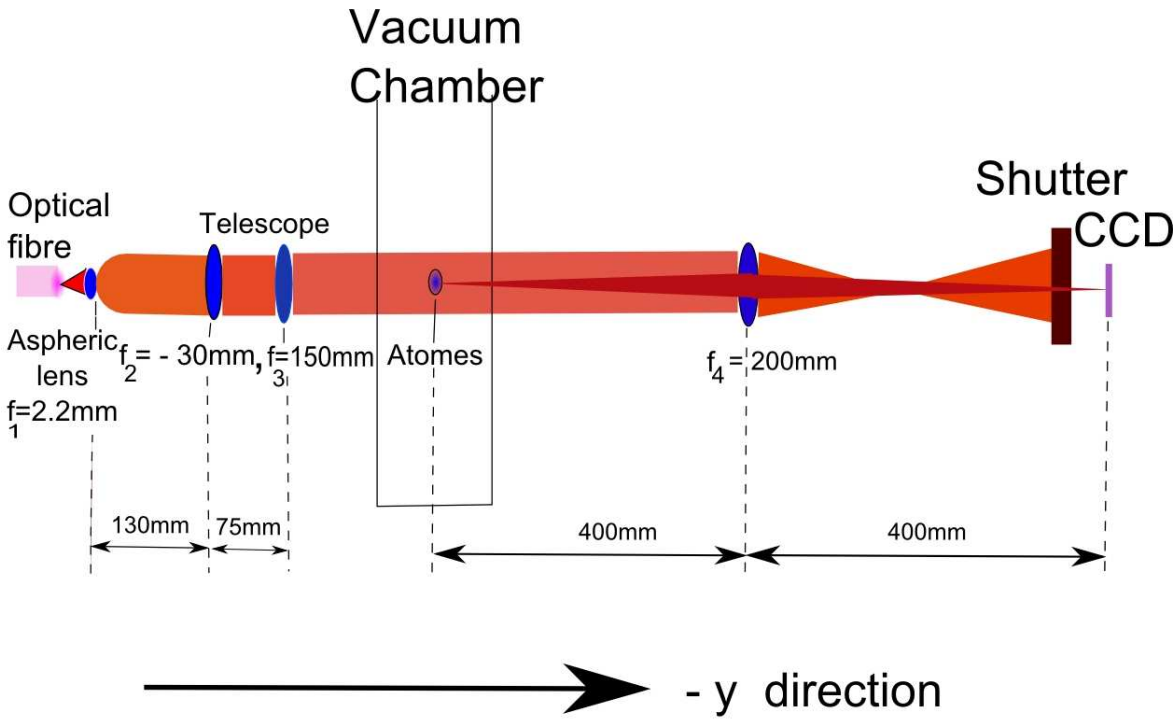

Figure 2.11: Imaging set up along the horizontal direction $-y$: The probe beam propagating from the left to the right is first collimated to a 10 mm diameter beam by using a telescope and then partially absorbed by the prepared atomic cloud whose shadow is imaged on the CCD sensor by a biconvex lens, with a magnification $\gamma_y = -1$.

quartz cell and is partially absorbed in the areas where it encounters the atomic cloud. The shadow of the atomic cloud is then imaged on the CCD sensor by an achromatic biconvex lens with a magnification of $\gamma_y = -1$. The number of atoms, the optical density, the cloud size can be deduced from this absorption images recorded by the CCD camera. This is well explained in the annex of Y. Colombe's thesis [27].

2.6 Experimental set up for producing the radiofrequency fields

In this section, I will explain the experimental set up used for generating the radio frequency fields needed in the experiment. Radio frequency fields are used in our cold atom experiments for different purposes like:

1. Evaporative cooling performed in a magnetic trap which relies on rf field coupling between the different atomic magnetic states [34],
2. rf fields are used together with static fields for trapping ultracold atoms at a temperature of a few μK in a very anisotropic trap [22],
3. and for the spectroscopic investigation and evaporative cooling of this magnetic trap dressed with a rf field [35].

The schematic outline of the experimental set up for producing radio frequency fields and various radio-frequency related components are shown in Figure 2.12.

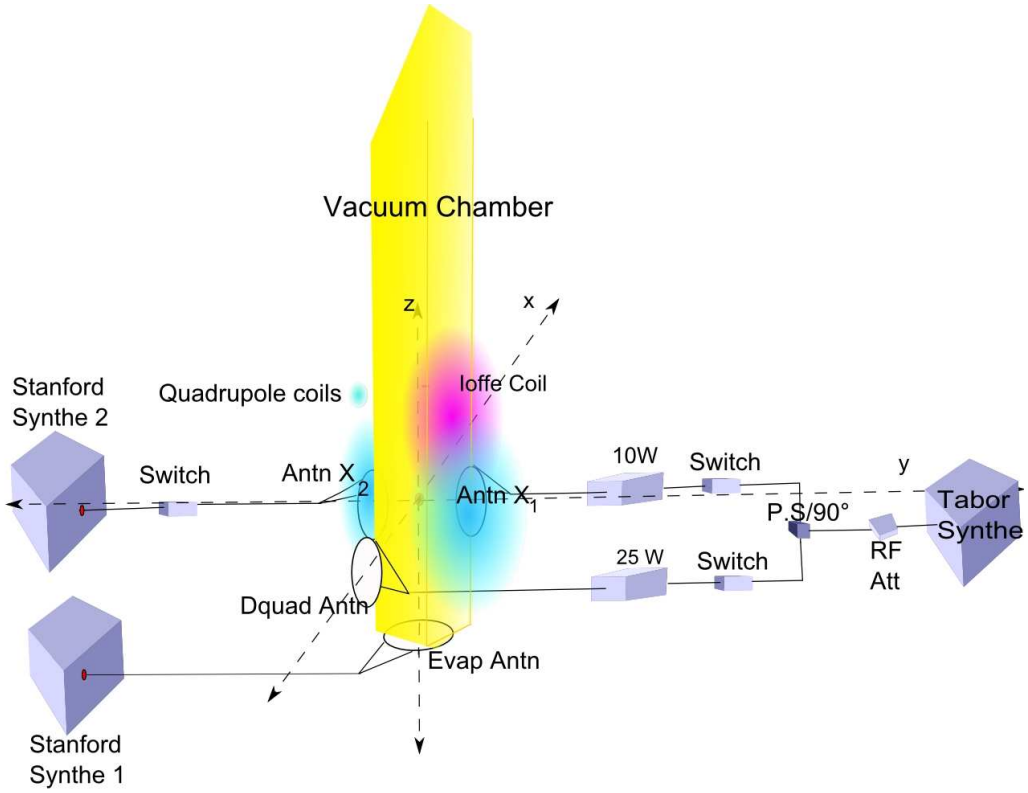

Figure 2.12: Schematic outline of the radio-frequency set up used in the experiment

2.6.1 Description of various radio-frequency related components used in the experiment

The various radio-frequency related components used in this experiments are rf antennas, rf synthesizers, rf attenuators, rf power amplifiers and switches.

Rf antennas We use 4 different rf antennas in this experiment. Characteristics and purpose of these antennas are explained in the table 2.1.

Table 2.1: Characteristics and properties of the different antennas used in the experiment.

rf antenna	No.of loops	Dimensions	Purpose	Polarization properties	Position
Evap antenna	8	Rectangular 7 cm×9 cm	evaporative cooling in the QUIC trap down to BEC	Linearly polarized rf oriented in the z direction	5 cm below the QUIC center
antenna X_1	9	Circular diameter = 3 cm	loading the atoms into a dressed QUIC trap	Linearly polarized rf oriented in the y direction	+1.5 cm from the QUAD center
antenna X_2	9	Circular diameter = 3 cm	evaporative cooling in the dressed QUIC trap and rf spectroscopy	Linearly polarized rf oriented in the y direction	−1.5 cm from the QUAD center
D Quad antenna	9	Circular diameter = 8 cm	Production of a dressed quadrupole trap	Linearly polarized rf oriented in the x direction. This antenna is used with ant. X_1 antenna to give a circular polarization along z	4.7 cm from the QUIC center

Rf synthesizers We use three DDS rf synthesizers in this experiment, the WW1072 synthesizer from Tabor electronics and two identical Stanford DS345.

1. Tabor1072

Tabor 1072 is used for loading the atoms into a dressed QUIC trap. For performing this experiment we operate the 1072 in the arbitrary FM mode. The way to 'talk' to the instrument is by installing a software package called Arb connection which is supplied with 1072. This provides a user interface with a familiar windows interface, which allows the user to interact and control the 1072 directly. The 1072 is controlled from remote using a LAN interface. The required arbitrary frequency sweep to load the atoms into a 2D trap is downloaded into a separate and dedicated memory of the 1072 device. It can be programmed to have a variable length (10 to 20,000 points) and has a separate and independent sample clock control (9 digits,1 mS/s to 2 MS/s).

2. Stanford DS345

   We use two identical Stanford DS345, Stanford 1 and Stanford 2 in this experiment. Stanford 1 is used for evaporative cooling in the dressed QUIC trap and for rf spectroscopic studies whereas Stanford 2 is used for evaporative cooling in a magnetic trap down to BEC. For performing an evaporative cooling we operate the DS345 in FM mode and use the programmed logarithmically decreasing ramp. For the detailed description of the computer controlled sequences refer to chapter 2.4 (Le contrôle informatique des séquences)of Y. Colombe's thesis [27].

Rf attenuators, rf amplifiers and rf switches In order to control the rf amplitude, a programmable rf attenuator Mini circuits ZAS-3 is driven by an analog output channel of a National Instrument PC card PCI- 6713. At the output of the attenuator, the rf signal is amplified by a HD Communications Corp. class-AB amplifier HD19168. Its gain is 40 dB and its noise figure is typically +7 dB according to the manufacturer specifications. This 40 dB amplifier with attenuator is used for dressing the atoms in the QUIC (connected to X_1 antenna in the $-y$ direction). For dressing the QUAD we need a circularly polarized rf so after attenuation we split and phase shift by 90 degrees using a rf splitter/Phase shifter (Pulsar microwave QE-12-442B), one branch goes to the antenna X_1 through the 40 dB amplifier and the second branch goes to the D Quad antenna through another 44 dB amplifier. After the splitting and the phase shifting stage we have two rf switches Mini circuit ZASWA-2-50DR on both the branches to cut the rf whenever it is not needed. A rf switch is also used before the X_2 evaporation antenna, see Figure 2.12.

Chapter 3

Ultracold atoms confined in a radio-frequency dressed magnetic trap

The trapping of ultra cold atoms into an anisotropic quasi two dimensional trap based on rf induced adiabatic potentials was proposed by O. Zobay and B. M. Garraway [21] in 2001 and experimentally realized in 2003 by Y. Colombe *et al.* [22] et al. This trap relies on the rf coupling between the Zeeman sub levels in an inhomogeneous static magnetic field. A static trapping magnetic field presenting a local minimum is used together with a rf oscillating magnetic field. The rf field couples the Zeeman substates $|F, m_F\rangle$ and $|F, m'_F\rangle$ with $m_{F'} = m_F \pm 1$ at the positions where the rf wave is resonant. This results in a dressing of the m_F levels into adiabatic states whose energies depends on position, as represented on Figure 3.1. This creates an adiabatic shell potential for the atoms located on an iso magnetic surface surrounding the minimum of the static magnetic field. The atoms gather at the bottom of this shell due to gravity. This yields a quasi two dimensional trap for an ultra cold atomic vapor, with an oscillation frequency much larger in the direction transverse to the shell than in the two other directions.

In the following sections, I give a theoretical background for the adiabatic potentials and then I describe the experimental procedure for loading atoms into this radio-frequency trap. Finally, I present the oscillation frequency measurements and the Stern-Gerlach technique used to measure the rf coupling strength.

3.1 Hamiltonian of the system

The ^{87}Rb atoms are confined in a QUIC magnetic trap produced by an inhomogeneous dc magnetic field $\mathbf{B_{dc}}(\mathbf{r})$, see Eq.(2.1). The atomic cloud trapped in this configuration is anisotropic and cigar-shaped along x, which is the direction of the offset magnetic field produced by the Ioffe coil. In the following, the axes in the lab frame will be

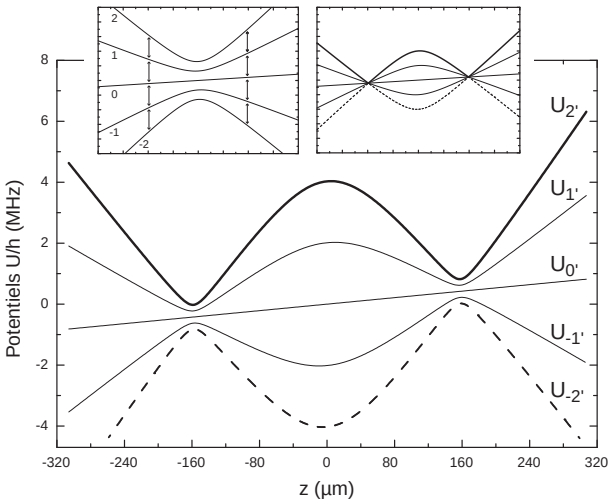

Figure 3.1: Plot along z of the adiabatic potentials for the five rf-dressed Zeeman substates of ^{87}Rb in $^5S_{1/2}$, F = 2 in the QUIC magnetic field, when gravity is taken into account.

labeled by the lower case letters x, y and z. As already mentioned in chapter 2, the z axis is in the vertical direction and y is the horizontal direction perpendicular to the cigar axis. The direction of the DC magnetic field is not the same everywhere. One thus defines X, Y and Z the axes of the local frame attached to the static magnetic field, Z being the direction of the dc magnetic field and X the direction of polarisation of the rf field, assumed to be always perpendicular to Z. This is justified in the QUIC trap geometry, where the magnetic field at the position of the atoms belongs to the $x-z$ plane and the rf field is polarized along y.

The Larmor frequency of the atomic spin precession in the dc field is denoted by $\omega_0(\mathbf{r}) = g_F\mu_B B_{dc}(\mathbf{r})/\hbar$, where g_F and μ_B are the Landé factor and the Bohr magneton, respectively. The antenna X_1 produces a radio frequency field of frequency ω_1. The total magnetic field experienced by the atoms consists of two terms

1. one coming from the inhomogeneous d.c magnetic field $\mathbf{B_{dc}}(\mathbf{r}) = B_{dc}(\mathbf{r})\hat{\mathbf{e}}_Z$ of the QUIC trap

2. a second term oscillating at the frequency ω_1, $\mathbf{B}_1(\mathbf{r},t) = B_{01}\hat{\mathbf{e}}_X\cos(\omega_1 t)$, responsible for the adiabatic trapping potential.

B_{01} is the amplitude of the field whereas $\hat{\mathbf{e}}_X$ and $\hat{\mathbf{e}}_Z$ are unit polarization vectors. Using these definitions and denoting by $\mathbf{F}$ the atomic angular momentum operator, the total Hamiltonian of the atom-spin interaction $H_T(\mathbf{r},t)$ is:

$$H_T(\mathbf{r},t) = \frac{g_F\mu_B}{\hbar}\mathbf{F}.[\mathbf{B_{dc}}(\mathbf{r}) + \mathbf{B_1}(\mathbf{r},t)]. \tag{3.1}$$

Since we assume that at every point $\mathbf{r}$, X is perpendicular to Z, Eq.(3.1) takes the form:

$$H_T(\mathbf{r},t) = \omega_0(\mathbf{r})F_Z + V_1(\mathbf{r},t). \tag{3.2}$$

$V_1(\mathbf{r},t)$ is defined by the expression

$$\begin{aligned} V_1(\mathbf{r},t) &= 2\Omega_1(\mathbf{r})F_X\cos\omega_1 t \\ &= \Omega_1(\mathbf{r})F_X(e^{i\omega_1 t}+e^{-i\omega_1 t}) \end{aligned} \tag{3.3}$$

and $\Omega_1(\mathbf{r}) = g_F\mu_B B_{01}/(2\hbar)$ is the Rabi frequency of the rf field.

3.2 Spin evolution

Given $H_T(\mathbf{r},t)$, the dynamics of an atomic spin state $|\phi(\mathbf{r},t)\rangle$ is governed by the Schrödinger equation:

$$i\hbar\frac{\partial}{\partial t}|\phi(\mathbf{r},t)\rangle = H_T(\mathbf{r},t)|\phi(\mathbf{r},t)\rangle. \tag{3.4}$$

In the frame rotating at the frequency ω_1, it yields:

$$ih\frac{\partial}{\partial t}|\psi(\mathbf{r},t)\rangle = [-\delta(\mathbf{r})F_Z + R_1^\dagger V_1(t)R_1]|\psi(\mathbf{r},t)\rangle \tag{3.5}$$

with the detuning $\delta(\mathbf{r}) = \omega_1 - \omega_0(\mathbf{r})$, the rotating frame operator $R_1 = \exp(-i\omega_1 t F_Z/\hbar)$ and the rotated state $|\psi(\mathbf{r},t)\rangle = R_1^\dagger|\phi(\mathbf{r},t)\rangle$. The rotated interaction Hamiltonian $R_1^\dagger V_1(t)R_1$ is given by:

$$\begin{aligned} R_1^\dagger V_1(t)R_1 &= 2\Omega_1\cos\omega_1 t(\cos\omega_1 t F_X - \sin\omega_1 t F_Y) \\ &= \Omega_1(\mathbf{r})F_X + \Omega_1(\mathbf{r})F_X\cos 2\omega_1 t - \Omega_1(\mathbf{r})F_Y\sin 2\omega_1 t. \end{aligned} \tag{3.6}$$

We apply a rotating wave approximation on Eq.(3.6) and we neglect the terms oscillating at frequency $2\omega_1$. Eq.(3.6) becomes:

$$R_1^\dagger V_1(t)R_1 = \Omega_1(\mathbf{r})F_X. \tag{3.7}$$

We find the dynamics of $|\psi(\mathbf{r},t)\rangle$ in Eq.(3.5) to be described by the time independent Hamiltonian:

$$H_A(\mathbf{r}) = -\delta(\mathbf{r})F_Z + \Omega_1 F_X. \tag{3.8}$$

In the presence of the rf field, the eigenstates of the spin are tilted by an angle θ from the Z axis (aligned with the static d.c.magnetic field $\mathbf{B_{dc}}(\mathbf{r})$ of the QUIC trap) and precess around it at the angular frequency ω_1 of the rf wave. The time independent Hamiltonian of Eq.(3.8) can be rewritten in terms of θ, which makes the Hamiltonian more compact and powerful to understand the spin evolution in an analytical way:

$$\begin{aligned} H_A &= \Omega(\mathbf{r})(\cos\theta F_Z + \sin\theta F_X) \\ &= \Omega(\mathbf{r})F_\theta. \end{aligned} \tag{3.9}$$

We have defined $\Omega(\mathbf{r}) = \sqrt{\delta(\mathbf{r})^2+\Omega_1^2}$ and the flip angle θ by

$$\tan\theta = -\frac{\Omega_1}{\delta(\mathbf{r})} \quad \text{with} \quad \theta\in[0,\pi]. \tag{3.10}$$

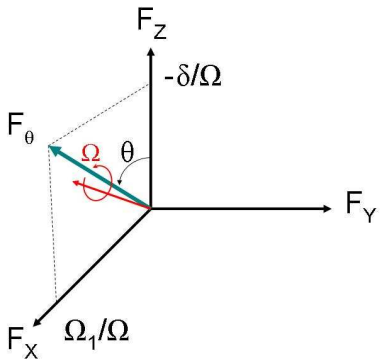

Figure 3.2: At a given location $\mathbf{r}$, δ and Ω_1 define the angle θ by which F_Z is rotated. The spin (red arrow) therefore precesses around an axis given by F_θ (blue arrow) at a frequency Ω.

$F_\theta = \mathbf{F}.\mathbf{e}_\theta$ is then simply the projection of the spin on the direction $\mathbf{e}_\theta = \cos\theta\,\mathbf{e}_Z + \sin\theta\,\mathbf{e}_X$.

Graphically the spin evolution given by Eq.(3.8) is represented in Figure 3.2. At each fixed position $\mathbf{r}$, the spin Hamiltonian H_A can be diagonalized. The eigenstates are the spin states $|m'_F\rangle$ of the rotated spin F_θ. The energy of the m'_F dressed state is equal to

$$\begin{aligned} U_{m'_F}(\mathbf{r}) &= m'_F\hbar\Omega(\mathbf{r}) \\ &= m'_F\hbar\sqrt{\delta(\mathbf{r})^2+\Omega_1^2} \end{aligned} \tag{3.11}$$

The dressed states $|m'_F\rangle$ can be written in terms of bare states basis $|m_F\rangle$ after the application of a rotation operator $|m'_F\rangle = e^{-\frac{i\theta F_Y}{\hbar}}|m_F\rangle$. For example for the extreme state $|2'\rangle \equiv |m'_F = 2\rangle$, we can write:

$$\begin{aligned} |2'\rangle &= \frac{1}{4}(1+\cos\theta)^2|2\rangle + \frac{1}{2}\sin\theta(1+\cos\theta)|1\rangle + \sqrt{\frac{3}{8}}\sin^2\theta|0\rangle \\ &+ \frac{1}{2}\sin\theta(1-\cos\theta)|-1\rangle + \frac{1}{4}(1-\cos\theta)^2|-2\rangle. \end{aligned} \tag{3.12}$$

For the extreme cases of detuning, when $\delta \to \mp\infty$ the dressed state $|2'\rangle$ is equal to the bare state $\pm|2\rangle$. The weight, *i.e.* the square of the amplitude, of each bare substate is plotted as a function of the rf detuning δ in Figure 3.3 below.

3.3 Adiabatic Potentials

The energy and the eigenstates depends on position. If the atomic motion is slow enough, the position-dependent energies can be seen as a potential for the atoms.

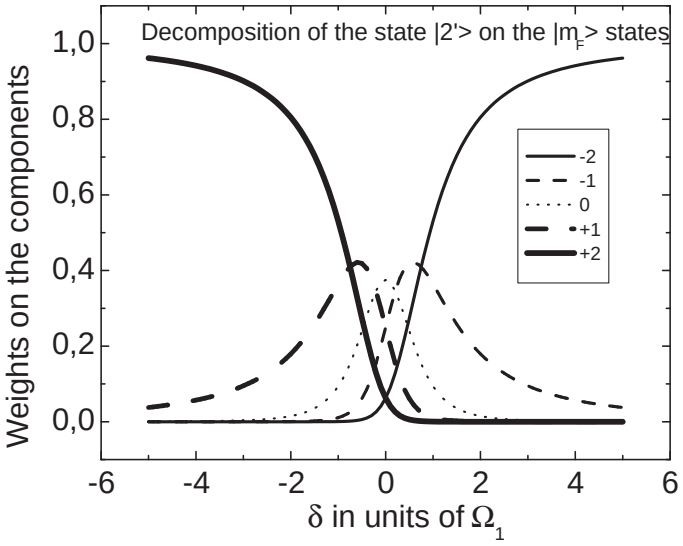

Figure 3.3: Decomposition of the dressed state $|2'\rangle$ in the bare $|m_F\rangle$ basis, for a F=2 hyperfine level. The weight over each bare sub state is plotted as a function of the rf detuning δ, expressed in units of the Rabi frequency Ω_1.

Taking gravity into account, the total potential for the dressed state m'_F reads:

$$U_{m'_F}(\mathbf{r}) = m'_F\sqrt{\delta(\mathbf{r})^2+\Omega_1^2}+Mgz \tag{3.13}$$

$$= m'_F\sqrt{(\hbar\omega_1 - g_F\mu_B B(\mathbf{r}))+\Omega_1^2}+Mgz. \tag{3.14}$$

For the atoms in $m'_F = 2$ dressed state, this potential presents a minimum at the points where[1]

$$\hbar\omega_1 = g_F\mu_B B(\mathbf{r}). \tag{3.15}$$

The locus of these points is the surface where the norm of the magnetic field has a given value or equivalently, an iso-B surface of equation:

$$B(\mathbf{r}) = \frac{\hbar\omega_1}{g_F\mu_B}. \tag{3.16}$$

We will see at section 3.6 that the transeverse confinement to the shell can be quite strong. If, for instance, the d.c. magnetic trapping potential is harmonic, the iso-B surfaces are ellipsoids. The atoms are thus forced to move onto an egg shell, their motion being very limited in the direction orthogonal to the shell, see Figure 3.4. This atomic bubble is not easily observable, because the atoms fall at the bottom of the shell due to gravity. As the typical radius of the shell increases, the atomic cloud becomes essentially two-dimensional. It is this property that will be used in our experiment for creating a quasi-two dimensional trap.

[1]Strictly speaking, there will be a small shift in the z position due to gravity. The correction for z is given by $-\frac{g}{\omega_z^2} \approx -1\,\mu$m which is negligible. Gravity essentially attracts the atoms to the bottom of the iso-B surface.

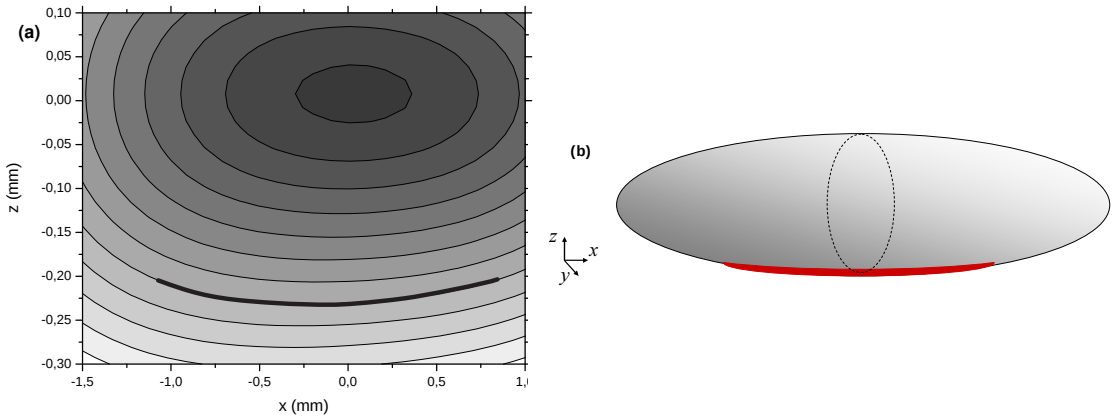

Figure 3.4: (a) Cut of the iso-B surfaces in our QUIC trap in the vertical plane xOz. Two successive iso-B lines are separated by 0.5 G. The thick line represents schematically the atomic distribution of the atoms in the dressed trap in the presence of gravity. (b) 3D scheme of the iso-B surface within which the atoms (thick red line) are trappped.

3.4 Adiabaticity condition

To describe the adiabatic potential the dressed atoms are trapped in, we made the hypothesis that at each point $\mathbf{r}$, the atoms stay in the eigenstate of H_A. This is true only if the motional coupling between dressed states, induced by the kinetic energy term of the total Hamiltonian, is small enough. The adiabaticity condition states that the variation rate $\dot{\theta}$ of the eigenstates of the spin Hamiltonian H_A must be very small as compared to the level spacing $\Omega(\mathbf{r})$ in the dressed basis:

$$|\dot{\theta}| \ll \sqrt{\delta^2 + \Omega_1^2}. \tag{3.17}$$

By differentiating Eq.(3.10), we can find

$$\dot{\theta} = \frac{\Omega_1 \dot{\delta} - \dot{\Omega}_1 \delta}{\delta^2 + \Omega_1^2}. \tag{3.18}$$

Substituting Eq.(3.18) into Eq.(3.17) we get

$$|\Omega_1 \dot{\delta} - \dot{\Omega}_1 \delta| \ll (\delta^2 + \Omega_1^2)^{3/2}. \tag{3.19}$$

This criterion defines the condition under which the spin can follow the change in the effective magnetic field adiabatically. If this condition is not satisfied, non-adiabatic transitions are favored. Note that the adiabaticity criterion is more restrictive on resonance (around $\delta = 0$), where it simplifies to $|\dot{\delta}| \ll \Omega_1^2$.

This adiabaticity condition must be fulfilled both when a change in Ω_1 occurs, for example when the rf field is switched on in the loading stage, and when the detuning is modified, either directly by the experimentalist or by atomic motion in the potential. In this last case, residual motional coupling with a too low Rabi frequency induces Landau-Zener transitions.

3.5 Loading atoms into the radio-frequency trap

Ultra cold atoms or Bose-Einstein condensate are prepared in the QUIC trap in the $|+2\rangle$ bare state. We then switch off the evaporation rf and turn on the trapping rf wave progressively from $\Omega_1 = 0$ to Ω_0 within $t_{on} = 2\,\text{ms}$, at an initial negative detuning δ_i from the QUIC trap bottom $\omega_{\min} = g\mu_B B_{\min}/\hbar$: $\delta_i = \omega_i - \omega_{\min} < 0$ ($\omega_i = 2\pi \times 1\,\text{MHz}$ and $\omega_{\min} = 2\pi \times 1.35\,\text{MHz}$). This ensures that the atoms follow adiabatically the state $|2\rangle$, and, are transferred from the bare state $|2\rangle$ to the final dressed state $|2'\rangle$. The rf frequency is then swept up to the desired value ω_1. Figure 3.5 shows the evolution of the adiabatic potentials during the rf frequency sweep. The graphs are plotted at constant rf coupling strength $\frac{\Omega_1}{2\pi} = 180\,\text{kHz}$, for rf frequencies (a) $\frac{\omega_1}{2\pi} = 1\,\text{MHz}$, (b) 1.3 MHz, (c) 1.5 MHz and (d) 2 MHz. Gravity is taken into account. When $\omega_1 < \omega_{\min}$, the atoms stay approximately at the centre of the QUIC trap and see a varying detuning δ. With typical experimental parameters, the rate $\dot{\delta}$ is low enough to avoid non-adiabatic transitions. When $\omega_1 > \omega_{\min}$, the atoms follow the avoided crossing and see a constant detuning $\delta \cong 0$. The adiabaticity criterion Eq.(3.19) is then fulfilled during the whole loading stage. For the efficient loading of atoms to the dressed trap, we use a typical ramp as shown in Figure 3.6. The rf frequency ω_1 is ramped up from 1 MHz to a final fixed frequency ω_1 ranging from 2 to 10 MHz in 500 ms typically. The frequency is ramped more slowly around 1.3 MHz, corresponding to the resonant frequency at the center of the magnetic trap where adiabaticity of spin rotation is more difficult to obtain.

The series of absorption images shown in Figure 3.7 illustrate the deformation of the atomic cloud as it is transferred into the egg shell trap. Starting from the QUIC trap, the cloud is translated along z when ω_1 increases, and is deformed at the same time: It is compressed in the z direction whereas it is relaxed along x and y.

3.6 Rf dressed trap oscillation frequencies

The oscillations of the atoms in the egg shell trap are not harmonic. However, for small amplitude oscillations, an oscillation frequency can be defined in each direction by making an harmonic approximation near the trap bottom. The oscillation frequency in the strongly confined z-direction can be inferred from the Rabi frequency Ω_1 and the vertical gradient $\alpha(z_0)$ of the static magnetic field in units of frequency, at position z_0. With these notations, the oscillation frequency in the z direction reads:

$$\omega_\perp = \alpha(z_0)\sqrt{\frac{2\hbar}{M\Omega_1}} \tag{3.20}$$

where $\alpha(z_0)$ is defined as

$$\alpha(z_0) = \frac{g_F \mu_B}{\hbar}\,\frac{dB}{dz}(z_0). \tag{3.21}$$

In a QUIC trap, the radial gradient α is constant except in a small region of characteristic size $B_{\min}/b' = 78\,\mu\text{m}$ around the minimum at $z = 0$. The transverse oscillation

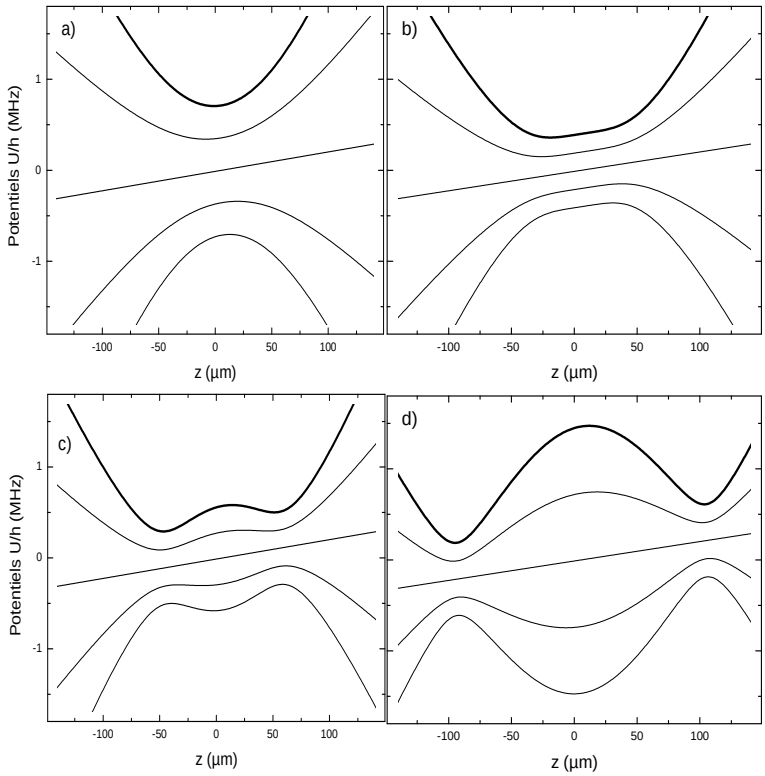

Figure 3.5: Illustration of the trap loading stage : The energy diagram plotted at constant rf coupling strength $\frac{\Omega_1}{2\pi} = 180\,\mathrm{kHz}$, for detunings $(a)\ \omega_1 - \omega_{min} = -1.94\,\Omega_1\,\mathrm{kHz}$, (b) -0.27 Ω_1 kHz (c) 0.83 Ω_1 kHz and (d) 3.61 Ω_1 kHz. For negative detunings as in the case of (a) and (b) atoms stay approximately at the centre of the QUIC trap. The potential starts to get deformed as we cross the resonance and for positve detunings as in the case of (c) and (d) it presents an avoided crossing where the rf wave is resonant with the adjacent $|m_F\rangle$ Zeeman states. At these points, the degeneracy between the dressed states is lifted by the rf coupling that seperates adjacent potentials by an energy $\hbar\Omega_1$. The atoms in the highest $|2'\rangle$ dressed state (bold line) can be trapped in the vicinity of this avoided crossing.

frequency can still be controlled using the Rabi frequency Ω_1. The horizontal frequencies ω_{h1} and ω_{h2} corresponding, respectively, to the x and y directions directly depend on the local shape of the iso-B surface. In the yz plane, due to the axial symmetry of the QUIC trap, the iso-B lines are circles and ω_{h2} is merely the pendulum pulsation

$$\omega_{h2} = \sqrt{\frac{g}{|z_0|}}. \tag{3.22}$$

In the xz plane, the iso-B lines are very elongated due to the cigar shape of the QUIC trap. ω_{h1} is much smaller than ω_{h2} and cannot be expressed analytically. Its order of magnitude is given by approximating the iso-B lines by ellipses:

$$\omega_{h1} = \sqrt{\frac{g}{|z_0|}}\frac{\omega_x}{\omega_z} \tag{3.23}$$

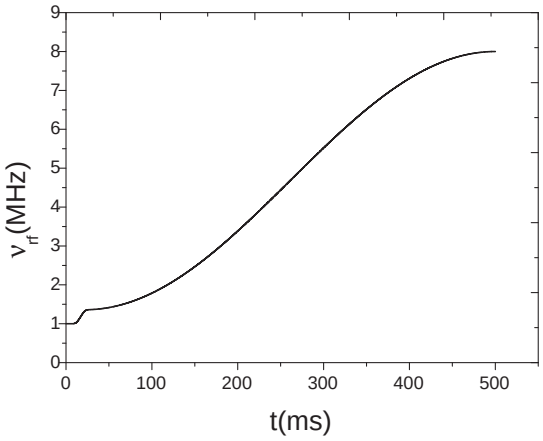

Figure 3.6: Typical shape of a radio-frequency ramp applied to the ultracold atomic sample. In the present example ω_1 is increased from 1 to 8 MHz within 500 ms, after a 12 ms stage where the frequency is maintained at 1 MHz for adiabatic switching of the rf source. At the end of the ramp, the rf frequency is maintained at its final value for some holding time in the rf-based trap

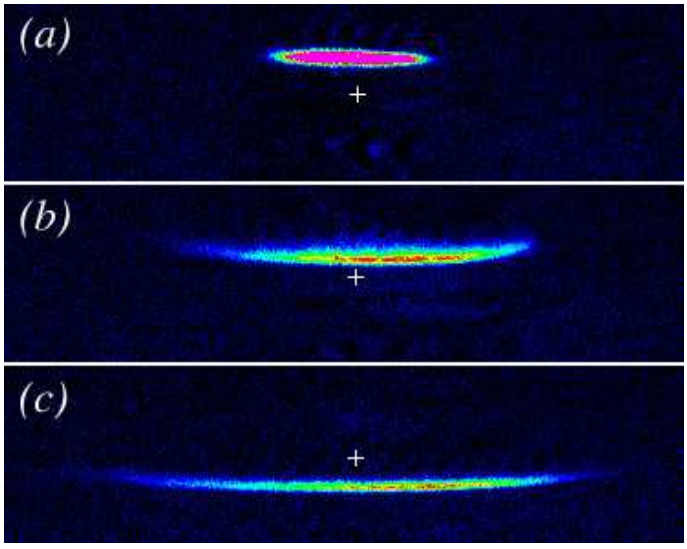

Figure 3.7: Experimental pictures of a cloud of 10^6 atoms at 5 μK trapped inside (a) the QUIC and (b) the dressed trap for $\omega_1 = 2\pi \times 3$ MHz (vertical displacement $z_0 = -130$ μm) or (c) for $\omega_1 = 2\pi \times 8$ MHz (vertical displacement $z_0 = -450$ μm. The dimensions of the pictures are 4.5×1.2 mm. The frame is the same for all the pictures, and the atomic cloud is shifted downwards when ω_1 increases. Figure from Ref. [22].

where ω_x and ω_y are the oscillation frequencies in the bottom of the QUIC trap. As $|z_0|$ increases with ω_1, ω_{h1} and ω_{h2} may be controlled via ω_1 and $\omega_\perp$ via Ω_1; one can find a set of parameters such that $\omega_\perp \gg \omega_{h1}, \omega_{h2}$.

3.6.1 Measurement of the transverse oscillation frequency $\omega_\perp$

We measure the oscillation frequency by displacing suddenly the atomic cloud in the vertical direction and recording the oscillation in its centre of mass velocity. This is done by the application of a rf ramp as shown in Figure 3.8. Atoms are first loaded into the dressed trap and then we suddenly jump to a lower value of the final frequency, the frequency jump being typically $\Delta\omega_1 = 2\pi \times 0.1\,\mathrm{MHz}$. This initiates oscillations in the vertical direction and from the damped sine fitting we deduce the vertical oscillation frequency. The Figure 3.9 shown below gives the experimental results for measurements done at 5 MHz final frequency and for output voltages of $400\,\mathrm{m}V_{pp}$, $200\,\mathrm{m}V_{pp}$ and $50\,\mathrm{m}V_{pp}$ from the Tabor synthesizer. This gives $\omega_\perp = 2\pi \times 545\,\mathrm{Hz}$, $2\pi \times 606.7\,\mathrm{Hz}$ and $2\pi \times 684\,\mathrm{Hz}$ respectively.

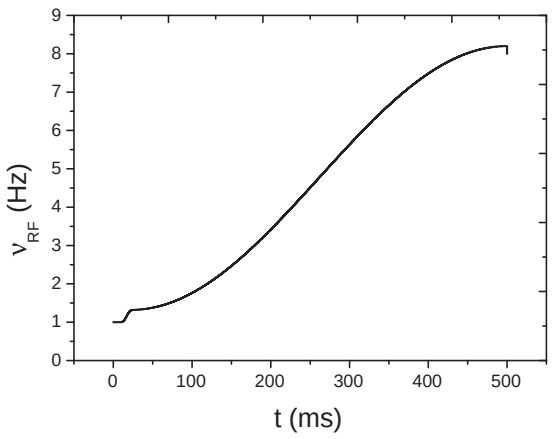

Figure 3.8: (a) Typical shape of a radio-frequency ramp applied to the ultracold atomic sample to initiate vertical oscillations. In the present example ω_1 is increased from 1 to 8.1 MHz within 500 ms. At the end of the ramp, the rf frequency is suddenly changed to a final value of 8 MHz. The centre of mass of the cloud is not located at the trap bottom anymore, and vertical oscillations are initiated.

3.6.2 Measurement of the rf coupling strength Ω_1

The Rabi frequency of the dressing field was calibrated using two different procedures

1. from the oscillation frequency measurement
2. from the Stern-Gerlach experiment.

These two procedures are explained in the following paragraphs.

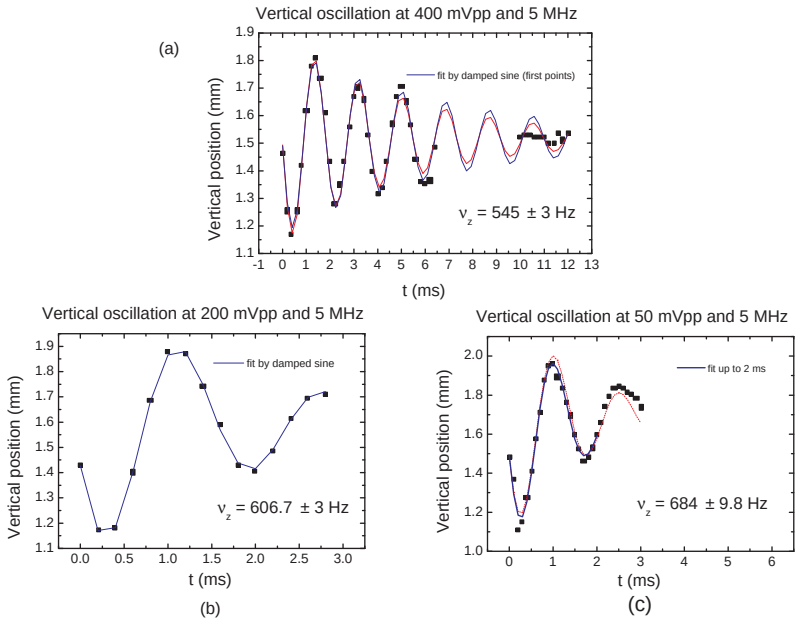

Figure 3.9: Oscillation of the centre of mass of the atomic cloud with time in milliseconds. A damped sine fitting is done and the oscillation frequency is deduced from the fit. Measurements were done for three values of the rf amplitude before the rf amplifier: (a) 400 mV_{pp}, (b) 200 mV_{pp} and (c) 50 mV_{pp} at same final frequency of 5 MHz. This gives $\omega_\perp = 2\pi \times 545$ Hz, $2\pi \times 606.7$ Hz and $2\pi \times 684$ Hz respectively.

3.6.3 From an oscillation frequency measurement

In this method we make use of the relation between the vertical oscillation frequency in the dressed trap and the Rabi frequency Ω_1 Eq.(3.20). By knowing the value of the vertical oscillation frequency and of the magnetic field gradient (measured from the vertical displacement of rf dressed trap) Ω_1 is deduced. For example, from the measured values of $\omega_\perp = 2\pi \times 545$ Hz (from Figure 3.9) and the gradient $b' = 223$ G/cm, we deduce $\Omega_1 = 2\pi \times 192$ kHz. However, a discrepancy between the measured value of the oscillation frequency and the value given at Eq.(3.20) can arise if the oscillation is not in the harmonic regime. To be inside the harmonic regime we need to satisfy two criteria:

1. $\Delta z \ll \frac{\Omega_1}{\alpha}$ or equivalently $\Delta\omega_1 \ll \Omega_1$, where Δz is the shift of the position of the atomic cloud during the sudden change of $\Delta\omega_1$ in the dressing rf frequency. This frequency jump initiates the vertical oscillations. For deducing small values of Ω_1 we should use smaller $\Delta\omega_1$, otherwise we will explore non-harmonic regime and the error in the measured oscillation frequency – and thus in the deduced value of Ω_1 – can be large. In the present example shown in Figure 3.8 $\Delta\omega_1 = 2\pi \times 100$ kHz, to be compared with the deduced value $\Omega_1 = 2\pi \times 192$ kHz.

2. $\sigma_{th} \ll \frac{\Omega_1}{\alpha}$, where $\sigma_{th} = \frac{1}{\omega_\perp}\sqrt{\frac{k_B T_0}{m}}$ is the thermal width of the atomic cloud in the harmonic approximation. After simplifying the above inequality we get $k_B T_0 \ll 2\hbar\Omega_1$, where T_0 is the initial temperature of the atomic cloud. This sets an upper bound for the initial temperature of the atomic cloud for the oscillation frequency measurements to be in the harmonic regime. For example, for $\frac{\Omega_1}{2\pi} = 200\,\text{kHz}$, T_0 should be much less than $20\,\mu\text{K}$.

For the measurements performed here, the first criterion is hardly matched. If the Rabi frequency is less than estimated, the second criterion also is not very well fulfilled. Simulations performed in the group showed that Ω_1 can be overestimated by a factor 3 in our experiment.

3.6.4 From a Stern-Gerlach measurement

In this method we make use of the idea that $|m'_F\rangle$ states can be decomposed in the bare $|m_F\rangle$ basis as discussed in section 3.2. To measure the m_F state decomposition, the rf field is turned on slowly at a fixed frequency ω_i, with $\delta_i < 0$ ($\delta_i = -300\,\text{kHz}$, with a bottom frequency $\omega_{\min} = 2\pi \times 1.3\,\text{MHz}$) to transfer[2] all the atoms from the $m_F = 2$ state to a single dressed state $m'_F = 2$. The rf field is then suddenly turned off to project the dressed state on to the bare $|m_F\rangle$ states. The rf field is turned off 1 ms before the static magnetic field. To make the m_F states well separated we keep the Ioffe bias field on 2 ms more than the quadrupolar field. The atoms are accelerated in the gradient produced by the Ioffe coil, which allows a separation of the magnetic sublevels. Ω_1 can be calculated from the following formula, deduced from Eq.(3.10).

$$\Omega_1 = -\delta_i \frac{\sqrt{\frac{P_1}{P_2}}}{1 - \frac{P_1}{4P_2}}. \tag{3.24}$$

where P_1 and P_2 correspond to the population in $m_F = 2$ and $m_F = 1$ states respectively.

P_1 and P_2 are measured by absorption imaging (see Figure 3.10). Ω_1 is computed to be 200 kHz for an output voltage of $400\,\text{m}V_{pp}$ from the Tabor synthesizer.

3.7 Conclusions

In this chapter, I briefly explained the technique of loading the atoms into the rf dressed trap starting from a static magnetic trap. I also presented two techniques to measure the rf coupling strength. As we will see in chapter 5, however, the value of the Rabi frequency deduced from these measurement is too large with respect to the value deduced from spectroscopic measurements. As pointed out in section 3.6.3, the frequency jump we used was too large with respect to the Rabi frequency. We believe

[2] δ is kept constant at $-300\,\text{kHz}$ throughout the experiment and Ω_1 is ramped slowly enough during t_{on} to transfer all the atoms from $m_F = 2$ state to a single dressed state $m'_F = 2$. $t_{on} \gg \frac{\Omega_1}{\delta^2}$ from the adiabaticity condition Eq.(3.19). See also Ref. [28] page 70. In our case $t_{on} = 12\,\text{ms}$.

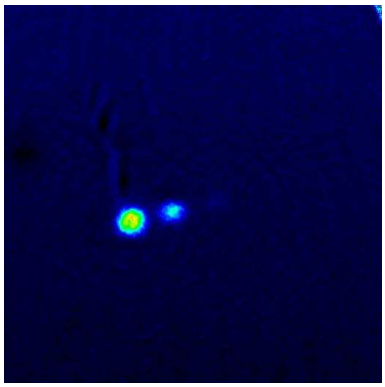

Figure 3.10: This picture shows the populations in the bare m_F states P_1 and P_2 after a sudden switch off of rf and keeping the atoms in the gradient of the Ioffe coil for 2 ms. This is an absorption picture taken after 5 ms of time of flight

now that the spectroscopic method is more appropriate to measure correctly the Rabi frequency of the rf dressing field.

Part of the work presented in this chapter was already done by the previous Ph.D students Y. Colombe and O. Morizot. In his dissertation, O. Morizot explains the difficulties in transferring the atoms from the static magnetic trap to a dressed rf trap. The main difficulty was the heating originated from excitations along the transverse axis, either due to frequency noise of the synthesizer used in FM mode or to discrete frequency steps when using a DDS synthesizer. Even after transfer, the life time in the rf dressed trap (9.6 s at best) was much less than the one in the static magnetic trap (about 60 s). This was the motivation for an intense study on the influence of various rf sources on the ultracold atoms to understand and avoid the technical noise coming from the rf components. This work is explained in the next chapter of this manuscript.

Chapter 4

Influence of the radio-frequency source properties on rf-based atom traps

This chapter is essentially based on our publication [36]. However, some notations were modified, so that it will be consistent with the rest of the chapters. As discussed in the conclusion of previous chapter, we decided to do a systematic study on the quality required for the rf source used to trap neutral atoms in rf-dressed potentials. For rf-based trapping, the requirements on the technical noise coming from the rf components is stronger than in the case of evaporative cooling of an atomic sample. In the case of evaporative cooling atoms are located away from the region of efficient coupling, whereas in the rf-based trapping scheme the coldest atoms sit exactly at the point where the rf field has the largest effect. The quality of the rf source is then much more important in the latter case. Indeed, the cloud position is directly related to the value of the rf field frequency, whereas the trap restoring force, or equivalently the oscillation frequency ν_z in the harmonic approximation, is linked to the rf amplitude. As a result, any amplitude noise, frequency noise or phase noise of the rf signal during the ramp or the plateau leads to heating of the cold atomic cloud [22]. These considerations motivated the detailed study done with different rf sources presented in this chapter. The chapter is organized as follows: In sections 4.1.1 and 4.1.2, I give explicit expressions for the heating of the cold atom sample for frequency or amplitude noise in the case of rf-based trapping. Section 4.2 is devoted to experimental results, with a comparison between different rf sources tested on our Bose-Einstein condensate experiment.

4.1 Requirements on the rf source for rf-based trapping

The quality of the rf source is very important in the rf based traps. Indeed, the cloud position is directly related to the value of the rf field frequency, whereas the trap

restoring force, or equivalently the oscillation frequency in the harmonic approximation, is linked to the rf amplitude. As a result, any amplitude noise, frequency noise or phase noise of the rf signal during the ramp or the plateau leads to heating of the cold atomic cloud. The atomic motion is pendulum-like in the horizontal directions, and imposed by the rf interaction along the vertical z axis. This last direction is thus the most sensitive to the rf field properties (frequency ν_1, amplitude B_{01} or Ω_1 in units of frequency) and we will therefore concentrate on the vertical motion in the following. Along this direction, heating or atomic losses may arise from frequency or amplitude noise, phase jumps or discrete frequency steps during the rf ramp.

4.1.1 Frequency noise: dipolar excitation heating

Fluctuations of the rf field amplitude Ω_1 are responsible for parametric heating in the vertical direction. Very generally, for atoms in a one dimensional harmonic trap with a trapping frequency $\nu_\perp$, any effect producing a jitter in the trap position z results in linear heating through dipolar excitation. The average energy of the cold atomic cloud E increases linearly as [37]:

$$\dot{E} = \frac{1}{4} M \omega_\perp^4 S_z(\nu_\perp) \tag{4.1}$$

where $\omega_\perp = 2\pi\nu_\perp$, M is the atomic mass and S_z is the one-sided Power Spectral Density (PSD) of the position fluctuations δz, defined as the Fourier transform of the position correlation function [37]

$$S_z(\nu) = 4 \int_0^\infty d\tau \, \cos(2\pi\nu\tau) \langle \delta z(t) \, \delta z(t+\tau) \rangle. \tag{4.2}$$

In our 3D trap, the time variations of energy, E, and temperature T, are related by $T = \frac{E}{3k_B}$. In principle, E is the sum of three contributions of the type (4.1) for all three directions. However, due to the difference in the oscillation frequencies, the vertical heating is always much larger than the horizontal ones in this rf-based trap, and we will neglect the minor contributions in the following. The vertical trap position z is a function $z = Z(\nu_1)$ of the rf frequency $\nu_1 = \frac{\omega_1}{2\pi}$. As a result, S_z is directly proportional to S_{rel}, the PSD of relative frequency noise of the rf source:

$$S_z(\nu) = \left(\nu_1 \frac{dZ}{d\nu_1} \right)^2 S_{\mathrm{rel}}(\nu). \tag{4.3}$$

The function Z depends on the geometry of the static magnetic field. In a quadrupolar field, for instance, Z is linear with ν_1 and its derivative is a constant. From equations (4.1) and (4.3), we infer that the linear heating rate is proportional to $S_{\mathrm{rel}}(\nu_\perp)$. To fix orders of magnitude, within the static magnetic field of our Ioffe-Pritchard trap, $\nu_\perp$ may be adjusted between 600 and 1500 Hz and the typical temperature of the cold rubidium 87 atoms ranges from 0.5 to 5 µK. For Bose-Einstein condensation experiments, a linear temperature increase below $0.1\,\mu\mathrm{K}\cdot\mathrm{s}^{-1}$ is desirable. This rate corresponds to $\sqrt{S_z(\nu_\perp)} = 0.3\,\mathrm{nm}\cdot\mathrm{Hz}^{-1/2}$ for an intermediate trap frequency of 1000 Hz and $\omega_1 = 2\pi \times$ 3 MHz, which in turn corresponds to a one-sided PSD of relative frequency fluctuations of the rf source $S_{\mathrm{rel}}(\nu_\perp) = 118\,\mathrm{dB}\cdot\mathrm{Hz}^{-1}$.

4.1.2 Amplitude noise: parametric heating

Fluctuations of the rf field amplitude Ω_1 are responsible for parametric heating in the vertical direction. As already stated at Eq.(3.20), the trapping frequency $\nu_\perp = \omega_\perp/(2\pi)$ is inversely proportional to $\sqrt{\Omega_1}$ [21]:

$$\nu_\perp = \left(\frac{dZ}{d\nu_1}\right)^{-1} \sqrt{\frac{F\hbar}{M\Omega_1}}. \tag{4.4}$$

Here, F is the total atomic spin ($F = 2$ for rubidium 87 in its upper hyperfine state). The atoms are assumed to be polarized in their extreme $m_F = F$ substate. Amplitude noise then results in an exponential increase of the cloud temperature with a rate Γ given by

$$\Gamma = \pi^2 \nu_\perp^2 S_a(2\nu_\perp) \tag{4.5}$$

where S_a is the PSD of the relative rf amplitude noise [37]. In order to perform experiments with the BEC within a time scale of a few seconds, Γ should not exceed $10^{-2}\,\mathrm{s}^{-1}$ [38]. Again, for a typical oscillation frequency of 1000 Hz, this corresponds to $S_a < -90\,\mathrm{dB}\cdot\mathrm{Hz}^{-1}$. This requirement is rather easy to match and does not limit the choice of the rf source, as -110 $\mathrm{dB}\cdot\mathrm{Hz}^{-1}$ is commonly reached with commercial synthesizers. However, particular care must be taken in the choice and installation of the rf amplifier usually used after the source.

4.1.3 Phase jumps

Controlling the phase of the rf source is not a crucial point for evaporative cooling, but becomes an issue in the case of rf-based traps, where it is associated with trap losses. In the latter situation, the atomic spin is an eigenstate of F_θ, see section 3.1. It follows an effective magnetic field precessing at the rf frequency around the dc magnetic field, with a precession angle $2\pi\nu_1 t$ and a nutation angle θ. A phase jump results in a sudden change $\Delta\varphi$ in the precession angle, the atomic spin being then misaligned with the new direction the effective field. Some of the atoms end up with a spin oriented incorrectly and escape the trap.

The atomic loss after a phase jump $\Delta\varphi$ may be estimated in the following way. As seen in chapter 3, Eq.(3.10), the nutation angle $\theta(\mathbf{r})$ is linked to rf frequency and amplitude through $\tan(\theta) = \Omega_1/(\omega_0(\mathbf{r}) - 2\pi\nu_1)$. $\theta(\mathbf{r})$ is position dependent, as is the value of the dc magnetic field. After the phase jump, the new effective field makes an angle ψ with the former one, where $\sin(\psi/2) = \sin(\theta)\sin(\Delta\varphi/2)$. At a given position, the probability $p(\psi)$ of keeping an atom in the new dressed state is then given by its overlap with the initial spin eigenstate, $p(\psi) = [\cos(\psi/2)]^{4F}$. In the case of rubidium 87 in the $F = 2$ hyperfine ground state, starting polarized in the $m_F = 2$ dressed state, $p(\psi) = \cos^8(\psi/2)$. The fraction $P(\Delta\varphi)$ of the atoms remaining in the right state is then an average of $\langle p(\psi)\rangle_\theta$ over the cloud size. For example, a phase jump of 10^{-2} rad will result at most in a loss of a fraction 10^{-4} of the atoms in states other than $m_F = 2$.

For a single phase jump, as illustrated experimentally in section 4.2, the phase jump amplitude should then remain below 0.1 rad for limiting the losses to 1%. However,

even much smaller phase jumps should be avoided, if they are repeated. This is difficult to achieve with an analog synthesizer over a wide frequency sweep. By contrast, Direct Digital Synthesis (DDS) technology is well adapted to this requirement.

4.1.4 Frequency steps

The drawback of DDS technology is that, although the phase is continuous, the frequency is increased in successive discrete steps $\delta\nu$. A sudden change in the rf frequency also results in atomic losses, through the same mechanism as for phase jumps. The effective magnetic field rotates, at most, by the small angle $\delta\theta$ given by $\delta\theta = 2\pi\,\delta\nu/\Omega_1$. For a linear ramp with N steps over a frequency range $\Delta\nu = N\delta\nu$, the fraction of atoms remaining after the full ramp is of order $[\cos(\delta\theta/2)]^{4FN}$. Given the expression for $\delta\theta$, this reads:

$$\left[\cos\left(\frac{\pi\,\Delta\nu}{N\Omega_1}\right)\right]^{4FN} \simeq 1 - \frac{F}{2N}\left(\frac{2\pi\,\Delta\nu}{\Omega_1}\right)^2 . \tag{4.6}$$

Thus, for the remaining fraction to be larger than 95%, the number of frequency steps should be larger than $N_{\min}$, where $N_{\min} = 10F(2\pi\,\Delta\nu/\Omega_1)^2$. For example, for a 2 MHz ramp with a typical rf amplitude of 70 kHz, it yields $N_{\min}$ =16,000.

In addition to this loss effect, a sudden change in the rf frequency results in a sudden shift of the position of the rf-dressed trap. This may cause dipolar heating of the atoms, especially if this frequency change occurs every trap period. The frequency steps should thus be as small as possible, a few tens Hz to a hundred Hz typically.

4.2 Results

In the following, we present three kinds of measurements performed with different rf sources. First, we investigate the effect of a single phase jump at the end of the ramp on the trapped atom number, for a fixed holding time. Second, the number of frequency steps during the ramp is varied and the final number of atoms is recorded together with the temperature. Finally, the holding time is varied to measure the lifetime and the heating rate in the rf-based trap, for three different rf-sources. The atom number and the temperature are measured after a ballistic expansion of 10 ms by absorption imaging on a CCD camera. The temperature is deduced from the vertical size of the cloud after expansion, as the initial size in the trap is smaller along z.

4.2.1 Phase jumps

The effect of a phase jump is tested in the following way. The rf frequency is swept from 1 MHz to 3 MHz with the Stanford DS-345 DDS presented in section 2.6.1. The 1,500 points frequency ramp is non linear, with a slower zone around the resonance crossing at 1.3 MHz in the spirit of the typical ramp depicted on Fig. 4.2. The rf antenna is then switched to a second independent synthesizer, the Rohde & Schwartz SML-01 described in section 2.6.1, maintained at a fixed frequency of 3 MHz for the

full holding time (dashed line of Fig. 4.2). The phase difference is not controlled at the switching, but is monitored for each experiment with an oscilloscope. The final atom number is recorded after a 1 s holding time. The results are presented on Fig. 4.1, full circles. For the maximum phase jump, π, 80% of the atoms are lost. This figure depends on the atomic temperature, the losses being higher at lower temperature, and is well reproduced by theory, as shown on Fig. 4.1, black line. The theoretical curve is calculated for the experimental rf amplitude of 165 kHz by averaging the loss probability over the positions of the atoms, as deduced from a thermal distribution at the measured temperature of 4 µK. The fact that the trap is able to hold two of the five spin components of the $F = 2$ hyperfine state is taken into account, by using $p(\psi) = \cos^8(\psi/2) + 4\cos^6(\psi/2)\sin^2(\psi/2)$, see section 4.1.3 for the definition of the probability $p(\psi)$. The overall amplitude is set to the initial atom number in the magnetic trap before transfer into the rf-based trap, measured independently. We find a very good agreement between the experimental results and the simple theory developed above, with no adjustable parameter.

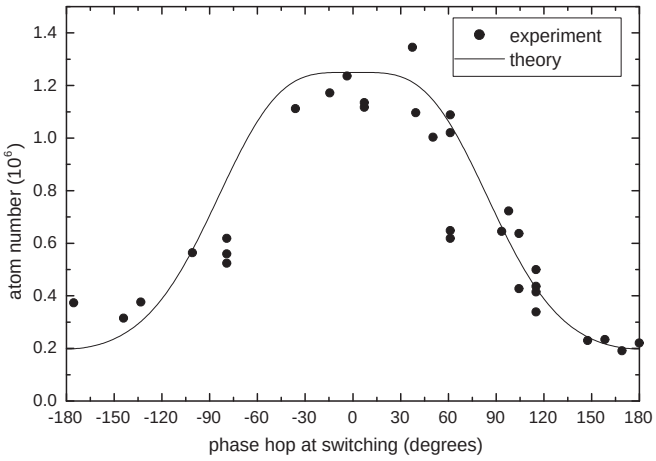

Figure 4.1: Number of atoms remaining 1 s after switching between the two synthesizers as a function of the phase jump. Experimental data, full circles, are compared to a calculation, full line, with an rf amplitude of 165 kHz and a temperature of 4 µK.

4.2.2 Frequency steps

As discussed in section 4.1.4, the transfer efficiency is expected to depend on the number of frequency steps in the ramp, when a DDS device is used. To evaluate the number of required steps, we repeated the following procedure, varying only the number of frequency points in the arbitrary ramp. The atoms were cooled in the magnetic trap down to 10 µK. After an adiabatic switching of the rf up to $\Omega_1 = 2\pi \times 200$ kHz in 12 ms, the rf frequency was ramped from 1 MHz to 8 MHz in 88 ms to transfer the atoms in the

rf-based trap. The number of transferred atoms and their temperature was recorded after 1 s in the trap. This time was short as compared to the lifetime in the rf-based trap, which reached 25 s for this experiment. The arbitrary ramp is depicted on Fig. 4.2. It consisted in a constant plateau of 12 ms followed by two connected cosine branches of 10 ms and 78 ms respectively, in order to cross the resonance at 1.25 MHz more slowly. For these experiments, the sine-wave output of the Tabor Electronics DDS synthesizer presented in section2.6.1 was used. The number of frequency points N was varied between 500 and 20,000 which is the maximum value for this device. These frequency lists were constructed by removing uniformly a fraction of the points of a reference arbitrary ramp of 20,000 points. Only 88% of these points really contributed to the frequency ramp, as 12% of them were used for maintaining a constant frequency for the initial switching stage.

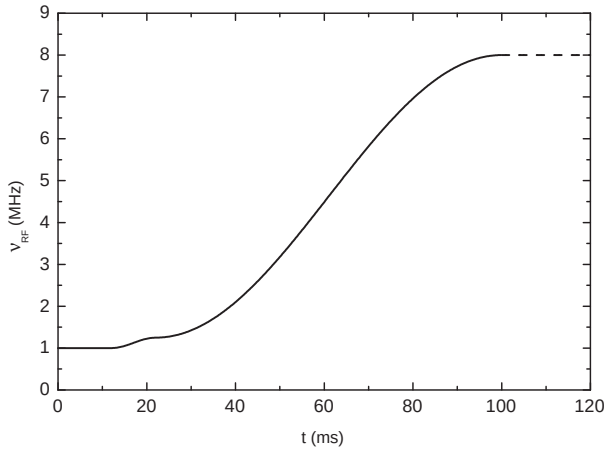

Figure 4.2: Typical shape of a radio-frequency ramp applied to the ultracold atomic sample. In the present example ν_{rf} is increased from 1 to 8 MHz within 88 ms, after a 12 ms stage where the frequency is maintained at 1 MHz for adiabatic switching of the rf source. At the end of the ramp, the rf frequency is maintained at its final value for some holding time in the rf-based trap, dashed line.

The results for atom number and temperature are presented on Fig. 4.3 and 4.4 respectively. The initial atom number in the magnetic trap was measured to be $2.05 \pm 0.2 \times 10^6$. Two regimes are clearly identified. Below N =5,000, the number of transferred atoms increases almost linearly with N. Above this value, more than 80% of the atoms are transferred into the rf-based trap, and the number of atoms detected for N larger than 15,000 is even equal to the initial atom number. To compare with the theory of section 4.1.4, the expected value of the transferred number given by both the measured initial atom number and Eq.(4.6) is plotted together with the data, dashed line. The number of frequency steps considered in the calculation is $0.88N$, as the initial points at constant frequency do not induce losses. The theory reproduces well the overall behaviour, even if it slightly underestimates the transfer efficiency at

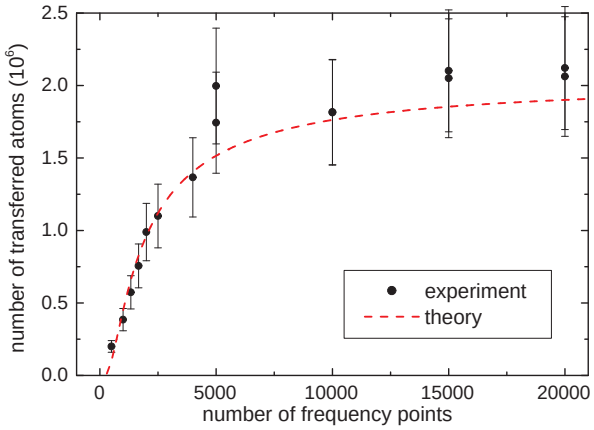

Figure 4.3: Number of atoms remaining 1 s after the transfer ramp, as a function of the number of frequency points in the arbitrary ramp. Circles: experimental data. Dashed line: prediction of the model of Eq.(4.6).

large N. In particular, it predicts a transfer efficiency reaching 80% for N =7,000. The transfer efficiency is expected to reach 93% for N =20,000, which is consistent with the experiment within the uncertainty.

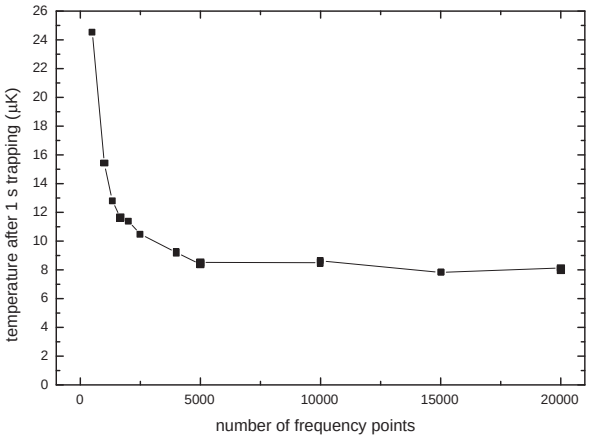

Figure 4.4: Temperature of the transferred atoms, measured 1 s after the end of the transfer ramp, as a function of the number of frequency points in the arbitrary ramp. The initial temperature in the magnetic trap was 10 μK. The solid line is a guide to the eye.

Below 5,000 points, the lack of frequency resolution in the ramp is also visible in the temperature data, Fig. 4.4, as a clear temperature increase during the loading phase. This is due to the excitation of the dipolar mode through sudden changes in the trap position at each frequency change, as explained in section 4.1.4. For more than 5,000 frequency points, the temperature reaches the asymptotic value of 8 μK. This value is smaller than the initial temperature in the magnetic trap. This was expected as the geometric mean of the oscillation frequencies is much larger in the initial trap. The transfer within 88 ms is not adiabatic in this respect, the expected temperature in the rf-based trap being on the order of 2 μK for an adiabatic transfer.

4.2.3 Frequency noise

The heating rate in the dressed trap was measured with three different rf sources. First, we used an Agilent 33250A analog synthesizer with an rf amplitude of 180 kHz for both the frequency ramp and the final holding frequency. Such rf analog synthesizers operated at fixed frequency exhibit very good relative frequency noise in most cases, typically at the $-180\,\mathrm{dB}\cdot\mathrm{Hz}^{-1}$ level or better. However, as mentioned by Y. Colombe *et al.* [22] and confirmed by White *et al.* [39], the relative frequency noise increases by a few decades when a large range frequency sweep is required, as the output frequency then needs to be driven with an external analog voltage. The external voltage control was provided by a PC analog board (NI 6713), such that the modulation depth was ±1 MHz on a central frequency of 2 MHz. We obtained both a short lifetime, typically 400 ms at $1/e$, and a strong linear heating, as shown on Fig. 4.5 full circles. The heating rate is measured to be $5.0\,\mu\mathrm{K}\cdot\mathrm{s}^{-1}$. This rate, given the rf amplitude, corresponds to a relative frequency noise of $S_{\mathrm{rel}} = -100\,\mathrm{dB}\cdot\mathrm{Hz}^{-1}$ at the trap frequency of 600 Hz. An independent measurement of the spectral width of the rf signal produced by the Agilent synthesizer in the same conditions indeed gave the same value for the relative frequency noise $S_{\mathrm{rel}} = -100\,\mathrm{dB}\cdot\mathrm{Hz}^{-1}$. This noise is quite high because the frequency is varied with a large modulation depth ($\Delta f/f = 1$) and the voltage noise of the NI board is directly translated into frequency noise.

We also measured the lifetime and heating rate with the setup used for phase jump characterisation, with the disadvantage however that the random phase jumps resulted in a large dispersion in the atom number data. Nevertheless, within a precision limited to $0.1\,\mu\mathrm{K}\cdot\mathrm{s}^{-1}$ and 2 s respectively, we observed no heating and a lifetime of order 4.5 s [22]. These good results are linked to the excellent frequency stability of the second device used at fixed frequency.

Finally, the lifetime and heating measurement was repeated with the Tabor Electronics WW1072 device mentioned previously. The loading ramp was the same as described above, with 20,000 frequency points between 1 and 8 MHz, but with a total duration of 500 ms. Typical results are presented on Fig. 4.5, open diamonds. The contrast with the Agilent data is very strong. With the Tabor device and an rf amplitude of 200 kHz, the lifetime increased up to 32 s, a value comparable with the lifetime in the static magnetic trap. A small linear heating rate of $82 \pm 5\,\mathrm{nK}\cdot\mathrm{s}^{-1}$ is still present in the rf-based trap for this data set. No exponential parametric heating is measurable. The residual heating rate is slightly larger than the one predicted from the Tabor device

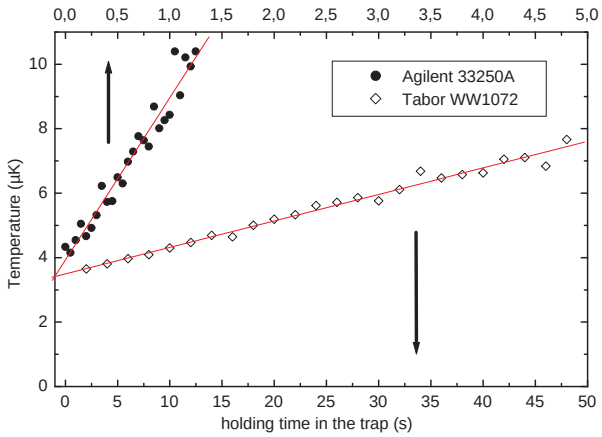

Figure 4.5: Comparison of heating of the atomic cloud in the bubble trap: Agilent 33250A synthesizer driven by NI board, full circles, or Tabor Electronics WW1072, open diamonds, is used for producing the rf ramp and the final radio-frequency ν_1^{end}. Note that the horizontal scales differ by a factor 10 for the two data sets. We observe a heating rate of $5.0\,\mu\mathrm{K}\cdot\mathrm{s}^{-1}$ in the first case and $0.082\,\mu\mathrm{K}\cdot\mathrm{s}^{-1}$ the second one, as given by a linear fit, full lines. The lifetime reaches 32 s in this situation.

specifications. At 8 MHz and for an oscillation frequency of 600 Hz, we expect a linear heating rate of $17\,\mathrm{nK}\cdot\mathrm{s}^{-1}$. This value is slightly smaller than $33\,\mathrm{nK}\cdot\mathrm{s}^{-1}$, which is the lowest observed heating rate with the Tabor device. For the calculation of the theoretical rate, $\nu_\perp$ was deduced from the oscillation frequency measurement, see section 3.6.1. If the real oscillation frequency is larger by only 20%, as it is possible due to the non harmonic shape of the potential, it could explain the discrepancy.

4.3 Conclusion

The requirements on the radiofrequency source may be divided into two parts, concerning the ramping stage and the holding stage. Once the atoms are loaded in the rf-based trap, heating and trap losses are avoided if the relative frequency noise and the amplitude noise are below $S_{\mathrm{rel}}(\nu_\perp) = -118\,\mathrm{dB}\cdot\mathrm{Hz}^{-1}$ and $S_a < -90\,\mathrm{dB}\cdot\mathrm{Hz}^{-1}$ respectively. This is relatively easy to meet, although care has to be taken on the choice of low noise rf attenuators and amplifiers. The best results were obtained with the Tabor Electronics device, with a typical heating rate of $0.082\,\mu\mathrm{K}\cdot\mathrm{s}^{-1}$ and a lifetime of up to 32 s. Finally, the lifetime would be affected if the rf amplitude is below a few tens of kHz, as Landau-Zener losses then occur at the avoided crossing [40].

For the initial frequency sweep, the use of DDS technology ensures phase continuity, and losses or heating are limited if the number of frequency points is large enough, say, 10,000 at least for a few MHz ramp. In the loading stage, once the number of frequency steps is sufficient, the heating will mostly be given by the non adiabatic deformation of the trapping potential when the atoms are transferred from the magnetic to the dressed trap. But as the value of the lowest oscillation frequency in the dressed trap

is of the order of a few Hz, this heating is difficult to avoid. This prevented us from transferring directly the Bose-Einstein condensate to the rf dressed trap. On the other hand, cooling directly in the rf-based trap [23,41] is made possible by the long lifetimes and the low heating rates reported here. We present an implementation of this strategy in chapter 5 of this manuscript. In any case, these good performances make the rf-based trap compatible with the confinement of Bose-Einstein condensates.

Chapter 5

Spectroscopy and evaporative cooling in a rf-dressed trap

After trying to load the dressed trap with a BEC, we decided to go in another direction: we first dress the atoms from a cold sample and then evaporate them. This technique has been studied theoretically in our group [23] and shows that a weak additional rf field can outcouple the dressed atoms at a given position in the adiabatic potential. In order to understand well the evaporative cooling mechanism in the rf dressed trap we performed here some spectroscopic measurements. They will give us an idea of the different transitions involved when we irradiate a weak additional rf probe field close to the rf dressed state level spacing. When the probe rf field is resonant with the dressed state level spacing, transitions to an untrapped state are induced. This results in trap losses, which are the signature of the resonances. Unlike for the case of a static magnetic trap, not only one but multiple resonance frequencies are identified. Two resonances were already discussed in [23] using a semi-classical approach, and the third one is presented in section 5.1.5. Once these transitions have been identified, we used them to evaporate the hotter atoms in the dressed trap, by applying a sweep of an additional weak rf field close to the observed transitions. We found that the evaporation is efficient for one of the transitions, inducing a temperature decrease and an increase in the phase space density. In the following sections, I will give a theoretical background for the predicted resonances and I will present the experimental procedure and results.

5.1 Theory

5.1.1 Hamiltonian for the rf spectroscopy

The underlying idea of confining ultra cold atoms using rf adiabatic potentials is presented in detail in chapter 3 of this manuscript. Here, we will follow the approach of Ref. [23]. Using the dressed trap Hamiltonian for the first rf field, we will derive a

time independent Hamiltonian in the presence of the second rf field. This will explain the transitions occurring, when the frequency of second rf field ω_2 differs from the dressing frequency ω_1 by the frequency difference between the adiabatic eigenenergies $\Omega(\mathbf{r})$. Other transitions occur at a frequency ω_2 equal to this level spacing and will be described in section 5.1.5. More generally, beyond the rotating wave approximation (RWA), the number of allowed transitions increases, with resonant frequencies of the form $\omega_2 = n\omega_1 \pm \Omega(\mathbf{r})$, n being an integer [35].

The Hamiltonian of the atom-spin interaction $H_T(\mathbf{r},t)$ for the atoms trapped in a static magnetic field $\mathbf{B}_{dc}(\mathbf{r})$, together with a rf oscillating magnetic field $B_1(\mathbf{r},t)$ was given in Eq.(3.1). We now add a second rf field $B_2(\mathbf{r},t)$, which is sent to probe the resonances. The probe rf field $B_2(\mathbf{r},t)$ is polarized along the same direction as $B_1(\mathbf{r},t)$, here the $X \equiv y$ direction. The new Hamiltonian contains an extra term for the second rf and Eq.(3.1) can be modified as:

$$\begin{aligned} H_T(\mathbf{r},t) &= \frac{g_F\mu_B}{\hbar}\mathbf{F}.[\mathbf{B}_{dc}(\mathbf{r}) + \mathbf{B}_1(\mathbf{r},t) + \mathbf{B}_2(\mathbf{r},t)] && (5.1)\\ &= \omega_0(\mathbf{r})F_Z + V_1(\mathbf{r},t) + V_2(\mathbf{r},t) && (5.2)\end{aligned}$$

where $\mathbf{B}_1(\mathbf{r},t) = B_{01}\hat{\mathbf{e}}_X\cos(\omega_1 t)$ and $\mathbf{B}_2(\mathbf{r},t) = B_{02}\hat{\mathbf{e}}_X\cos(\omega_2 t)$. B_{01} and B_{02} are the rf amplitudes of rf fields at ω_1 and ω_2, respectively. We assume that the rf field is uniform to the spatial extent of the atoms, which is experimentally the case.

Each coupling term $V_j(t)$ is given by the expression:

$$V_j(t) = \Omega_j F_X(e^{i\omega_j t} + e^{-i\omega_j t}), \quad j = 1,2 \tag{5.3}$$

where $\Omega_j = g_F\mu_B B_{0j}/(2\hbar)$ is the Rabi frequency of the rf field of frequency ω_j.

Given $H_T(\mathbf{r},t)$, the dynamics of an atomic spin state $|\phi(\mathbf{r},t)\rangle$ is governed by the Schrödinger equation:

$$i\hbar\frac{\partial}{\partial t}|\phi(\mathbf{r},t)\rangle = H_T(\mathbf{r},t)\,|\phi(\mathbf{r},t)\rangle \tag{5.4}$$

which in the frame rotating at the frequency ω_1, becomes:

$$ih\frac{\partial}{\partial t}|\psi(\mathbf{r},t)\rangle = [-\delta(\mathbf{r})F_Z + R_1^\dagger V_1(t)R_1 + R_1^\dagger V_2(t)R_1]\,|\psi(\mathbf{r},t)\rangle \tag{5.5}$$

where $\delta(\mathbf{r}) = \omega_1 - \omega_0(\mathbf{r})$ and $\omega_0(\mathbf{r}) = g_F\mu_B B_{dc}(\mathbf{r})/\hbar$.

The term $-\delta(\mathbf{r})F_Z + R_1^\dagger V_1(t)R_1$ was already discussed in chapter 3. It gives rise to the first RWA adiabatic Hamiltonian $H_A(\mathbf{r})$ as given in Eq.(3.8). The second rf interaction term $R_1^\dagger V_2(t)R_1$ is given by:

$$\begin{aligned} R_1^\dagger V_2(t)R_1 &= 2\Omega_2\cos(\omega_2 t)(\cos(\omega_1 t)F_X - \sin(\omega_1 t)F_Y) && (5.6)\\ &= \Omega_2\left[\cos(\omega_1+\omega_2)t + \cos(\omega_1-\omega_2)t\right]F_X - \Omega_2\left[\sin(\omega_1-\omega_2)t + \sin(\omega_1+\omega_2)t\right]F_Y.\end{aligned}$$

Let us consider the situation where the frequency ω_2 is close to ω_1 and ω_1 is fast as compared to the Bloch vectors dynamics. This condition can be written as $|\omega_1 - \omega_2| \ll \omega_1$ and $\omega_1 \gg \Omega_2, \delta, \Omega_1$. We can then apply the first rotating wave approximation to Eq.(5.6) by neglecting the fast oscillating terms at the frequency $\omega_1 + \omega_2$, and get:

$$H(\mathbf{r},t) = H_A(\mathbf{r}) + \Omega_2[\cos(\Delta t)F_X + \sin(\Delta t)F_Y] \tag{5.7}$$

where $\Delta = \omega_2 - \omega_1$ and $H_A(\mathbf{r}) = \Omega(\mathbf{r})F_\theta$ (see Eq.(3.10) and Figure 3.2).

5.1.2 Second rotating wave approximation

The Hamiltonian $H(\mathbf{r},t)$ we derived in the Eq.(5.7) contains time dependent terms. In order to make it time independent, we introduce a rotation at frequency $|\Delta|$ around F_θ and will apply a second rotating wave approximation. The Hamiltonian in the Eq.(5.7) can be expressed through the rotation $H'(t) = R_\Delta H(t) R_\Delta^\dagger$, where $R_\Delta = \exp(i|\Delta|tF_\theta/\hbar)$. This transformation leads to the time-dependent Hamiltonian:

$$\begin{aligned} H'(t) &= -(|\Delta| - \Omega(\mathbf{r}) - \Omega_2 \sin\theta\cos\Delta t)F_\theta \\ &+ \Omega_2(\cos\theta\cos^2\Delta t + \varepsilon\sin^2\Delta t)F_{\perp\theta} + \Omega_2(1-\varepsilon\cos\theta)\sin\Delta t\cos\Delta t F_Y \end{aligned} \tag{5.8}$$

where $F_{\perp\theta} = \mathbf{F}.\mathbf{e}_{\perp\theta}$ is the projection of the atomic angular momentum in the direction perpendicular to both $\mathbf{e}_\theta$ and $\mathbf{e}_Y$, and ε is the sign of Δ such that $\Delta = \varepsilon|\Delta|$.

Now we apply a second rotating wave approximation, by averaging to zero the terms oscillating at the frequency 2Δ and the oscillating term along F_θ. This is valid provided that $||\Delta| - \Omega(\mathbf{r})| \ll |\Delta|$ and $\Omega_2 \ll |\Delta|$. We finally obtain from Eq.(5.8) the time-independent effective Hamiltonian:

$$H'_A(\mathbf{r}) = -(|\Delta| - \Omega(\mathbf{r}))F_\theta + \frac{\Omega_2}{2}(1+\varepsilon\cos\theta(\mathbf{r}))F_{\perp\theta} = \Omega_\Delta(\mathbf{r})F_{\theta_\Delta}, \tag{5.9}$$

where

$$\Omega_\Delta(\mathbf{r}) = \sqrt{(|\Delta| - \Omega(\mathbf{r}))^2 + \frac{\Omega_2^2}{4}(1+\varepsilon\cos\theta(\mathbf{r}))^2} \tag{5.10}$$

and

$$F_{\theta_\Delta} = \cos(\theta_\Delta)F_\theta + \sin(\theta_\Delta)F_{\perp\theta} \tag{5.11}$$

with $\tan(\theta_\Delta) = -\dfrac{\Omega_2[1+\varepsilon\cos\theta(\mathbf{r})]}{2(|\Delta| - \Omega)}$ for $\theta_\Delta \in [0,\pi]$.

The Hamiltonian in the Eq.(5.9) is equivalent to Eq.(3.10) with a coupling $\Omega_\Delta(\mathbf{r})$ dependent explicitly on the position via $\theta(\mathbf{r})$ and $\Omega(\mathbf{r})$. Its eigenstates $|m''_F\rangle_\theta$ are doubly dressed states, making an angle θ_Δ with the singly dressed eigenstates $|m'_F\rangle_\theta$. The vectorial representation of the spin in the presence of the second rf field is shown in Figure 5.1. The spin of the atoms confined in the adiabatic potential is aligned along F_θ. It is flipped along F_{θ_Δ} in the presence of the second rf field, in a basis rotating around F_θ at frequency $|\Delta|$.

The energy of the doubly dressed trap can be written after diagonalizing the Hamiltonian of Eq.(5.9) as $E_\Delta = m''_F\hbar\Omega_\Delta(\mathbf{r})$. $\Omega_\Delta(\mathbf{r})$ describes the energy seperation between the doubly dressed states. The adiabatic potential for the doubly dressed states $|2''\rangle \equiv |m''_F = 2\rangle$ and $|-2''\rangle$ are plotted as a function of the position z in the absence (neglecting) of gravity in Figure 5.2. It is clear from this figure that the effect of the second rf field is to truncate the adiabatic potential to a depth depending on the frequency difference Δ. Note that the singly dressed state $|2'\rangle$ in which the atoms are confined initially is matched to the doubly dressed state $|-2''\rangle$ — not to $|2''\rangle$.

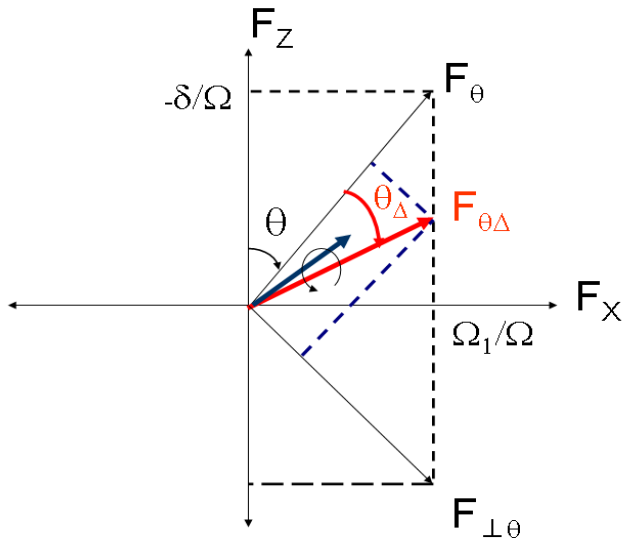

Figure 5.1: In the presence of the second rf field and after applying a second RWA, the spin (red arrow) precesses around an axis obtained when first, ω_1 tilts F_Z by θ getting F_θ and then ω_2 tilts F_θ by θ_Δ getting $F_{\theta\Delta}$.

5.1.3 Resonant coupling for the rf probe

As soon as $|\Delta|$ is larger than the minimum frequency spacing Ω_1 between singly dressed states, there will be points in space where the resonance condition $\Omega(\mathbf{r}) = |\Delta|$ is fulfilled. As a matter of fact, there are two positions $\mathbf{r}_i (i = 1, 2)$ such that $\Omega(\mathbf{r}_i) = |\Delta|$. These positions correspond to a dressing angle $\theta(\mathbf{r}_1) = \theta_0$ and $\theta(\mathbf{r}_2) = \pi - \theta_0$ with $\theta_0 = \arcsin \frac{\Omega_1}{|\Delta|}$. These two positions, called the *inner resonance* (IR) inside the trapping surface and the *outer resonance* (OR) outside, are symmetrical with respect to the center of the dressed trap, located on the iso-B surface $\omega_0(\mathbf{r}) = \omega_1$. The effective coupling of the second rf to the dressed spin is different at these two locations, and is given by $\frac{\Omega_2}{2}[1 + \varepsilon \cos\theta_0]$ and $\frac{\Omega_2}{2}[1 - \varepsilon \cos\theta_0]$, respectively. At the bottom of the trap $\theta = \frac{\pi}{2}$, the two resonances collapse into a single one, with an energy seperation Ω_2. All the three points θ_0, $\theta = \pi/2$ and $\pi - \theta_0$ are shown in Figure 5.2. Hence, the hotter atoms are outcoupled through these two locations OR and IR for a fixed value of $|\Delta|$, which sets the trap depth.

5.1.4 Trap depth

As already pointed out, the atoms are trapped in the state $|2''\rangle$ of the doubly dressed trap. The trap depth ΔE can then be written as the energy difference in this state between the resonance with the strongest coupling (for which the depth is smallest, see

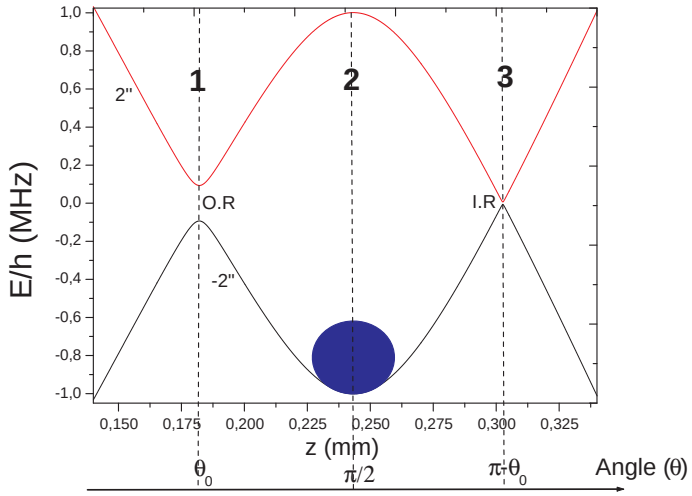

Figure 5.2: Adiabatic potential of the doubly dressed state $|2''\rangle$ in the absence of gravity. The position 1, 2 and 3 corresponds to the different values of θ. The blue spot indicates the atomic cloud sitting in the $m''_F = -2$ doubly dressed state.

Figure 5.2) and the trap bottom $\theta = \frac{\pi}{2}$:

$$\Delta E = m_F \hbar \left(\Omega_\Delta(\text{res}) - \Omega_\Delta(\theta = \frac{\pi}{2}) \right). \tag{5.12}$$

In our case $m_F = -2$, and using $\cos\theta_0 = \sqrt{\Delta^2 - \Omega_1^2}/|\Delta|$, we get:

$$\Delta E = -2\hbar \left[\frac{\Omega_2}{2} \left(1 + \frac{\sqrt{\Delta^2 - \Omega_1^2}}{|\Delta|} \right) - \sqrt{(|\Delta| - \Omega_1)^2 + \frac{\Omega_2^2}{4}} \right]. \tag{5.13}$$

The trap depth goes to zero when the second rf is resonant with the level spacing at the trap bottom, *i.e.* at $|\Delta| \approx \Omega_1$ [1]. We expect resonances that fully empty the dressed trap at these locations, corresponding to $\omega_2 = \omega_1 + \Omega_1$ and $\omega_2 = \omega_1 - \Omega_1$. Thus for two values of the probe frequencies all the atoms are resonantly coupled out of the trap.

5.1.5 The low frequency resonance

As mentioned in the introduction of this chapter, direct transitions between dressed states at a frequency of order $\omega_2 \sim \Omega_1$ can also occur. However, to described these transitions theoretically, we need to consider a π-polarized coupling, that is a second rf field polarized *along* the static magnetic field.

Let us consider the following Hamiltonian in the laboratory frame:

$$H(t) = \omega_0(\mathbf{r}) F_Z + 2\Omega_1 F_X \cos\omega_1 t + 2\Omega_2 F_Z \cos\omega_2 t. \tag{5.14}$$

[1] In reality, there is a small correction to this value. The first order correction gives $|\Delta| \approx \Omega_1[1 + (\frac{\Omega_2}{\Omega_1})^{\frac{4}{3}} \frac{1}{2^{\frac{1}{3}}}]$, with $\Omega_2 \ll \Omega_1$ as already stated for the RWA to be valid.

It is identical to Hamiltonian H_T of Eq.(5.1) except the polarization of the second rf field. Now, let us transform to the frame rotated by a time-dependent angle $\omega_1 t + \frac{2\Omega_2}{\omega_2}\sin\omega_2 t$, instead of $\omega_1 t$. The idea is that the time derivative of the rotated state will cancel the term $2\Omega_2 F_Z \cos\omega_2 t$ in the Hamiltonian H. The Hamiltonian H' applying to the rotated state reads:

$$\begin{aligned} H'(t) &= -\delta(\mathbf{r})F_Z + 2\Omega_1 \cos\omega_1 t \, \cos\left(\omega_1 t + \frac{2\Omega_2}{\omega_2}\sin\omega_2 t\right) F_X \\ &- 2\Omega_1 \cos\omega_1 t \, \sin\left(\omega_1 t + \frac{2\Omega_2}{\omega_2}\sin\omega_2 t\right) F_Y. \end{aligned} \tag{5.15}$$

As before, $\delta(\mathbf{r}) = \omega_1 - \omega_0(\mathbf{r})$. Here we will use the fact that $\Omega_2 \ll \omega_2$ and develop the sin and cos terms around $\omega_1 t$. Doing that and applying RWA to Hamiltonian (5.15) allows us to drop terms rotating essentially at $2\omega_1$. It yields:

$$H''(t) = -\delta(\mathbf{r})F_Z + \Omega_1 F_X - \Omega_1 \frac{2\Omega_2}{\omega_2}\sin\omega_2 t F_Y. \tag{5.16}$$

Using the usual notation $\Omega(\mathbf{r}) = \sqrt{\Omega_1^2 + \delta(\mathbf{r})^2}$ and the same F_θ and $F_{\theta\perp}$ spin operators, we have:

$$H''(t) = \Omega(\mathbf{r})F_\theta - \frac{2\Omega_1\Omega_2}{\omega_2}\sin\omega_2 t F_Y. \tag{5.17}$$

This describes the direct coupling of dressed states with a field of amplitude $2\Omega_1\Omega_2/\omega_2$ for a linear polarisation, that is with an effective coupling of $\Omega_1\Omega_2/\omega_2$. We can apply a rotation at frequency ω_2 around F_θ and again RWA, neglecting the terms oscillating at $2\omega_2$, which is valid if $|\omega_2 - \Omega(\mathbf{r})| \ll \omega_2$ and $\Omega_2 \ll \omega_2$ (already stated). One finally has for the doubly dressed Hamiltonian:

$$H_{dd} = (\Omega(\mathbf{r}) - \omega_2)F_\theta + \frac{\Omega_1\Omega_2}{\omega_2}F_{\theta\perp}. \tag{5.18}$$

The resonance at $\omega_2 = \Omega(\mathbf{r})$ appears naturally, as well as the coupling strength. The doubly dressed Hamiltonian gives a new direction for the eigenstates, which make an angle of θ_2 with F_θ, where $\tan\theta_2 = \frac{\Omega_1\Omega_2}{\omega_2(\Omega(\mathbf{r})-\omega_2)}$. Note that the coupling at resonance is even simpler, using $\omega_2 = \Omega(\mathbf{r}) = \Omega_1$. The coupling at the dressed trap bottom is directly Ω_2.

5.1.6 Interpretation of the resonances in terms of photon transfer

To give an enlightening interpretation in terms of photon transfer of the three transitions at $\omega_2 = \omega_1 \pm \Omega(\mathbf{r})$ and $\omega_2 = \Omega(\mathbf{r})$, we consider the case where atoms are coupled far from the resonant region $\omega_0(\mathbf{r}) \simeq \omega_1$ where the dressed trap has its minimum. The limit we will focus on is: $|\delta(\mathbf{r})| \gg \Omega_1$, when the spin angle θ is close to 0 or π. In this limit, the level spacing between dressed states can be approximated by $\Omega(\mathbf{r}) \simeq |\delta(\mathbf{r})| = |\omega_1 - \omega_0(\mathbf{r})|$, and the coupling strength for the transitions around ω_1

simplifies to Ω_2 for the strongest coupling and $\Omega_2\Omega_1^2/(4\delta^2)$ for the weakest. This expression suggest that the strongest coupling arises from a one-photon transition whereas the weakest concerns a three-photon transition. In the same spirit, the expression for the coupling strength of the low frequency transition, $\Omega_1\Omega_2/\omega_2$, suggests a two-photon transition, with one photon of frequency ω_1 and one photon with frequency ω_2. Indeed, we will discuss the three resonances in the light of the photon transfer represented in the bare state basis in Figure 5.3. The coupling in the dressed state basis at frequency $\pm\Delta$ or ω_2 is shown on the right hand side in this figure.

We will discuss the three cases (a) $\omega_2 \gtrsim \omega_1$, (b) $\omega_2 \lesssim \omega_1$ and (c) $\omega_2 \approx \Omega_1$.

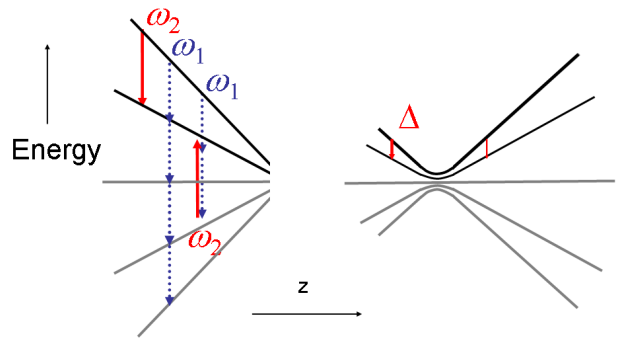

(a)

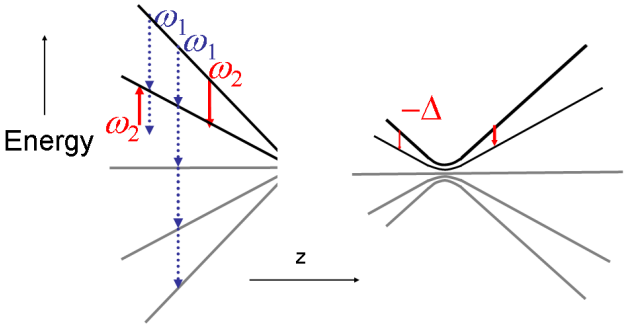

(b)

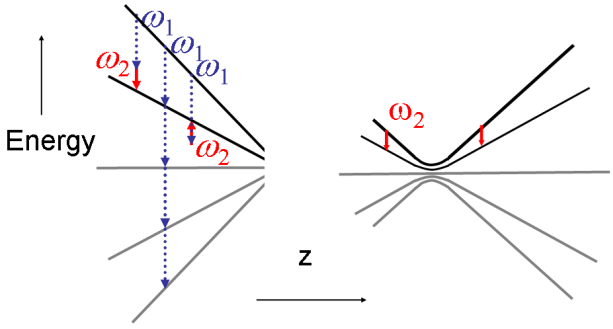

(c)

Figure 5.3: The transitions induced by the second rf field, represented in the bare state basis (left) or in the dressed state basis (right) for three different rf probe frequencies: (*a*) when $\omega_2 \gtrsim \omega_1$ (*b*) $\omega_2 \lesssim \omega_1$ and (*c*) direct transition at $\omega_2 \approx \Omega_1$.

(a) $\omega_2 \gtrsim \omega_1$

This corresponds to the case where $\Delta > 0$, or $\varepsilon = +1$. The resonance occurs at the two points where $\omega_2 = \omega_1 + \Omega(\mathbf{r})$. The outer resonance corresponds to the position $\theta_0 \ll 1$, $\delta < 0$ (or equivalently $\omega_1 < \omega_0(\mathbf{r})$) such that $\omega_2 \simeq \omega_1 + |\omega_1 - \omega_0(\mathbf{r})| = \omega_0(\mathbf{r})$. As shown on the left of Figure 5.3(a), it is a direct one photon resonance, a single rf photon being emitted at frequency $\omega_2 \simeq \omega_0(\mathbf{r})$ and with a coupling strength Ω_2. Note that this is also the situation we would get in the absence of the first dressing field.

On the contrary, for the inner resonance at position $\pi - \theta_0 \simeq \pi$, δ is positive such that $\omega_2 \simeq \omega_1 + |\omega_1 - \omega_0(\mathbf{r})| = 2\omega_1 - \omega_0(\mathbf{r})$. We now have a three photon resonance, thanks to the dressing field at ω_1. The resonance condition is $\omega_0(\mathbf{r}) = 2\omega_1 - \omega_2$, two photons of frequency ω_1 being emitted while a probe photon at ω_2 is absorbed, see Figure 5.3(a). This process has a much smaller coupling strength $\Omega_2\Omega_1^2/(4\delta^2)$.

(b) $\omega_2 \lesssim \omega_1$

In this case, $\Delta < 0$ or $\varepsilon = -1$. The resonances occur at positions $\mathbf{r}$ such that $\omega_2 = \omega_1 - \Omega(\mathbf{r})$. For the OR with δ large and negative, this simplifies to $\omega_2 \simeq \omega_1 - |\omega_1 - \omega_0(\mathbf{r})| = 2\omega_1 - \omega_0(\mathbf{r})$, and now the outer resonance corresponds to the three-photon process, with the smallest coupling $\Omega_2\Omega_1^2/(4\delta^2)$. On the other hand, the inner resonance matches to the direct one-photon coupling at frequency $\omega_2 \simeq \omega_0(\mathbf{r})$ and coupling Ω_2.

(c) $\omega_2 \sim \Omega_1$

This last case corresponds to coupling directly the dressed states at frequency $\Omega(\mathbf{r})$, their frequency separation. The two resonances, OR and IR, are again present. In the bare state basis, the OR corresponds to the emission of two photons at ω_1 and ω_2, and the IR is also a two-photon process, but with emission of ω_1 and absorption of ω_2, such that we have $\omega_0(\mathbf{r}) = \omega_1 \pm \omega_2$. As it is a two photon process, we expect a coupling strength of order $\Omega_2\Omega_1/\omega_2$ *at both positions*, OR and IR, in contrast to the two previous cases.

Let us point out finally that the polarization of the rf probe has to be chosen σ^+ (or at least transverse to the static field) for the two first process, for which the transition from m'_F to $m'_F - 1$ is either direct or a three-photon process: $-1 = -2 + 1$. On the contrary, it should be π for the third process, to have $-1 \pm 0 = -1$. It means that the last situation occurs with a probing rf field parallel to the static magnetic field.

5.2 Spectroscopy of the rf-dressed QUIC trap

In the previous theoretical section, we have shown that trapped dressed atoms can be outcoupled with an additional rf field, at three different frequencies ω_2. As we will see in this section, we have experimentally observed all the three transitions and were able to deduce the Rabi frequency Ω_1 of the first dressing field from the measurements.

5.2.1 Experimental procedure

In this section I will explain the experimental details for performing the spectroscopy in the rf dressed trap. The rf field is produced by the Tabor Electronics synthesizer, see section 2.6.1. The dressed trap is loaded in 500 ms with a ramp of 20,000 frequency points between 0.8 MHz and the final dressing frequency ω_1. This frequency is typically a few MHz with a Rabi frequency Ω_1 of order 50 kHz. At the end of this loading stage, a second rf with a fixed frequency ω_2 and Rabi frequency Ω_2 is switched on for a plateau of 2 seconds. The typical rf ramping scheme for these experiments is shown in Figure 5.4 below. The dressing rf power is kept constant during the loading stage and the plateau. The corresponding amplitude Ω_1 is adjusted by attenuating the $2\,V_{pp}$ sine output of the Tabor synthesizer. The rf attenuator is controlled from the computer using a parameter η between 0 and 1, setting the relative rf amplitude: $\Omega_1 = \eta\Omega_{max}$.

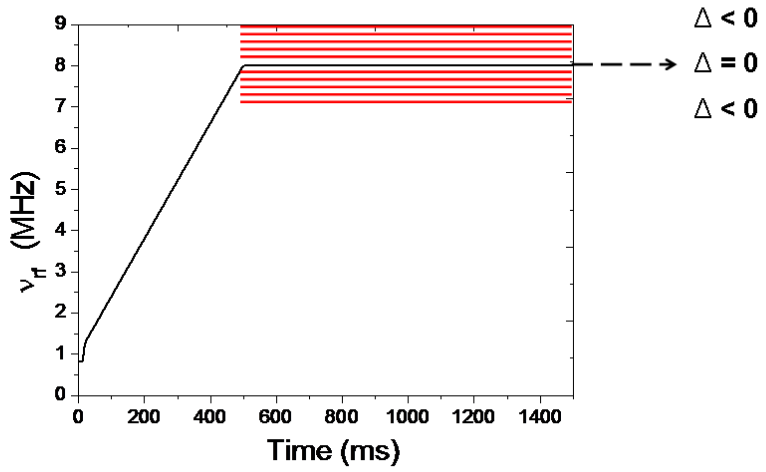

Figure 5.4: Evolution of the dressing frequency ω_1 (black line) and the probing frequency ω_2 (red lines) with time, in the case where $\omega_2 \sim \omega_1$.

At the end of the plateau, the atom number and the optical density are recorded after a time of flight of 7 or 10 ms, as a function of ω_2. For performing the spectroscopy, the probing rf frequency ω_2 is scanned across the final value of the dressing rf frequency ω_1, see the horizontal lines of Figure 5.4. We first expect to see two resonances when the value of $|\Delta|$ becomes close to Ω_1, or when the frequency ω_2 itself is close to Ω_1.

The second rf is produced by a second Stanford Synthesizer, see section 2.6.1. In order to fulfill the rotating wave approximation, the probing rf coupling strength Ω_2 was chosen to be around 0.3% of the dressing rf coupling strength Ω_1 for the spectroscopy experiments. For a dressing coupling strength of $\Omega_1 \approx 2\pi \times 55$ kHz we choose a probing rf coupling strength $\Omega_2 \approx 2\pi \times 180$ Hz[2].

[2]The probing rf coupling strength Ω_2 was not measured directly, but was estimated from the value of Ω_1 and the ratio of the rf powers at ω_1 and ω_2 measured just before the antenna. We use the fact that the rf amplitude scales as the square root of the rf power.

5.2.2 Results

We observed experimentally the three resonances predicted in the previous section. Four different sets of spectroscopic data were collected by changing different parameters, namely, the Rabi frequency Ω_2 of the probing field, the Rabi frequency Ω_1 of the dressing field, and its frequency ω_1.

varying Ω_2 The first set of data shows the broadening of the resonances with a larger probing field amplitude Ω_2. The spectra are recorded around $\omega_1 = 2\pi\times\ 8\,\mathrm{MHz}$ at an attenuation $\eta = 0.5$, for different probing rf amplitudes at the input of the antenna: $1\,\mathrm{V}_{pp}$, $0.3\,\mathrm{V}_{pp}$ and $0.1\,\mathrm{V}_{pp}$. The data are plotted as a function of the frequency difference $\Delta = \omega_2 - \omega_1$. In each case, we observe two resonances for $\Delta = \pm\Omega_1$. This is compatible with the previous results showing two resonances at $\omega_2 = \omega_1 \pm \Omega_1$. These resonances correspond to the ones illustrated in Figure 5.3 (a) and (b).

It is clear from Figure 5.5 that the resonances are broadened for a larger probing field amplitude. This is in agreement with the fact that the probe coupling is $\frac{\Omega_2}{2}(1 \pm \cos\theta)$, proportional to Ω_2. The smallest probing rf amplitude $0.1\,V_{pp}$ allows the most accurate determination of $\Omega(\mathbf{r}_0)$ at the bottom of the dressed trap, which is about $2\pi\times 50\,\mathrm{kHz}$. This gives a direct measurement of the dressing rf frequency for $\eta = 0.5$: $\Omega_1 = 2\pi \times 50\,\mathrm{kHz}$, and this result is independent from the initial cloud temperature.

We observe that the shape of the resonance peaks are not symmetric. We see that the atom number (or the integrated optical density) drops down slowly as ω_2 is approaching the resonance from the side $|\Delta| > \Omega_1$. When $|\Delta| = \Omega_1$ we lose almost all the atoms and for $|\Delta| < \Omega_1$ we go back to the initial atom number quickly. This asymmetric behavior can be explained through the energy distribution at temperature T. The resonance occurs at a position $\mathbf{r}$ such that $|\Delta| = \Omega(\mathbf{r})$. Hence, all the atoms with an energy $E > \Delta E$ larger than the trap depth ΔE defined at Eq.(5.12) will escape the trap. In the limit where $\Omega_2 \ll \Omega_1$, which is always the case here, this condition is simply $E > 2\hbar|\Delta| - 2\hbar\Omega_1$. While doing spectroscopy we start with $|\Delta| \gg \Omega_1$ and then come closer and closer to Ω_1. For higher values of $|\Delta|$ only atoms in the higher energy levels are coupled out of the trap. When we go closer to the resonance we outcouple more and more atoms. And when $|\Delta| < \Omega_1$ we are below the bottom of the rf dressed trap and we do not outcouple anymore, so we go back to the initial number of atom. Whatever the energy distribution $f(E)$ in the trap, this explains the sharp edge at $|\Delta| = \pm\Omega_1$ and the monotonic increase of the number of remaining atoms as $|\Delta|$ increases. The exact lineshape depends on the detail of the energy distribution, and would be exponential with a $1/e$ decay length $\Delta\nu = k_B T/2h$ for a harmonic trap[3]. In the case of the adiabatic potential, which becomes linear at large distances, the energy distribution $f(E)$ is modified, and so is the lineshape. An exponential fit of the wings of the spectra should still give an estimate of the initial temperature of the atoms in the trap using the relation $k_B T \simeq 2h\Delta\nu$. From Figure 5.5(d) the width of the fit gives $\Delta\nu \approx 130\,\mathrm{kHz}$ which corresponds to an initial temperature $T \approx 12.5\,\mu\mathrm{K}$. This is in good agreement

[3]The factor 2 comes from the fact that the atoms are in the $m'_F = 2$ state of the adiabatic potential (for the energy) and that we probe transitions with $\Delta m_F = \pm 1$

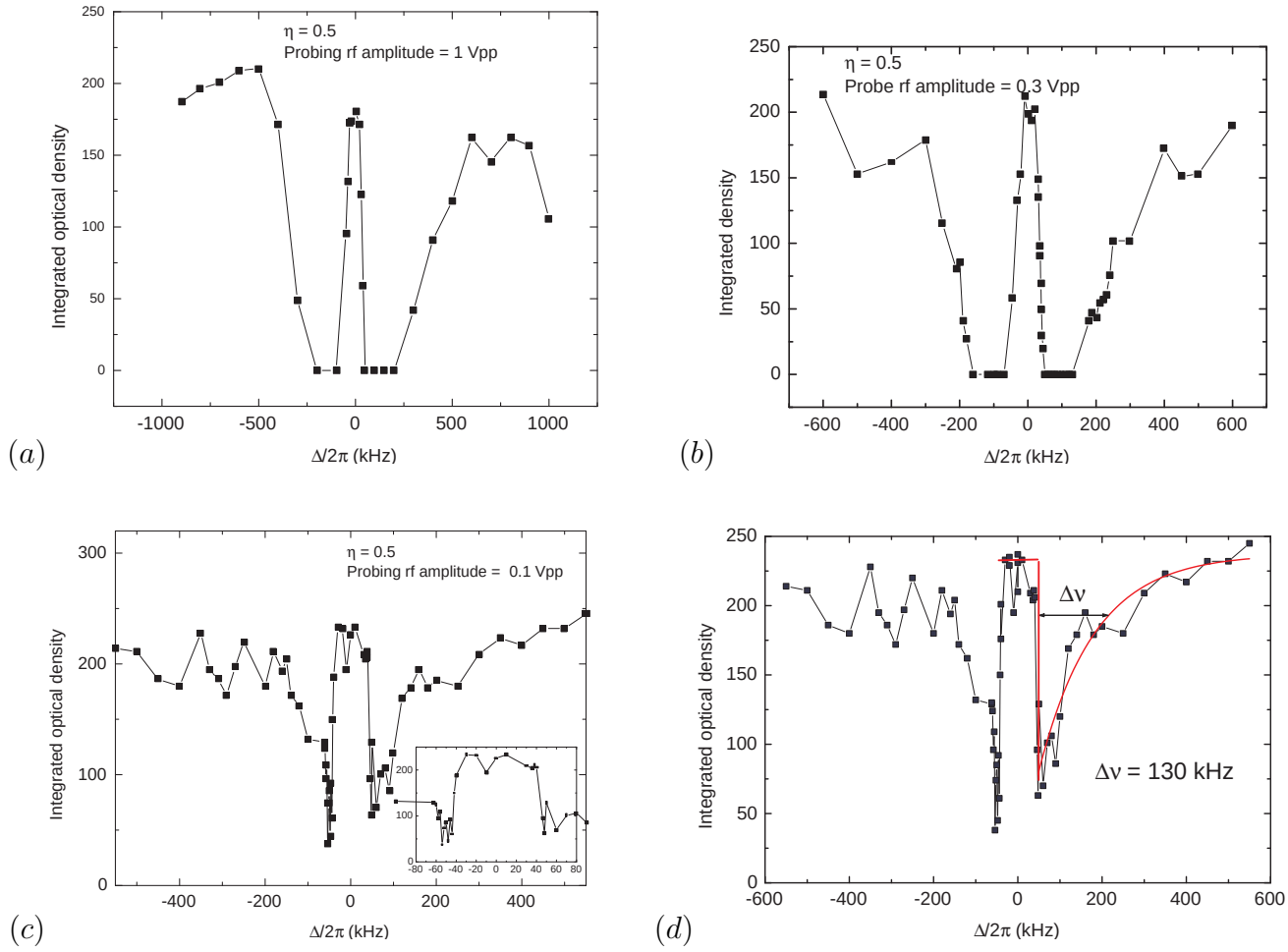

Figure 5.5: Spectroscopy of the dressed trap for $\eta = 0.5$ and for different values of probing rf amplitudes given by: (a) $1\,V_{pp}$; (b) $0.3\,V_{pp}$; (c) $0.1\,V_{pp}$. Note the different horizontal scales. Inset of figure (c): zoom around zero detuning. (d) An exponential fitting done to figure (c) in order to estimate the initial temperature of the atoms in the dressed QUIC: the $1/e$ decay is 130 kHz, corresponding to a temperature of 12.5 μK.

with the temperature of 11 μK deduced from the time of flight measurement. If the actual shape of the trapping potential is taken into account, simulations done in the group have shown indeed that the line width is slightly broadened.

Finally, the small asymmetry between the left wing and the right wing of the resonance at $\omega_1 \pm \Omega_1$ may be due to gravity. On the side $\Delta > 0$, the stronger coupling occurs for the OR. At the resonance point, the trap depth is also limited by gravity, which favors the expulsion of atoms at larger values of Δ. On the opposite, if $\Delta < 0$ the strongest resonance is the IR, which is more difficult to reach as the corresponding resonant surface is situated above the trapped atoms. The atoms need an additional energy $Mg\Delta z$ to escape, and $|\Delta|$ cannot be so large as in the previous case. The typical size of this effect is $Mg/(2\hbar\alpha) = 0.07$, and the expected asymmetry is thus

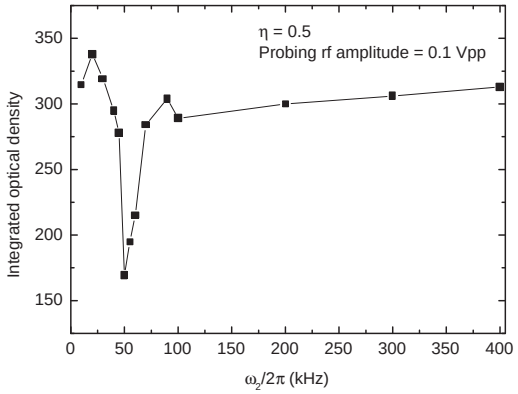

Figure 5.6: A direct probing of the resonance at $\omega_2 \approx 2\pi \times 50\,\mathrm{kHz}$.

rather small.

low frequency spectrum In order to check the value of Ω_1 obtained in the first set of experiments, we tried to probe the resonance directly at $\omega_2 \approx 2\pi \times 50\,\mathrm{kHz}$. This resonance correspond to the one predicted in Figure 5.3(c). A rf spectrum was recorded at low probing frequency. Here again, all the atoms are coupled out of the dressed trap for a frequency $\omega_2 = 2\pi \times 50\,\mathrm{kHz}$, as shown on Figure 5.6. We thus recover exactly the same value for Ω_1, the dressing Rabi frequency.

varying Ω_1 In our third experiment we observed the dependency of the resonance frequency with the rf amplitude Ω_1. Spectra are recorded around $\omega_1 = 2\pi \times 8\,\mathrm{MHz}$ for different relative amplitudes $\eta = 0.3$, 0.5 and 0.75. The resonances on both sides of the dressing frequency ω_1, are now shifted respectively by 30 kHz, 50 kHz and 75 kHz from the dressing frequency, see figure 5.7. This is in agreement with resonances at positions $\Delta = \pm\Omega_1$ with $\Omega_1 = \eta\Omega_{max}$, and $\Omega_{max} = 2\pi \times 100\,\mathrm{kHz}$ at $\omega_1 = 2\pi \times 8\,\mathrm{MHz}$. This experimental measurement of Ω_1 is direct and scales linearly with η. These values differ from the ones obtained by the other methods described in chapter 3. However, the previous methods are indirect; the oscillation frequency method is affected by the non harmonic character of the trap and by the temperature, and the Stern-Gerlach method gives a measurement only around $\omega_1 \sim \omega_{\mathrm{min}}$. In addition, these methods do not exhibit such a clear linear dependence with the amplitude. This is why we think that the spectroscopic method is the most reliable one for measuring Ω_1.

varying ω_1 The fourth experiment gives an indication that the Rabi frequency Ω_1 depends on the rf frequency ω_1. Spectra are recorded around $\omega_1 = 2\pi \times 6\,\mathrm{MHz}$ and $2\pi \times 3\,\mathrm{MHz}$ at a probing rf amplitude $= 0.2\,V_{pp}$ and a relative amplitude $\eta = 0.5$, see Figure 5.8. The probe amplitude was increased to $0.2\,V_{pp}$ to enhance the spectrum visibility. The resonance is slightly shifted as compared to the 8 MHz case, as peaks are present at about 60 kHz and 70 kHz respectively from the dressing frequency, instead of

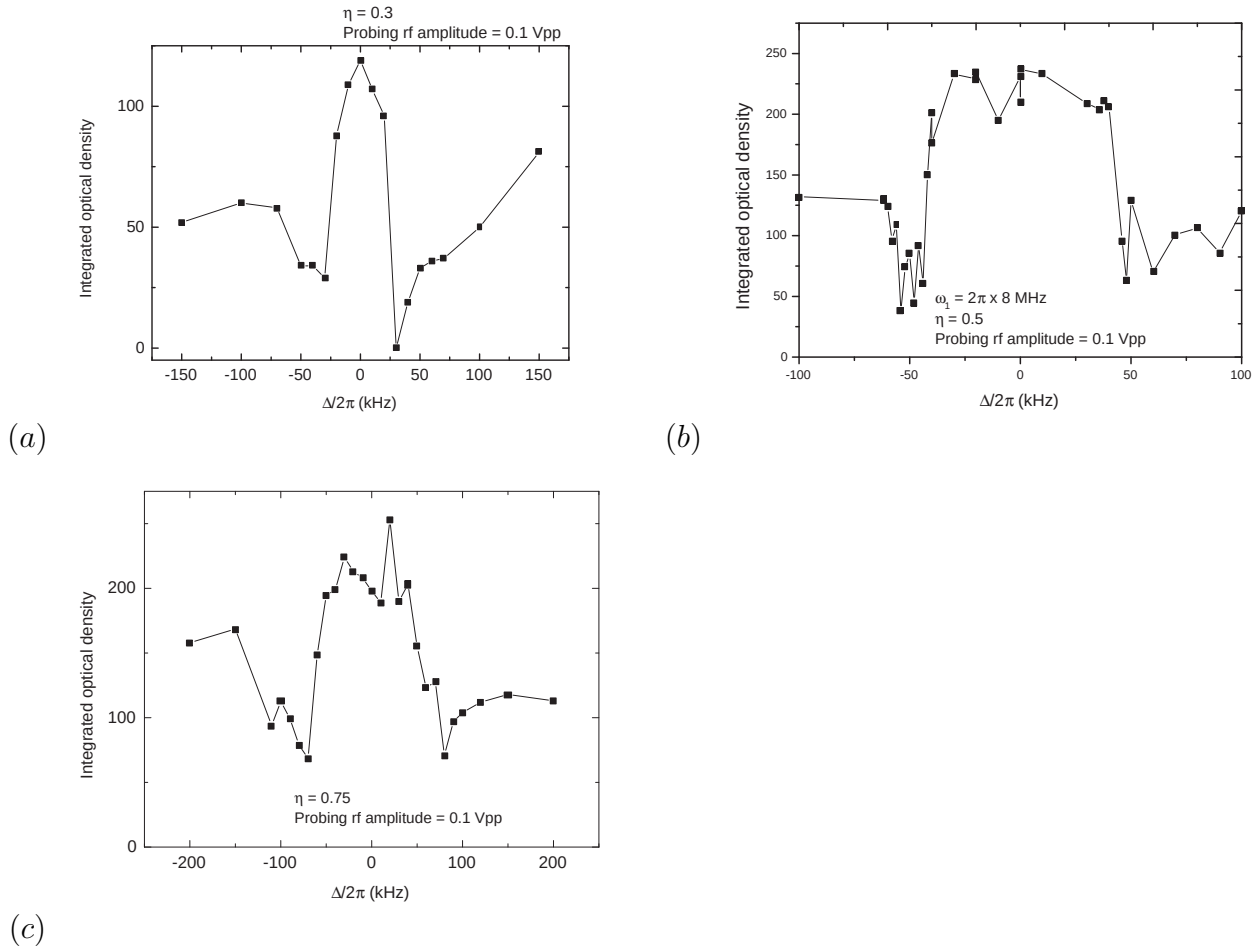

Figure 5.7: Spectroscopy of the dressed trap with a probing rf amplitude of $0.1\,V_{pp}$ and for different values of η: (a) : $\eta = 0.3$; (b) : $\eta = 0.5$; (c) : $\eta = 0.75$. A resonance is observed on both sides of the dressing frequency ω_1, at ± 30 kHz in (a), ± 50 kHz in (b) and ± 75 kHz in (c). (b) is a zoom of Figure 5.5*c*.

50 kHz previously. This is an indication that the Rabi frequency Ω_1 depends on the rf frequency ω_1 and is larger at smaller frequency. We tried to understand the reason for this dependency of Ω_1 with ω_1. We first suspected that due to the displacement of the atomic cloud when the dressing frequency ω_1 increases, the atoms could enter a region where the rf field varies in space. But this is not true since for a variation of ω_1 from 9 MHz to 3 MHz the atomic cloud displacement is $\approx 600\,\mu$m, which is $\approx \frac{1}{25}^{th}$ of the radius of the rf antenna. For such a small displacement of the atomic cloud compared to the radius of the rf antenna, the magnetic field change is negligible. Instead, we suspect a frequency dependence of antenna response to be the cause for this change in Ω_1 with ω_1.

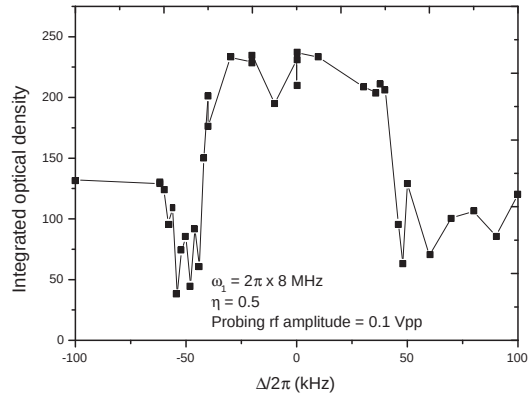

(a)

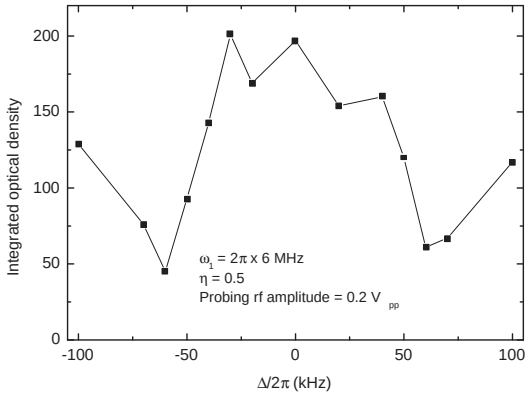

(b)

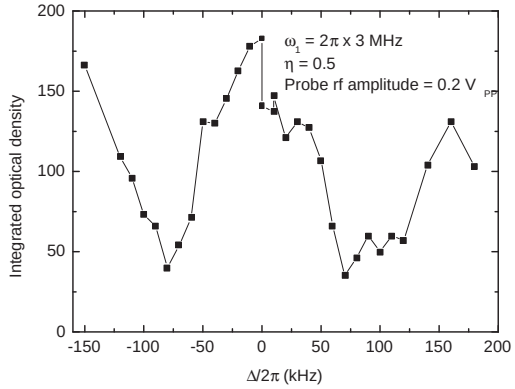

(c)

Figure 5.8: Spectroscopy of the dressed trap, with a dressing frequency (*a*): $\omega_1 = 2\pi \times 8\,\mathrm{MHz}$, (*b*): $\omega_1 = 2\pi \times 6\,\mathrm{MHz}$ and (*c*): $\omega_1 = 2\pi \times 3\,\mathrm{MHz}$. Figure (*a*) is identical to Figure 5.7*b*. The relative amplitude η is 0.5 for all the three plots and the probing rf amplitude is $0.1\,V_{pp}$ for (*a*) and $0.2\,V_{pp}$ for (*b*) and (*c*). A resonance is observed at $\pm 50\,\mathrm{kHz}$ from the dressing frequency in plot (*a*), $\pm 60\,\mathrm{kHz}$ in (*b*) and $\pm 70\,\mathrm{kHz}$ in (*c*).

5.3 Evaporative cooling in the rf dressed trap

5.3.1 Principle

In this section we demonstrate rf induced evaporative cooling in the rf-dressed trap. In the conservative magnetic QUIC trap we use forced evaporative cooling to reach quantum degeneracy [34]. In rf-forced evaporative cooling, a resonant rf radiation selects the most energetic atoms and transfers them from a trapped spin state to an untrapped spin state. Once these rapid atoms are lost, the average energy of the remaining atoms decreases after rethermalization through collisions. By this process the phase space density increases and the temperature decreases, which is the signature of evaporative cooling.

Here, we implement this idea in the dressed trap, which means that we use *two* rf frequencies: one at ω_1 with a strong amplitude Ω_1 to dress the atoms, and another one at $\omega_2 \neq \omega_1$ with a much smaller amplitude Ω_2 to induce spin flips of the dressed atoms, as in the spectroscopy experiments. This cooling scheme was studied in our group by C. Garrido Alzar *et al.* [23] and implemented in the group of J. Schmiedmayer [41] in the case where the atoms are trapped away from the first rf resonance ($\omega_1 < \omega_{\min}$ and $\delta < 0$ everywhere). In contrast to what was proposed and implemented before, we use here mainly the low frequency transition.

5.3.2 Experimental procedure

According to the results from the previous section, the rf which was used to probe the spectroscopy is now used to perform evaporative cooling. The three resonances observed for different probe frequencies in the previous section can be used for this. The efficiency of the evaporation process is not the same for each of the three resonances. We found that the evaporative cooling is much more efficient by using an evaporation rf ramp ω_2 around Ω_1 rather than around $\omega_1 \pm \Omega_1$. We believe that this is due to a more symmetric out coupling around Ω_1, which involves on both sides (IR and OR) a 2 photon process with the same coupling $\Omega_1\Omega_2/\omega_2$.

In this section I will explain the experimental details for performing evaporative cooling in our rf dressed trap. In order to remove dynamically the high energy atoms, the second rf ω_2 is swept from a given initial value down to a value slightly higher than Ω_1. Thanks to the spectroscopy experiments, we know the value of $\Omega_1 = 2\pi \times 50\,\mathrm{kHz}$ in our experimental conditions. The Stanford 2 synthesizer which was used for the spectroscopy generates an evaporation linear rf ramp, from 600 kHz to 55 kHz typically, for a duration of 4 s right after loading the atoms into the dressed trap. The rf amplitude was optimized to $400\,\mathrm{mV}_{pp}$, a value larger than the $100\,\mathrm{mV}_{pp}$ which was used for the spectroscopy. The dressing and evaporation amplitudes were kept constant throughout the evaporation ramp.[4] The temperature of the atoms was deduced from the width of the atomic cloud along z after a time of flight for various values of the final evaporation frequency. The number of atoms N for each final value of ω_2 is estimated by taking the mean value of N obtained during the time of flight (average over 7 to 8 pictures) measurements. This is done to average shot to shot fluctuations in the atom number of the order of $\pm 20\,\%$. In a harmonic trap, the phase space density ϕ_{psd} at the trap center is given by [42]:

$$\phi_{psd} = N \left(\frac{\hbar}{k_B T} \right)^3 \omega_x \omega_y \omega_z. \tag{5.19}$$

But in reality, in the z direction, depending on the temperature, the atoms may explore the linear region more than the harmonic one. To which energy should we compare the temperature? The atoms enter the linear region if the two terms Ω_1^2 and $\delta(\mathbf{r})^2$

[4] We also tried to reduce the evaporation amplitude at different rates during the evaporation ramp. This was intended to make the evaporative cooling more efficient as the trap depth is reduced, to avoid the resonance broadening and get closer to the trap bottom. However, we did not see any improvement in the temperature nor in the phase space density.

below the square root in the definition of $\Omega(\mathbf{r})$ of Eq.(3.10) are comparable, that is if $\delta(\mathbf{r}) \sim \Omega_1$ and $\Omega \sim \sqrt{2}\,\Omega_1$. The corresponding energy $E_{\rm lin}$ with respect to the trap bottom is

$$E_{\rm lin} = 2\hbar\,(\Omega - \Omega_1) = 2(\sqrt{2}-1)\,\Omega_1 \simeq 0.83\,\Omega_1. \tag{5.20}$$

If we compare the initial temperature $T \approx 5\,\mu$K to the typical energy $0.83\hbar\Omega_1$ above which the trap is linear, we find $0.83\frac{\Omega_1}{2\pi} = 40\,$kHz $= 2\,\mu\text{K} \times k_B/h$, and we conclude that the cloud is definitely entering the linear part at the beginning of the evaporation.

For a trap linear along z (with a potential energy $2\hbar\alpha z$) and harmonic along x and y, the 1D density along z at temperature T is of the order of $n_1 \sim N \times 2\hbar\alpha/(k_B T)$. The phase space density can be estimated using this formula:

$$\phi_{psd} \sim N \left(\frac{\hbar}{k_B T}\right)^2 \omega_x\omega_y \frac{2\hbar\alpha\lambda_{\rm dB}}{k_B T} \propto \frac{N}{T^{\frac{7}{2}}}. \tag{5.21}$$

However, this would be valid at the beginning of the evaporation only. To keep a single formula, we decided to use Eq.(5.19) to calculate ϕ_{psd} during the whole evaporation process. By this mean, we may underestimate a little bit the phase space density at the beginning of the evaporative cooling.

5.3.3 Results

In this section, I present the experimental results of evaporative cooling in the rf dressed trap. During an efficient evaporative cooling process, an increase in the phase space density must occur. After transferring the atoms into the dressed QUIC, we applied an rf evaporation ramp starting from 600 kHz to various final frequencies close to Ω_1. The results are shown in Figure 5.9*a*. We see an increase in the phase space density by a factor 8 with a final detuning of 20 kHz. When the detuning is smaller than 20 kHz, we see a decrease in phase space density, which could be either due to fluctuations in the atom numbers[5] or to the fact that we are too close to the bottom of the trap and start to evaporate to coldest atoms.

We found that the initial conditions in the QUIC are very important to reach a low temperature and a high phase space density. We tried with various initial conditions to improve the final phase space density and temperature and found an optimum starting point, see Figure 5.9 (*b*), (*c*) and (*d*). These situations are explained in the following paragraphs.

First, we started with an initial temperature of 11.6 μK and a phase space density of 1.4 $\times 10^{-4}$ in the QUIC, see Figure 5.9 (*b*). After the transfer of the atoms into the dressed QUIC, the phase space density decreases to 3.5 $\times 10^{-5}$ and the temperature to 5.34 μK. We expect that the temperature decreases because of the trap deformation, the dressed trap being much shallower that the QUIC trap. However, it should decrease even more if the transfer is adiabatic, which is not the case since the phase space density also decreases. This is due to the fact that the oscillation frequency in the x direction

[5]The signal becomes very small when the final frequency is very close to Ω_1. With a very small signal it is difficult to do a good fitting and estimate the number of atoms N. This leads to an inaccuracy of the order of 20% on N.

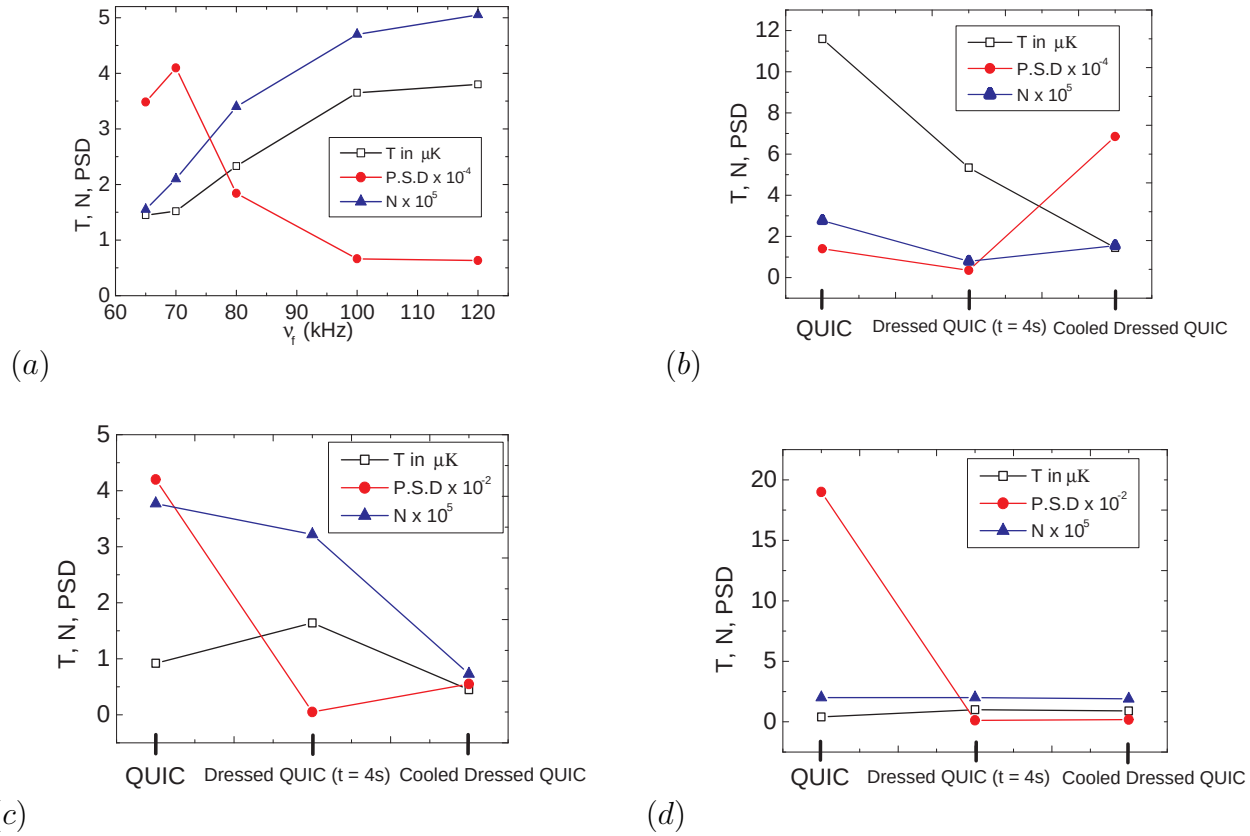

Figure 5.9: (a): Evolution of the atom number N, the temperature T and the phase space density (PSD) in the dressed trap as a function of the final frequency of the evaporation ramp. The linear evaporation ramp starts at a frequency of 600 kHz. (b), (c) and (d): Evolution of the temperature, the phase space density and the number of atoms during the different stages of loading for three different initial conditions in the QUIC trap, see text.

is only a few Hz, which makes the adiabaticity condition $\dot{\omega_x} \ll \omega_x^2$ difficult to satisfy in the x direction. From this new starting point, we applied an evaporation ramp from 600 kHz to 70 kHz and observed a final temperature of 1.45 μK and phase space density of 6.85 $\times 10^{-4}$. This configuration allows a net gain in phase space density between the QUIC trap and the dressed trap, but with a modest final phase space density.

In a second sequence, we started with a colder sample at an initial temperature of 0.92 μK and a phase space density of 4.2×10^{-2}, see Figure 5.9 (c). After transfer into the dressed trap, the phase space density drops down to 5×10^{-4} and the temperature slightly raises to 1.64 μK. Then we applied an evaporation ramp from 150 kHz to 65 kHz and obtained a final temperature of 450 nK and phase space density of 5.5×10^{-3}. The final phase space density is thus less than the initial one in the QUIC trap. However, this final conditions are better than the previous case, and we could improve the final situation by starting from a colder sample.

Finally, we tried to start with an even colder sample, at an initial temperature of 412 nK and a phase space density of 0.19, see Figure 5.9 (*d*). After the transfer to the dressed trap, the phase space density drops down dramatically by two orders of magnitude, to 1.29×10^{-3}, and the temperature increases to 1.02 µK. We then applied an evaporation ramp from 150 kHz to 70 kHz and ended up with a final temperature of 900 nK and a phase space density of 1.82×10^{-3}, only slightly higher. In this condition, the transfer really degrades the phase space density and the evaporative is not very efficient, as the initial atom number is too low. Comparing these data with the previous case, it is not recommended to start with a too cold sample — especially a BEC.

After analyzing the above three possible scenarios we can conclude that there is an optimal intermediate initial temperature, neither too hot nor too cold as in the case of Figure 5.9 (*c*) to reach the better final conditions.

The phase space density figures presented above were calculated from the temperature deduced from the time of flight measurements. We must note however that these figures can be overestimated. As a matter of fact, the temperature is measured along z, the same direction in which the evaporation takes place with the second rf field. Depending on the relative time scales of evaporation and thermalization by elastic collisions, the atomic cloud could be out of equilibrium, with effective temperatures $T_x, T_y > T_z$. In order to estimate this effect, we have to check the efficiency of evaporative cooling using the parameter η_{evap} defined as $\eta_{\text{evap}} = \frac{\Delta E}{k_B T}$, where ΔE is the trap depth[6]. Efficient evaporation is possible when $\eta_{\text{evap}} > 3$, and the run-away regime even requires $\eta_{\text{evap}} > 5$ in an harmonic trap. In practice, however, a very large η_{evap} leads to very slow evaporation, so that η_{evap} between 7 and 10 is a good compromise. In our case this parameter η_{evap} is of the order of 6 at the beginning and continuously decreases down to 2.5 during evaporation. The decrease of η_{evap} is an indication that the thermalization process is too slow in our cloud. Indeed, the initial density of $\approx 10^{11}\text{cm}^{-3}$ corresponds to $\approx$2 collisions per second, which leads to a long thermalization time. Our typical 5 s evaporation ramp is not slow enough as compared to this time, and an out of equilibrium cloud is produced. This situation can be improved by increasing the oscillation frequencies in the trap which will improve the initial density and the collision rate.

5.4 Conclusion

We performed spectroscopic studies in the radio frequency dressed trap. We predicted and observed three resonances, with different coupling strength, involving 1-, 2- and 3-photon processes. The dressing amplitude Ω_1 is evaluated from the resonances and found to increase linearly with the relative rf amplitude parameter η. Using the knowledge of the spectroscopy, we applied evaporative cooling to the rf dressed trap and could see a reduction in the temperature together with a modest increase in the phase space density. Even if the effect is likely less pronounced than naively deduced from the temperature measurements along z, we believe that evaporative cooling indeed

[6] 'Atomes ultra-froids' by J.Dalibard, Année 2006.

takes place. However, it is not efficient enough to reach quantum degeneracy as our starting conditions are not good enough. In particular, the initial density is too low. One limitation in these experiment is the oscillation frequency in the x direction. As we have only a few Hz along the x direction it is difficult to have an adiabatic transfer of the atoms from the QUIC trap to the dressed QUIC trap. We observed a reduction of the phase space density by at least a factor of ≈ 4 while transferring the atoms from the QUIC to the dressed QUIC. Increasing the oscillation frequency in the x direction would reduce the time constant $\tau \approx \omega_x^{-1}$ for the adiabaticity. This would help us to fulfill the adiabaticity condition in the x direction. This would also help to increase the evaporation dynamics as the collision rate would increase due to the increase in the density. One solution to improve the situation of the evaporative cooling would be to start from a quadrupolar trap instead of QUIC trap. The horizontal oscillation frequencies are indeed larger in this case. As a starting point, we demonstrated the loading of a dressed quadrupolar trap [43], which is presented in the next chapter.

Chapter 6

Ultra cold atoms confined in a dressed quadrupole trap

The motivation of this study is the realization of a quasi-2D degenerate gas in situations where a cylindrical symmetry in atom trapping is necessary. This particularly occurs in the study of vortices generation [44] and dynamics either in the trapping geometry of an oblate trap or in a toroidal trap [45]. The study of quantized circulation [45] and related superfluid propagation phenomena [46] would particularly benefit of the experimental realization of this circular geometry.

A quadrupole magnetic trap with the symmetry axis oriented in the vertical direction constitutes a first step in the realization of an azimuthal symmetry trap. The adjunction of a resonant rf can make this trap almost hermetic, the atoms being gathered far from the zero magnetic field region. A region of low rf coupling is still present and could induce atom losses; however, this region can be placed away from the center of the atomic cloud, like in a TOP (Time Orbiting Potential) trap [47].

The question of loading a rf dressed quadrupole trap (DQ trap) from a reservoir of atoms already stored in a Ioffe-Pritchard trap has been addressed in the thesis of of O. Morizot [28, 43]. Here, I will present results of loading the DQ trap directly from an atomic vapor in a MOT. This would allow to apply evaporative cooling in the dressed trap from the beginning, in a more favorable geometry where the horizontal oscillation frequencies are larger than in the dressed QUIC. Since the quadrupolar trap at work in our experimental set-up is oriented horizontally and hence not in the direction of the gravitational field, the resulting geometry of the trap is not circular. For what concerns the question of loading, this lack of circular geometry does not constitute an important issue.

The chapter is organized as follows: I first explain the radio frequency polarization effects in the quadrupole trap, then the loading schemes for dressing the quadrupolar trap are presented and experimental results are discussed.

6.1 Radio-frequency polarization effects in the trap

In this section I will explain the importance of rf polarization for dressing a quadrupolar trap. Up to now, the effects of the rf polarization have been neglected. In the case of the dressed QUIC trap described in chapter 3 and 5, the magnetic field at the position of the atoms was essentially parallel to the $x-z$ plane, having only a small component in the y direction. With a rf source polarized along y, the coupling is then maximum and the consequences of the small dependence of the coupling with position for off-plane atoms were ignored. In a quadrupolar magnetic field however, the static magnetic field takes all possible orientations which makes essential the role of the rf polarization. For example, with a linear polarization along y the coupling vanishes along the y axis of the quadrupolar field, resulting in holes in the dressed trap. This is explained in the thesis of O. Morizot [28] and in Ref. [43]. In our case we start with an initial temperature of $\approx 400\,\mu$K which leads to a continuous loss of atoms during the loading process, when the dressing rf frequency ω_1 is increased, as the atoms have enough energy to escape through these holes. The presence of the holes reduces the lifetime of the dressed atoms. Linearly polarized rf can work only if the initial temperature is low enough such that the atoms are lying at the bottom of the bubble and don't reach the holes at the equator. Spontaneous evaporation of the more energetic atoms through the holes was observed in the group in this situation [43].

To increase the life time in the dressed quadrupole trap, it is better to use a circularly polarized rf (σ_z^- with respect to the quantization axis $\mathbf{e}_z$) which gives a maximum coupling at the lowest point of the bubble trap where the static magnetic field is pointing downwards (towards $-\mathbf{e}_z$). The lowest point is a stable trapping location for the atoms, due to gravity. The point of zero coupling sits at the top of the bubble, where the direction of static magnetic field points upwards and where the atomic density is minimum. In the equator we have half of the maximum coupling. This gives a bubble with only one hole at the top which will be an ideal situation for our experiment. This is the reason why we use to dress the quadrupole trap a circularly polarized σ_z^- rf field, with respect to the $\mathbf{e}_z$ axis.

Let us now describe the static magnetic field. The magnetic field produced by the quadrupole coils of axis y is given by

$$\mathbf{B}_{dc}(\mathbf{r}) = b'(z\mathbf{e}_z + x\mathbf{e}_x - 2y\mathbf{e}_y) = B_{dc}(\mathbf{r})\mathbf{e}_Z \tag{6.1}$$

where b' is the magnetic field gradient in the z direction. One defines as X,Y and Z the axis of the local frame attached to the static magnetic field. Z is the direction of the static magnetic field taken as quantization axis. The atoms are attracted towards the iso-B surface, which is a sphere contracted along the y axis, that is an ellipsoid given by the equation $\ell = \sqrt{x^2 + 4y^2 + z^2}$. ℓ is the "radius" of the bubble and is related to ω_1 through $\ell = \dfrac{\hbar\omega_1}{g_F\mu_B b'}$. This is sketched in Figure 6.1. The distance to the vertical axis is defined as $r = \sqrt{x^2 + 4y^2}$. Any point $M(x, y, z)$ on the ellipsoid can be mapped onto a point $M'(x, 2y, z)$ on the sphere of radius ℓ by a projection along y. Using the spherical coordiantes one the sphere, any point on the iso-B surface can be written in

terms of the angles θ and φ where θ and φ are the zenithal and azimuthal co-ordinates of the point M':

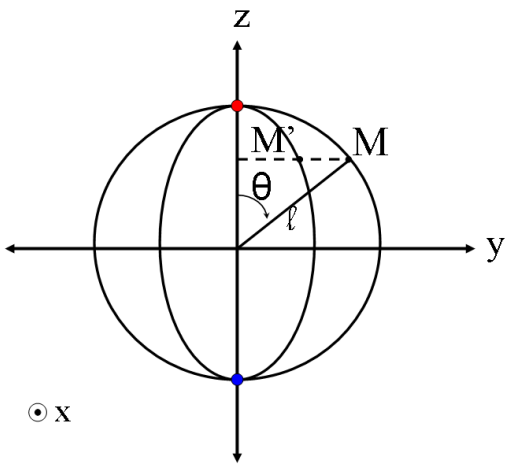

Figure 6.1: This figure shows a cut of the ellipsoid in the $y-z$ plane. The ellipsoid is contracted by a factor of 2 along the y axis. The radius of the ellipsoid along x and z is given by ℓ. The blue and red points at $z = \pm\ell$ represents the poles of the ellipsoids.

$$\begin{aligned} x &= \ell \sin\theta \cos\varphi = r\cos\varphi && (6.2)\\ 2y &= \ell \sin\theta \sin\varphi = r\sin\varphi && (6.3)\\ z &= \ell\cos\theta. && (6.4) \end{aligned}$$

We can now write the circularly polarized σ_z^- rf field $\mathbf{B}_1(\mathbf{r},t)$ as

$$\mathbf{B}_1(\mathbf{r},t) = B_{-1}\mathbf{e}_-(t) \tag{6.5}$$

where

$$\mathbf{e}_-(t) = \cos\omega_1 t\ \mathbf{e}_x - \sin\omega_1 t\ \mathbf{e}_y. \tag{6.6}$$

Again, we assume that the rf field produced by the antennas is homogeneous on the scale of the atomic cloud, with an amplitude B_{-1}. Substituting Eq.(6.6) in Eq.(6.5), we get

$$\mathbf{B}_1(\mathbf{r},t) = B_{-1}\cos\omega_1 t\ \mathbf{e}_x - B_{-1}\sin\omega_1 t\ \mathbf{e}_y. \tag{6.7}$$

This field can be realized with two antennas of axis x and y and a phase shift of $-\frac{\pi}{2}$. Now the unit vectors $\mathbf{e}_x$ and $\mathbf{e}_y$ can be expressed in terms of the unit vectors in the local frame $\mathbf{e}_X$, $\mathbf{e}_Y$ and $\mathbf{e}_Z$ as follows:

$$\begin{aligned} \mathbf{e}_x &= \cos\varphi\cos\theta\,\mathbf{e}_X + \cos\varphi\sin\theta\,\mathbf{e}_Z + \sin\varphi\,\mathbf{e}_Y && (6.8)\\ \mathbf{e}_y &= -\sin\varphi\cos\theta\,\mathbf{e}_X - \sin\varphi\sin\theta\,\mathbf{e}_Z + \cos\varphi\,\mathbf{e}_Y. && (6.9) \end{aligned}$$

Substituting Eq.(6.8) and Eq.(6.9) into Eq.(6.6) we get

$$\mathbf{e}_-(t) = \cos(\omega_1 t - \varphi)\cos\theta\,\mathbf{e}_X + \cos(\omega_1 t - \varphi)\sin\theta\,\mathbf{e}_Z - \sin(\omega_1 t - \varphi)\,\mathbf{e}_Y. \tag{6.10}$$

Now we can write the Hamiltonian of the system as

$$H_T(\mathbf{r}, t) = \frac{g_F \mu_B}{\hbar}\mathbf{F}.(\mathbf{B}_{dc} + \mathbf{B}_1(\mathbf{r}, t)). \tag{6.11}$$

At every point $\mathbf{r}$, Eq.(6.11) can be written as

$$H_T(\mathbf{r}, t) = \omega_0(\mathbf{r})F_Z + V_{-1}(\mathbf{r}, t) \tag{6.12}$$

where $V_{-1}(\mathbf{r}, t)$ is defined by the expression

$$V_{-1}(\mathbf{r}, t) = \Omega_{-1}\mathbf{F}.\mathbf{e}_-(t) \tag{6.13}$$

and $\Omega_{-1} = \dfrac{g_F \mu_B B_{-1}}{2\hbar}$ is the Rabi frequency of the rf field.

We apply the same treatment as we did in the chapters 3 and 5 for the Hamiltonian $H_T(\mathbf{r}, t)$ to go to the frame rotating at the frequency ω_1. After a rotating wave approximation, the interaction Hamiltonian $R_1^\dagger V_{-1}(\mathbf{r}, t)R_1$ is given by

$$\begin{aligned} R_1^\dagger V_{-1}(\mathbf{r}, t)R_1 &= \Omega_{-1}\,(1 - \cos\theta)\,[-\cos\varphi F_X + \sin\varphi F_Y] && (6.14)\\ &= \Omega_{-1}\left(1 - \frac{z}{\ell}\right)\left[-\frac{x}{r}F_X + \frac{2y}{r}F_Y\right]. && (6.15) \end{aligned}$$

We have removed the term in F_Z, parallel to the static magnetic field, which does not induce coupling between the spin states to first order. In the above expression $z = \pm\ell$ indicates the two poles and $z = 0$ represents the equator. At any point of fixed z on the ellipsoid, the coupling strength is equal to $\Omega_{-1}\left(1 - \frac{z}{\ell}\right)$. We see that the coupling vanishes due to the term $\left(1 - \frac{z}{\ell}\right)$ at the upper point $z = +\ell$ (minimum coupling), and it gives a maximum rf coupling of $2\Omega_{-1}$ at the lower point $z = -\ell$ where the static dc magnetic field is pointing downwards. At the equator where $z = 0$, the rf coupling strength becomes Ω_{-1} which is half its maximum value at the lower point. If we would have used σ_z^+ circularly polarized rf wave for dressing the atoms, we would have got a maximum coupling at the upper point (red point in Figure 6.1) which is an unstable location for the atoms due to gravity, and a hole at the bottom of the trapping shell.

To implement this experimentally, we use two rf antennas (kept orthogonal to each other in x and y axis) and two rf amplifiers (10 W) after the 90 degree phase shifter/power splitter (QE 01-412 Pulsar 1-10 MHz) as shown in Figure 2.12 to produce circularly polarized rf wave.

6.2 Loading Scheme

The quadrupole trap consists of two identical coils carrying opposite currents. This trap clearly has a single center where the field is zero. This configuration cannot produce a

BEC because atoms are lost from the trap due to Majorana spin flip transitions at low B values near the trap center. Another consequence of the presence of this zero field point is that it is not possible to dress the atoms from below the resonance as we did in the QUIC trap (it would require a negative frequency). The usual loading method doesn't work in this case.

We use a different method to load the atoms into the dressed quadrupole trap. To dress the atoms, we need a way to place them in a non zero magnetic field region. We thus first load the atoms into a shifted MOT using a bias field in the z direction. The atoms are then located 3 mm away from the real zero of the quadrupolar trap. The dressing is done after the molasses stage in the presence of a uniform x field for optical pumping. To fix the position of the atomic cloud at this location $\mathbf{r_0}$ (3 mm away from the quadrupole center) the rf field is first ramped up to the pumping field. After reaching this resonance both quadrupole trap field $\omega_0(\mathbf{r_0}, t)$ and rf field frequency $\omega_1(t)$ are ramped together to maintain the atoms at the resonance location $\delta(\mathbf{r_0}, t) = 0$. We fix the position of the atoms at resonance because this corresponds to a potential minimum for the atoms. In the following section we give a detailed step by step procedure of this loading scheme

1. the MOT is run in an offset vertical field of 2 G, done with a pair of Helmholtz coils of axis z, such that the MOT is shifted 3 mm below the center of the quadrupole trap.

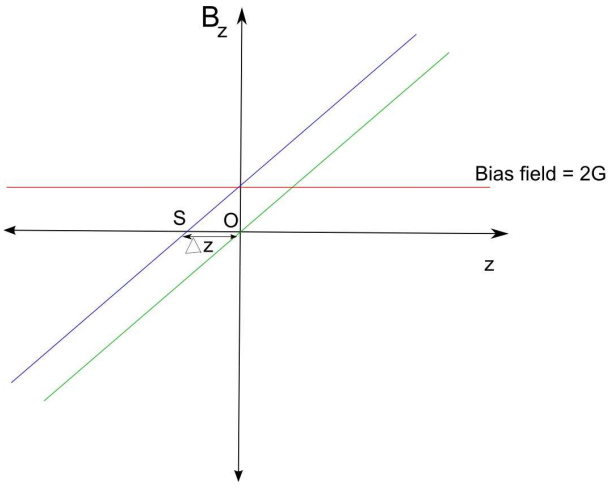

Figure 6.2: B_z v/s z plot for a shifted MOT: O represents the MOT center and S represents the MOT shifted by a distance of $\Delta z = 3$ mm in the z-direction after switching on the shift coils to produce a vertical bias field of 2 G.

2. all the magnetic fields are switched off for the molasses (except the Earth magnetic field compensation).

3. a uniform field B_{0x} oriented along x is switched on for optical pumping, with $B_{0x} = 2$ G (it corresponds to a magnetic level spacing of 1.4 MHz in the $F = 2$

state). The energy is plotted versus z for the state $m_F = 2$ in Figure 6.3. At this stage, it is uniform.

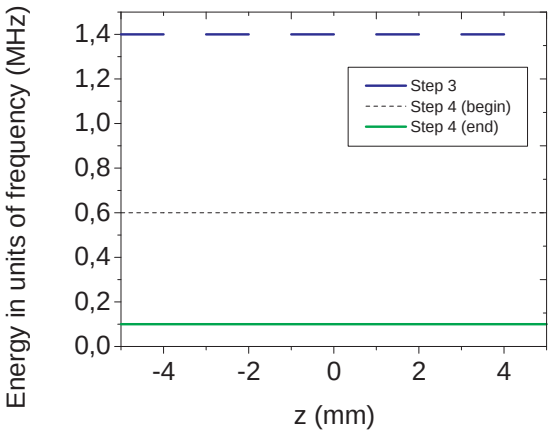

Figure 6.3: Energy v/s z plot in the upper dressed state $m_F = 2$, for various steps of the loading procedure.

4. the dressing rf field is then switched on at 800 kHz below the resonance with the static field B_{0x}, and ramped up to the resonance (up to 1.4 MHz), see Figure 6.3. The atoms are now dressed by the rf field, at the same position. This step has to be done fast enough to avoid a displacement of the atomic cloud due to gravity.

5. the quadrupole field is then ramped together with the dressing rf frequency, in order to keep the atomic position fixed (3 mm below the quadrupole center). For this, we need to maintain the resonance condition $\omega_1(t) = \omega_0(\mathbf{r_0}, t)$ at the same position $\mathbf{r_0}$. This is shown in Figure 6.4 where the energy is plotted for various values of the quadrupole field.

To maintain the resonance condition at all time t during the loading ramp, the following equation must hold:

$$\hbar\omega_1(t) = \hbar\omega_0(\mathbf{r_0}, t) \tag{6.16}$$

where $\omega_0(\mathbf{r_0}, t) = \frac{g_F \mu_B}{\hbar} B(\mathbf{r_0}, t)$ and $B(\mathbf{r_0}, t) = \sqrt{B_{0x}^2 + (b'(t)\Delta z)^2}$. B_{0x} is the magnetic field in the x direction during the optical pumping, $b'(t)\Delta z$ is the field produced by the quadrupolar coils at position $(0, 0, -\Delta z)$, and $b'(t)$ is the quadrupole field gradient in the x and z directions. $b'(t)$ varies proportionally with the quadrupole trap current $I_Q(t)$, we can write $b'(t) = \gamma I_Q(t)$. Now we can rewrite Eq.(6.16) as

$$\omega_1(t) = \frac{g_F \mu_B B_{0x}}{\hbar} \sqrt{1 + \left(\frac{\gamma \Delta z I_Q(t)}{B_{0x}}\right)^2} \tag{6.17}$$

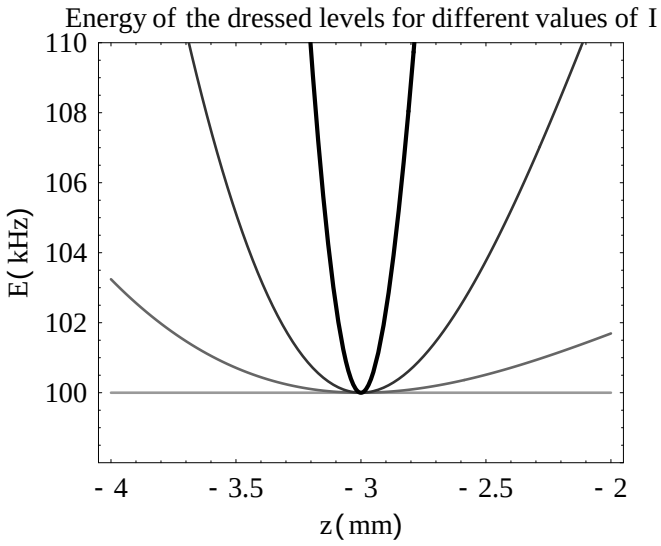

Figure 6.4: Plot of the energy in the extreme $m_F = 2$ dressed state versus z, for increasing values of quadrupolar current: $I_Q = 0$, 0.3, 0.5 and 1 A. The slope becomes steeper and steeper as the current through the quadrupole coils is increased. The atomic position is maintained as $\Delta z = -3$ mm throughout the quadrupolar ramp. The effect of gravity is not represented in this plot.

where $\gamma = 3.44\,\mathrm{G/cm/A}$, $\Delta z = 3\,\mathrm{mm}$ and $B_{0x} = 2\,\mathrm{G}$.

From the above formula we can deduce ω_1 for a given value of I_Q, so that we keep the distance $\Delta z = 3\,\mathrm{mm}$, all the time during the ramping stage. A typical ramp used to load the atoms to the dressed quadrupole trap is shown and commented in Figure 6.5.

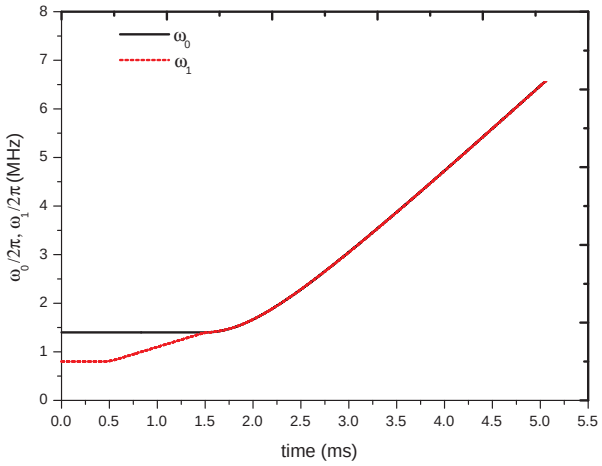

Figure 6.5: Typical shape of a radio frequency ramp applied to the atomic sample. In the present example $\omega_1/2\pi$ (dotted red line) is increased from 0.8 MHz to 7.36 MHz within 5 ms. ω_0 is the total magnetic field in units of frequency at the position of the atoms. The sequence is decomposed into 3 steps: step 1: a 0.5 ms stage where the frequency is maintained at 0.8 MHz for adiabatic switching of the rf source; step 2: the rf frequency is ramped up to 1.4 MHz after the optical pumping stage (1.4 MHz corresponds to the resonance set by the pumping field) in 1.5 ms; step 3: once the resonance is reached both the rf frequency and quadrupole field are ramped together in 3 ms up to 7.36 MHz, which corresponds to a current of 10 A in the quadrupolar coils.

6.3 Experimental results

We applied the procedure described in the last section to successfully load atoms from a molasses into a dressed quadrupole trap. Two absorption pictures of the DQ trap after 5 s of trapping, taken after a short time of flight of 4 ms, with a final frequency of $\omega_1/2\pi = 9.72\,\mathrm{MHz}$ and a rf power of 25 W are shown in Figure 6.6.

We studied the influence of different parameters on the loading efficiency and the lifetime in the DQ trap. The effect of reversing the polarization from σ_z^- to σ_z^+ is shown in Figure 6.6 (right). It is clear from these absorption images that is has a dramatic effect on the loading efficiency. As the lifetime in the case of σ_z^+ polarized rf field is very short, we rather compared the life time in the DQ trap using circularly polarized σ_z^- rf field with life time obtained with a linearly polarized field, at a final frequency

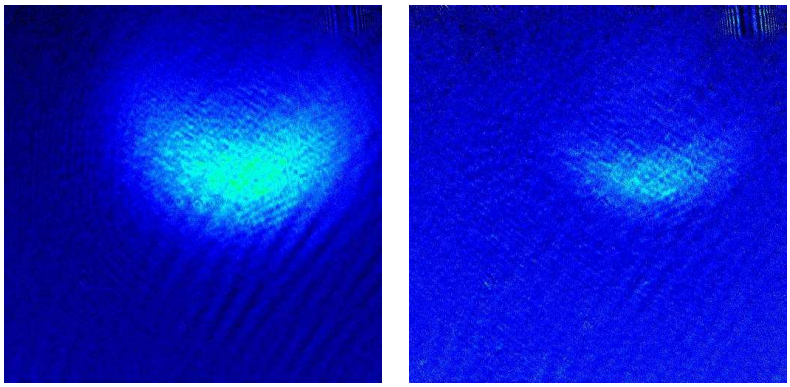

Figure 6.6: Left: absorption image of the DQ trap loaded using a σ_z^- polarized rf field after 5 s holding time, with a final rf frequency of 9.77 MHz and a rf power of 25 W. Right: DQ trap in the same conditions except the polarization of the rf field, which is now σ_z^+ polarized. The polarization is changed by interchanging the 0 and 90 degrees output of the rf phase shifter/power splitter. The time of flight is 4 ms for both pictures.

of 9.72 MHz and a rf power of 10 W. We found an improvement of the life time from 15 s to 19 s after using a σ_z^- circularly polarized rf field with respect to the linearly polarized case.

The life time and the number of atoms in the DQ trap were also compared for various values of the rf power up to a maximum power of 25 W, at the final frequency of 9.72 MHz and using a linearly polarized rf field, see Figures 6.8 and 6.7. We found that the life time increased continuously with the rf power, up to 19 s at 25 W. However, it seems to saturate at the maximum power of 25 W. The number of atoms measured after 5 s in the DQ trap increases linearly with the rf power (Figure 6.7). We don't see any saturation effect in this last case at the maximum power available in the experiment.

These plots indicates that if we put more power by upgrading our 25 W rf amplifier, it would be possible to increase the number of atoms in the DQ trap. We were also limited by the rf power splitter/phase shifter as it cannot work efficiently above 10 MHz (the maximum frequency was 10 MHz according to the specifications of the QE 01-412 Pulsar 1-10 MHz). This is the reason why most of the experiments were done at a final frequency of 9.72 MHz. This prevented us to go to higher values of magnetic gradients for the quadrupole where we could have compressed more and would have a larger density.

We measured the temperature of the atoms in the DQ trap for various values of the holding time by a time of flight experiment. We saw a reduction in the temperature by increasing the holding time. At $t = 0$, the initial temperature is $T = 345\,\mu\text{K}$ whereas at $t = 1\,\text{s}$ it drops down to $T = 285\,\mu\text{K}$ for a linearly polarized rf field of frequency 9.72 MHz, at the maximum power of 25 W. This cooling effect is certainly due to a self evaporation of the hotter atoms from the trap, through the holes at the equator of the trapping ellipsoid. This issue will be addressed by using a circularly polarized field and

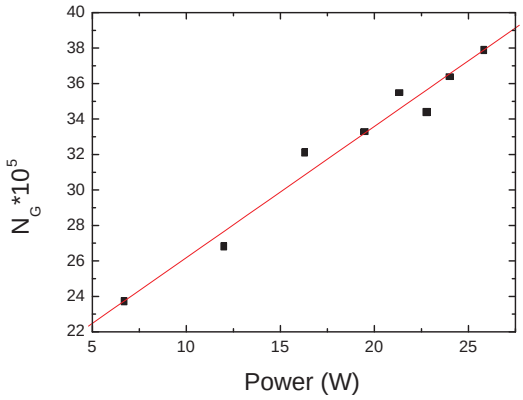

Figure 6.7: Number of atoms remaining in the DQ trap after 5 s of trapping, as a function of the rf power. We see a linear increase in the number of atoms with the rf power. This experiment was done at a final rf frequency of 9.72 MHz and with a linearly polarized rf field.

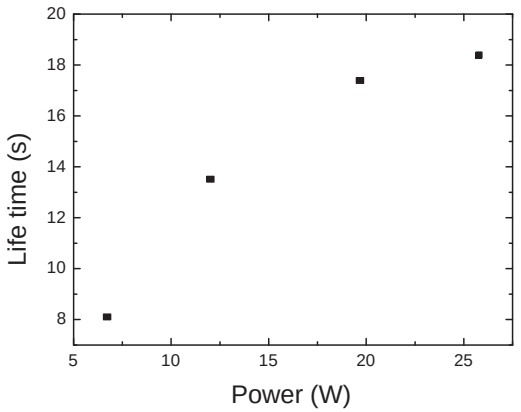

Figure 6.8: Life time in the DQ is plotted as a function of the rf power. We see an increase in the life time and it gets saturated near to 25 W rf power. This experiment was done at rf end frequency of 9.72 MHz and using a linearly polarized rf.

replacing the phase shifter by a device allowing a larger rf frequency, as the radius of the trapping surface could be larger and the evaporation less likely.

6.4 Conclusion

In conclusion, we demonstrated in this chapter a scheme for dressing cold atoms directly in a quadrupole configuration, realizing a dressed quadrupole (DQ) trap. Atoms are prevented to escape through low rf amplitude 'holes' by using a circularly polarized rf field. This helped in improving the life time of atoms in the DQ trap. We also showed a strong dependency in the life time and number of atoms in the DQ trap with the rf power. It may be possible to increase the number of atoms by increasing the rf power further by upgrading our amplifier, which seems to be very promising. In future the next step will be to perform evaporative cooling in the DQ trap down to quantum degeneracy. This system will be very interesting to make a ring trap and to see persistent currents by rotating the ring trap [24].

Chapter 7

Conclusions

The motivation of my Ph.D work was towards confining atomic Bose-Einstein condensate (BEC) into a ring geometry. The ring trap is a simple situation of a multiply connected space rendering the study of a persistent atomic current attractive [48]. The realization of this trap is based on a mechanism where radio frequency and optical dipoles couplings contribute to the creation of a quasi-two dimensional BEC subsequently loaded into a ring trap. This route to a ring BEC has been theoretically studied in the group of V. Lorent and H. Perrin [24].

As a first step towards the ring BEC we have prolonged the experimental investigation of loading a rf dressed trap with a BEC.
On the overall this experience has not reached the quantum degeneracy in a flat rf dressed trap. Several identified reasons have been examined : (i) heating of the atomic cloud due to the technical noise coming from the rf source used to dress the atoms and, (ii) heating coming from the non adiabatic deformation of the trapping potential when the atoms are transferred from the static magnetic trap into rf dressed trap. We did an intense study on the influence of various rf sources which is explained in our paper [36]. We have improved the life time and reduced the heating rate after fulfilling the rf requirements explained in the paper [36]. Still we failed in transferring the BEC directly from a static magnetic trap to rf dressed trap. A heating mechanism comes from the fact that periods of oscillations in the radial directions of the elongated rf dressed trap are unavoidably longer than the typical duration of the trap loading. The adiabaticity condition is never satisfied in this context. To overcome this difficulty it has been decided to dress the atoms first and then to perform evaporative cooling in a similar way it is made in a static magnetic trap. This has been theoretically studied in the group and published in 2006 [23].

In the present thesis, a better understanding of the evaporative cooling in a rf dressed trap has been made by a more extensive study in spectroscopy. It has been found that unlike the situation of evaporative cooling by rf outcoupling inside a static magnetic trap, a probe rf field nearly resonant with the energy spacing between rf dressed states exhibits multiple resonant transitions. Evaporative cooling has been experimented by sweeping in frequency a second rf field close to the observed transitions.

It has been found that evaporative cooling is efficient only with two photon transition. With the present parameters of experiment the phase space density has increased by a factor 8 only and quantum degeneracy is still far from reach. One way to render evaporative cooling in a dressed trap more efficient in quantum degeneracy is to increase the radial frequencies of the trap. This has been tested with a static quadrupole trap which yields larger trap frequencies. The magnetic field of a quadrupole is oriented mainly longitudinally in all directions. The polarization of the rf field becomes an important parameter since the rf coupling will asymptotically vanish in some directions of space. It has been found that a circular polarized σ_z^- rf oriented in the vertical radial direction of the quadrupole is a suitable choice. The loading of a rf dressed quadrupole trap is also an issue. We have tested two mechanisms. The transfer of atoms from a dressed Ioffe-Pritchard (QUIC) trap to a dressed quadrupole trap has the drawback of a fifty percent loss of atoms due to a transient in a zero magnetic field. A scheme to load directly the atomic cloud from a magneto optical trap to the rf dressed has been tested and has been proved to be more efficient.

The immediate future of this experiment is to perform evaporative cooling in the dressed quadrupole trap and possibly to reach quantum degeneracy. The radial strength of the dressed trap will be reinforced by the help of a dipole potential obtained produced by a red detuned laser piercing the centre of the magnetic quadrupole trap.

On the other hand the idea of combining a blue detuned optical standing wave in the vertical direction to the rf dressed trap as proposed in [24] can be applied here to load the atoms into a circular geometry. Thus the quadrupole geometry with a symmetry axis oriented in the vertical direction is ideal for the realization of a isotropic quasi-2D degenerate gas [49] or an atomic ring [24].

Once the atomic ring is created it could be stirred by an application of a periodic perturbation [24, 44, 45]. This will initiate persistent currents in the atomic ring which has been explored in some theoretical papers [50–53] and experimentally by [45]. In a superconductor, persistent flow is electrical current without resistance: current in a loop of superconducting wire will flow essentially forever. In a superfluid [54] such as liquid helium below the lambda point, the frictionless flow allows persistent circulation in a hollow toroid. Persistent flow of a BEC could be used to understand the fundamental relationship between superfluidity and Bose-Einstein condensation, especially in one- and two-dimensional systems. For example, a strongly interacting 1D gas is predicted to show superfluidity [55], although such a system does not Bose condense. Superfluid flow of quantum gas in a ring geometry raises new interesting possibilities. For example, with the addition of a quantum tunnel barrier, acting as a Josephson junction, the analog of a superconducting quantum interference device (SQUID) could be realized for a gas of atoms [56]. The UC Berkeley team has created a Bose-Einstein condensate of rubidium atoms and nudged it into a circular racetrack 2 millimeters across, creating a particle storage ring analogous to the accelerator storage rings of high energy physics [57]. Apart from basic physics, however, the millimeter storage rings could be used as sensitive gyroscopes to detect minute changes in rotation. If a ring could be created with two BECs traveling in opposite directions, the quantum interference pattern the two matter waves create would shift with rotation, allowing

exquisitely sensitive detection of rotation for use in research or navigation systems for satellites or aircraft. In the group of V.Lorent and Hélène Perrin future plan of study include quantized circulation, which is seen in superfluids and superconductors.

Bibliography

[1] S.N. Bose. Plancks Gesetz und Lichtquantenhypothese. *Z. Phys.*, 26:178–181, 1924.

[2] A. Einstein. Quantentheorie des einatomigen idealen Gases. *Sitzungsber. Kgl. Preuss. Akad. Wiss.*, :261–267, 1924.

[3] A. Einstein. Quantentheorie des einatomigen idealen Gases. Zweite Abhandlung. *Sitzungsber. Kgl. Preuss. Akad. Wiss.*, :3–14, 1925.

[4] L. Landau. Theory of the superfluidity of helium ii. *Phys. Rev.*, 60(4):356–358, Aug 1941.

[5] J. Zimányi, G. Fái, and B. Jakobsson. Bose-Einstein condensation of pions in energetic heavy-ion collisions? *Phys. Rev. Lett.*, 43(23):1705–1707, Dec 1979.

[6] M.H. Anderson, J.R. Ensher, M.R. Matthews, C.E. Wieman, and E.A. Cornell. Observation of Bose-Einstein condensation in a dilute atomic vapor. *Science*, 269:198–201, 1995.

[7] K.B. Davis, M.-O. Mewes, M.R. Andrews, N.J. van Druten, D.S. Durfee, D.M. Kurn, and W. Ketterle. Bose-Einstein condensation in a gas of sodium atoms. *Phys. Rev. Lett.*, 75(22):3969–3973, 1995.

[8] C.C. Bradley, C.A. Sackett, J.J. Tollett, and R.G. Hulet. Evidence of Bose-Einstein condensation in an atomic gas with attractive interactions. *Phys. Rev. Lett.*, 75(9):1687–1690, 1995. Erratum : *ibid.* **79** (6), 1170 (1997).

[9] L. Pricoupenko, H. Perrin, and M. Olshanii, editors. *Proceedings of the Euroschool on quantum gases in low dimensions, Les Houches 2003*, volume 116. J. Phys. IV, 2004.

[10] W. Hänsel, P. Hommelhoff, T.W. Hänsch, and J. Reichel. Bose-Einstein condensation on a microelectronic chip. *Nature*, 413:498–501, 2001.

[11] R. Folman, P. Krüger, J. Schmiedmayer, J. Denschlag, and C. Henkel. Microscopic atom optics: from wires to an atom chip. *Adv. At. Mol. Opt. Phys.*, 48:263, 2002.

[12] L. Tonks. The complete equation of state of one, two and three-dimensional gases of hard elastic spheres. *Phys. Rev.*, 50(10):955–963, 1936.

[13] M. Girardeau. Relationship between systems of impenetrable bosons and fermions in one dimension. *J. Math. Phys.*, 1:516–523, 1960.

[14] M. Olshanii. Atomic scattering in the presence of an external confinement and a gas of impenetrable bosons. *Phys. Rev. Lett.*, 81(5):938–941, 1998.

[15] V. Berezinskii. Destruction of long-range order in one-dimensional and 2-dimensional systems having a continuous symmetry group, 1 - classical systems. *Sov. Phys. JETP-USSR*, 32:493, 1971.

[16] V. Berezinskii. Destruction of long-range order in one-dimensional and 2-dimensional systems having a continuous symmetry group, 2 - quantum systems. *Sov. Phys. JETP-USSR*, 34:610, 1972.

[17] J.M. Kosterlitz and D.J. Thouless. Ordering, metastability and phase transitions in two-dimensional systems. *J. Phys. C : Solid State Phys.*, 6:1181–1203, 1973.

[18] Z. Hadzibabic, P. Krüger, M. Cheneau, B. Battelier, and J. Dalibard. Berezinskii-kosterlitz-thouless crossover in a trapped atomic gas. *Nature*, 441:1118, 2006.

[19] A Gorlitz, J.M. Vogels, C Leanhardt, A.E.and Raman, T.L. Gustavson, J.R. Abo-Shaeer, A.P. A.Chikkatur, S Gupta, S Inouye, T Rosenband, and W Ketterle. Realization of bose-einstein condensates in lower dimensions. *Phys. Rev. Lett.*, 87:130402, 2001.

[20] S. Stock, Z. Hadzibabic, B. Battelier, M. Cheneau, and J. Dalibard. Observation of phase defects in quasi-two-dimensional bose-einstein condensates. *Phys. Rev. Lett.*, 95:190403, 2005.

[21] O. Zobay and B.M. Garraway. Two-dimensional atom trapping in field-induced adiabatic potentials. *Phys. Rev. Lett.*, 86(7):1195–1198, 2001.

[22] Y. Colombe, E. Knyazchyan, O. Morizot, B. Mercier, V. Lorent, and H. Perrin. Ultracold atoms confined in rf-induced two-dimensional trapping potentials. *Europhys. Lett.*, 67(4):593–599, 2004.

[23] C.L. Garrido Alzar, H. Perrin, B.M. Garraway, and V. Lorent. Evaporative cooling in a radio-frequency trap. *Phys. Rev. A*, 74:053413, 2006.

[24] O. Morizot, Y. Colombe, V. Lorent, H. Perrin, and B.M. Garraway. Ring trap for ultracold atoms. *Phys. Rev. A*, 74:023617, 2006.

[25] Tomoya Isoshima, Mikio Nakahara, Tetsuo Ohmi, and Kazushige Machida. Creation of a persistent current and vortex in a bose-einstein condensate of alkali-metal atoms. *Phys. Rev. A*, 61(6):063610, May 2000.

[26] L. Landau. Theory of the superfluidity of helium ii. *Phys. Rev.*, 60(4):356–358, Aug 1941.

[27] Y. Colombe. *Condensat de Bose-Einstein, champs évanescents et piégeage bidimensionnel*. PhD thesis, Université Paris XIII, 2004.

[28] O. Morizot. *Pièges radiofréquence très anisotropes pour un condensat de Bose-Einstein*. PhD thesis, Université Paris XIII, 2007.

[29] E.L. Raab, M. Prentiss, A. Cable, S. Chu, and D.E. Pritchard. Trapping of neutral sodium atoms with radiation pressure. *Phys. Rev. Lett.*, 59(23):2631–2634, 1987.

[30] T. Esslinger, I. Bloch, and T.W. Hänsch. Bose-Einstein condensation in a quadrupole-Ioffe-configuration trap. *Phys. Rev. A*, 58(4):R2664–R2667, 1998.

[31] H. F. Hess. Evaporative cooling of magnetically trapped and compressed spin-polarized hydrogen. *Phys. Rev. B*, 34:3476, 1986.

[32] N. Masuhara, J. M. Doyle, J. C. Sandberg, D. Kleppner, T. J. Greytak, H. F. Hess, and G. P. Kochanski. Evaporative cooling of spin-polarized atomic hydrogen. *Phys. Rev. Lett.*, 61:935, 1988.

[33] E. Dimova, O. Morizot, G. Stern, C.L. Garrido Alzar, A. Fioretti, V. Lorent, D. Comparat, and H. Perrin. Continuous transfer and laser guiding between two cold atom traps. *Eur. Phys. J. D*, 42:299, 2007.

[34] W. Ketterle and N.J. van Druten. Evaporative cooling of trapped atoms. In B. Bederson and H. Walther, editors, *Advances in atomic, molecular and optical physics*, volume 37, pages 181–236. Academic Press, 1996.

[35] B. Hofferberth, T. Fischer, J. Schumm, I. Schmiedmayer, and Lesanovsky. Ultracold atoms in radio-frequency dressed potentials beyond the rotating-wave approximation. *Phys. Rev. A*, 76:013401, 2007.

[36] O. Morizot, L. Longchambon, R. Kollengode Easwaran, R. Dubessy, E. Knyazchyan, P.-E. Pottie, V. Lorent, and H. Perrin. Influence of the Radio-Frequency source properties on RF-based atom traps. *Eur. Phys. J. D*, 47:209, 2008.

[37] M.E. Gehm, K.M. O'Hara, T.A. Savard, and J.E. Thomas. Dynamics of noise-induced heating in atom traps. *Phys. Rev. A*, 58(5):3914–3921, 1998. Erratum: Phys. Rev. A **61**, 029902 (2000).

[38] W. Ketterle, D.S Durfee, and D.M Stamper-Kurn. Making, probing and understanding Bose-Einstein condensates. In M. Inguscio, S. Stringari, and C.E. Wieman, editors, *Proceedings of the International School of Physics "Enrico Fermi", Course CXL*, pages 67–176. IOS Press Ohmsha, 1999.

[39] M. White, H. Gao, M. Pasienski, and B. DeMarco. Bose-Einstein condensates in rf-dressed adiabatic potentials. *Phys. Rev. A*, 74(2):023616, 2006.

[40] O. Zobay and B.M. Garraway. Atom trapping and two-dimensional Bose-Einstein condensates in field-induced adiabatic potentials. *Phys. Rev. A*, 69:023605, 1–15, 2004.

[41] S. Hofferberth, I. Lesanovsky, B. Fischer, J. Verdu, and J. Schmiedmayer. Radiofrequency-dressed-state potentials for neutral atoms. *Nature Phys.*, 2:710, 2006.

[42] C. Cohen-Tannoudji. Atomes ultra-froids – Piégeage non dissipatif et refroidissement évaporatif. Cours de physique atomique et moléculaire, Collège de France, année 1996-1997.

[43] O. Morizot, C.L. Garrido Alzar, P.-E. Pottie, V. Lorent, and H. Perrin. Trapping and cooling of rf-dressed atoms in a quadrupole magnetic field. *J. Phys. B: At. Mol. Opt. Phys.*, 40:4013–4022, 2007.

[44] K. W. Madison, F. Chevy, W. Wohlleben, and J. Dalibard. Vortex formation in a stirred bose-einstein condensate. *Phys. Rev. Lett.*, 84:806, 2000.

[45] C. Ryu, M. F. Andersen, P. Cladé, V. Natarajan, K. Helmerson, and W. D. Phillips. Observation of persistent flow of a bose-einstein condensate in a toroidal trap. *Phys. Rev. Lett.*, 99:260401, 2007.

[46] W. M. Van Alphen, R. de Bruyn Ouboter, K. W. Taconis, and E. van Spronsen. Persistent flow and potential motion of superfluid helium. *Physica*, 39:109, 1968.

[47] W. Petrich, M.H. Anderson, J.R. Ensher, and E.A. Cornell. Stable, tightly confining magnetic trap for evaporative cooling of neutral atoms. *Phys. Rev. Lett.*, 74:3352, 1995.

[48] W. H. Heathcote, E. Nugent, B. T. Sheard, and C. J. Foot. A ring trap for ultracold atoms in an rf-dressed state. *New Journal of Physics*, 10(4):043012, 2008.

[49] L.P. Pitaevskii and A. Rosch. Breathing modes and hidden symmetry of trapped atoms in two dimensions. *Phys. Rev. A*, 55(2):R853–R856, 1997.

[50] Juha Javanainen, Sun Mok Paik, and Sung Mi Yoo. Persistent currents in a toroidal trap. *Phys. Rev. A*, 58(1):580–583, Jul 1998.

[51] L. Salasnich, A. Parola, and L. Reatto. Bosons in a toroidal trap: Ground state and vortices. *Phys. Rev. A*, 59(4):2990–2995, Apr 1999.

[52] Juha Javanainen and Yi Zheng. Perturbing a persistent current with an external potential. *Phys. Rev. A*, 63(6):063610, May 2001.

[53] Eileen Nugent, Dermot McPeake, and J. F. McCann. Superfluid toroidal currents in atomic condensates. *Phys. Rev. A*, 68(6):063606, Dec 2003.

[54] A. J. Leggett. Superfluidity. *Rev. Mod. Phys.*, 71:S318, 1999.

[55] Yu. Kagan, N. V. Prokof'ev, and B. V. Svistunov. Supercurrent stability in a quasi-one-dimensional weakly interacting bose gas. *Phys. Rev. A*, 61(4):045601, Mar 2000.

[56] B. P. Anderson, K. Dholakia, and E. M. Wright. Atomic-phase interference devices based on ring-shaped bose-einstein condensates: Two-ring case. *Phys. Rev. A*, 67:033601, 2003.

[57] S. Gupta, K. W. Murch, K. L. Moore, T. P. Purdy, and D. M. Stamper-Kurn. Bose-einstein condensation in a circular waveguide. *Phys. Rev. Lett.*, 95:143201, 2005.

Résumé

Le refroidissement évaporatif d'un nuage d'atomes de rubidium ultra froids a été étudié dans le cadre d'un piégeage radio-fréquence dans un champ magnétique inhomogène de type Ioffe-Pritchard. Contrairement à la situation rencontrée dans les pièges magnétiques statiques où une transition radio-fréquence à un photon est utilisée pour contrôler la hauteur du piège, nous montrons qu'une transition à plusieurs photons est nécessaire pour contrôler la hauteur d'un piège habillé par un champ radio-fréquence. L'efficacité de l'évaporation n'est pas identique pour toutes les transitions : une transition à deux photons s'est avérée la plus efficace par rapport aux autres. Des résultats préliminaires de refroidissement évaporatif sont discutés. La dégénérescence quantique, qui est le but poursuivi dans le refroidissement évaporatif, n'a pas été atteinte : la très grande anisotropie du piège rendant pratiquement impossible la thermalisation à l'intérieur du piège. La dégénérescence quantique dans un piège radio-fréquence très anisotrope pourrait être satisfaite par la transformation adiabatique vers ce piège à partir d'un condensat de Bose-Einstein produit dans un piège magnétique de type Ioffe-Pritchard. Les expériences qui ont été réalisées dans ce sens ont été négatives : les fréquences latérales du pièges radio-fréquences sont trop basses pour assurer une transformation adiabatique en un temps raisonnable pour l'expérience. La fin de la thèse expose des résultats préliminaires de piégeage d'atomes dans une configuration magnétique quadrupolaire, cette dernière configuration conduisant à des fréquences d'oscillation de piège plus élevées dans les directions latérales.

Mots clés : condensat de Bose-Einstein – gaz 2D – rubidium – atomes habillés – champ radiofréquence – potentiels adiabatiques – spectroscopie – refroidissement par évaporation

Abstract

In this thesis, I describe the spectroscopic investigations and preliminary results of evaporative cooling of rubidium atoms done on a magnetic trap dressed with a radiofrequency field. Unlike the case of a static magnetic trap, where a single radiofrequency photon is used to outcouple atoms we have demonstrated that a multiphoton transition is necessary. This transitions are nearly resonant with the energy spacing of the radiofrequency dressed states. The evaporation efficiency is not the same for all the observed transitions: the transition involving a two photon process is more efficient compared to the others. Preliminary results of evaporative cooling in a radiofrequency dressed trap are discussed. The quantum degeneracy is not reached as it is difficult to reach thermalization due to the strong anisotropy in the trap. A way to render the evaporative cooling more efficient is to increase the horizontal oscillation frequencies. Finally, we discuss a method to load the atoms into a radiofrequency dressed quadrupole trap, leading to large oscillation frequencies in the horizontal directions.

Key words : Bose-Einstein condensation – 2D gas – rubidium – dressed atoms – radiofrequency field – adiabatic potentials – spectroscopy – evaporative cooling